Etude de la rhéologie des composites polymères au cours du procédé FDM (Fabrication additive)

Mohammad Ahmadifar

To cite this version:

Mohammad Ahmadifar. Etude de la rhéologie des composites polymères au cours du procédé FDM (Fabrication additive). Mécanique [physics.med-ph]. HESAM Université, 2021. Français. NNT : 2021HESAE072 . tel-03708381

HAL Id: tel-03708381
https://pastel.hal.science/tel-03708381v1

Submitted on 29 Jun 2022

HESAM UNIVERSITÉ

Arts et Métiers Sciences et Technologies

ÉCOLE DOCTORALE SCIENCES DES MÉTIERS DE L'INGÉNIEUR
[PIMM- Procédés et Ingénierie en Mécanique et Matériaux]
[LCPI-Laboratoire Conception de Produits et Innovation]
[Campus de Paris]

THÈSE

présentée par : **Mohammad AHMADIFAR**
soutenance le : **13/12/2021**

pour obtenir le grade de : **Docteur d'HESAM Université**
préparée à : **École Nationale Supérieure d'Arts et Métiers**
Spécialité : **Mécanique des matériaux**

Etude de la rhéologie des composites polymères au cours du procédé FDM (Fabrication additive)

THÈSE dirigée par :
[Abbas TCHARKHTCHI]
et Co-encadrée par :
[Khaled BENFARIHA & Mohammadali SHIRINBAYAN]

Jury

M. Fodil MERAGHNI, Professeur, LEM3, Arts et Métiers ParisTech	Président
Mme. Françoise BERZIN, Professeure, Université de Reims Champagne Ardenne	Rapportrice
M. Hakim BOUZID, Professeur, ETS Montréal -Canada	Rapporteur
M. Alireza KHAVANDI, Professeur, IUST-Iran	Examinateur
Mme. Zaida ORTEGA, Docteur, ULPGC-Espagne	Examinatrice
M. Khaled BENFRIHA, Docteur (HDR), LCPI, Arts et Métiers ParisTech	Examinateur
M. Mohammadali SHIRINBAYAN, Docteur, PIMM, Arts et Métiers ParisTech	Examinateur
M. Abbas TCHARKHTCHI, Professeur, PIMM, Arts et Métiers ParisTech	Examinateur
Mme. Marie-France LACRAMPE, Professeur, École des Mines de Douai	Invitée

THÈSE

Contents

List of Figures

List of Tables

1 Introduction general

Additive Manufacturing (AM) is the manufacturing method for fabricating objects from the 3D CAD model, and it is a layer-by-layer manufacturing process. While the subtractive manufacturing process is introduced as another category of the 3D printing methods, which is based on successively removing material away from a solid block of material to obtain the desired three-dimensional object. Additive manufacturing also known as freeform fabrication, layer manufacturing, additive processes, additive techniques, and solid freeform fabrication. AM method begins with CAD software and designing to prepare the desired model. Then it will be sliced into a predefined number of layers and fabricated sequentially. Moreover, AM is utilized widely because of its capability to manufacture objects with complex shapes which are hard to be fabricated by means of conventional methods. Compared to conventional methods, AM process reduces post processing and material wastes. Also, it has appealed the attentions because of its economical features for rapid prototyping and production applications.

AM techniques after several decades such as stereolithography (SLA), Fused Filament Fabrication (FFF) or Fused Deposition Modeling (FDM), Selective Laser Sintering (SLS), Selective Laser Melting (SLM), Multi-Jet Modeling (MJM), Laminated Object Manufacturing (LOM) and Stereo-Lithography (SL), have been developed. Among the stated methods, the Fused Filament Fabrication (FFF) process due to less material wastage, less expensive used materials and tools is more cost-effective than the other processes. Therefore, FFF is currently the most widely available AM platform. The most widely used AM methods for processing polymer composites are FFF and Selective Laser Sintering (SLS), while the FFF method has been considered as the more beneficial process. Some advantages of FFF process in comparison with other AM methods are ability to deposit several materials simultaneously, low input energy, material availability, minimum waste of material because they are less prone to degradation, less expensive machines and materials, no need for subsequent chemical processing and machining, availability wide range of printers at different prices. While as the main drawback, the mechanical properties of the manufactured parts by the FFF methods are weaker than manufactured parts by the conventional methods. The stated weak mechanical properties are due to weak adhesion between the deposited layers. So, as for improving this the weak adhesion between the deposited layers in FFF process, it is important to identified the material parameters, machine parameters, and the process parameters.

From the start of utilizing the FFF/FDM process as fabrication process, numerous studies have been conducted for developing this process. Also, better description of the rheological characteristics such as material flow and mechanical strength allowed researchers to have a better viewpoint from the challenges. There are many challenges in aspect of the consideration of the process optimization by considering the rheological characteristics of materials. This approach along with in-process monitoring of various parameters effects, is an effective and helpful method to reach the final goal which is the production of optimum-quality final parts. Beside of the above-mentioned explanation, the below prerequisites for process optimization purposes are required:

- Temperature profile of filaments is an important subject and affect the bonding
- Temperature dependence viscosity must be considered
- Interaction of parameters and their impact on temperature evolution of filaments must be considered.

In this study, according to the literature review, some parameters that affect the printed part quality were selected. The chosen process parameters are the liquefier temperature, layer height, print speed, and bed platform temperature. This study differs from previous studies in the following ways:

- The interaction of essential process parameters such as liquefier temperature, platform temperature, layer height and print speed (identified from the literature) on the mechanical properties have been considered.
- The temperature evolution of filaments during FDM/FFF process by in-process monitoring of temperature measurements at the interface of adjacent filaments has been considered.
- Moreover, using the recorded temperature value, this study investigates the non-isotherm viscosity evolution of filaments.

The main objective of this research is to study the rheological characteristics of materials during FDM/FFF in order to process optimization to mechanical characterization improvement of the fabricated parts. In fact, As explained, the essential problem with parts produced with the FDM/FFF process is the adhesion between the filaments and the presence of porosity inside the part. This poor adhesion is linked to the fact that during the deposition of the molten filament (filament n), the preceding filament, n-1, is already cooled and solidified. Under this condition, it is clear that good adhesion between a solid material and a very viscous molten material cannot be expected. So, what is the solution? The answer is simple. Filament n-1 must always be kept in the molten state, hence the welding between the two filaments takes place correctly. However, for the dimensional stability problem, the filament n-1 must be melted only locally and at the time of contact with the filament n. This explains why, a precise and local measurement of the temperature on the scale of the diameter of the filaments is necessary.

Therefore, the solution should take into consideration both the temperature and the viscosity parameters. And establish the Time-Temperature-Transformation diagram for process optimization. This helps us to determine the processability area.

After presenting of literature review in section 1, in section 2, the result of the conducted studies so far toward the investigating the influence of FDM/FFF parameters on mechanical performance and part quality of manufactured parts have been provided. The literature review results related to printed composite materials are sorted in two main sections of powder reinforced polymers and Fused Filament Fabrication of fiber-reinforced polymers as sections 2.3.1 and 2.3.2. The used materials and the applied characterization methods have been introduced in section 3.

The primary characterization results are presented in section 4.1. The influence of four main process parameters which are liquefier temperature, bed platform temperature, layer height, and print speed on the part quality of the composite parts during FDM/FFF process have been presented in section 4.2. In this section it was tried to have a look on the process parameter effects on the polymer which was the used matrix component in the studied composite. The viscosity measurement and temperature effect on viscoelastic properties have been studied in section 4.3 to establish Time-Temperature-Transformation diagram.

Moreover, the published papers of the present thesis are listed as follows which are cited in the text with the label of “Article No.--".

Article No. 1: M. Ahmadifar, K. Benfriha, M. Shirinbayan, A. Tcharkhtchi; Additive Manufacturing of Polymer-Based Composites Using Fused Filament Fabrication (FFF): A Review; Applied Composite Materials Journal, August 2021.

DOI: 10.1007/s10443-021-09933-8

Article No. 2: K. Benfriha, M. Ahmadifar, M. Shirinbayan, A. Tcharkhtchi; Effect of process parameters on thermal and mechanical properties of polymer-based composites using fused filament fabrication; Polymer Composites, August 2021.

DOI: 10.1002/pc.26282

Article No. 3: M. Ahmadifar, K. Benfriha, M. Shirinbayan, A. Tcharkhtchi; Mechanical Behavior of Polymer-Based Composites Using Fused Filament Fabrication (FFF) under Monotonic and Fatigue Loadings; Polymers & Polymer Composites, Accepted paper.

Article No. 4: Z. Shakeri, K. Benfriha, M. Shirinbayan, M. Ahmadifar, A. Tcharkhtchi; Mathematical modeling and Optimization of FFF process parameters for shape deviation control using Taguchi method; Polymers, Accepted paper.

Article No. 5: M. Ahmadifar, K. Benfriha, M. Shirinbayan, A. Tcharkhtchi; Process parameters effect on thermal and mechanical properties of PA6 using fused filament fabrication; Applied Polymer Science Journal, Under review.

2 State of the art

2.1 Fused Filament Fabrication (FFF) influencing parameters

The manufacturing of the parts depends on many parameters related to the following elements: material, shape and geometry, process, and tools (mold, machine, and …). Numerous studies focused on finding a relationship between the properties and processing parameters of FFF process in printed parts, such as layer thickness or raster angle [1, 2, and 3]. In FFF process, each parameter has its own influence on the microstructure and bonding/strength of the fabricated parts. Some process parameters have been introduced in Fig 1.

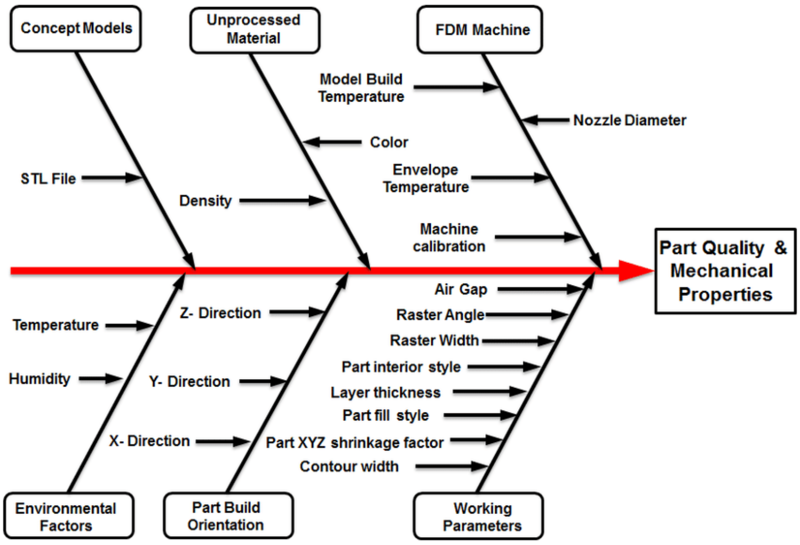

Fig. 1. Representation of influencing parameters in FFF process [4]

Due to the nature of FFF, almost all the 3D-printing machines comprise numerous process parameters. This allows users to utilize a wide range of parameters. Following Fig. 1, the process parameters such as road width, print speed, layer thickness, feed rate and build temperature of the model (both liquefier and envelope temperature), fiber orientation, layer position, volume fraction, and infill orientation should be considered when evaluating the strength/bonding and physicochemical characterization of FFF-fabricated parts. Almost all of them affect the filament bonding and consequently the mechanical behavior of 3D-printed parts. However, researchers tried to focus on some key parameters due to the numerous values that exist for the FFF process by optimizing the experimental procedure to obtain the best combination of parameters that help to improve the bonding of adjacent filaments, as much as possible. The development of the mechanical behavior and dimension accuracy of the printed parts are considered as the two most important criteria in optimized additive manufacturing process.

Various research studies consider the influence of parameters on parts fabricated using FFF. Build orientation and raster angle and their effects on the mechanical properties of 3D-printed parts have been consequently studied and the effect of raster angle was analyzed using infill patterns (Fig. 2) [1, 3].

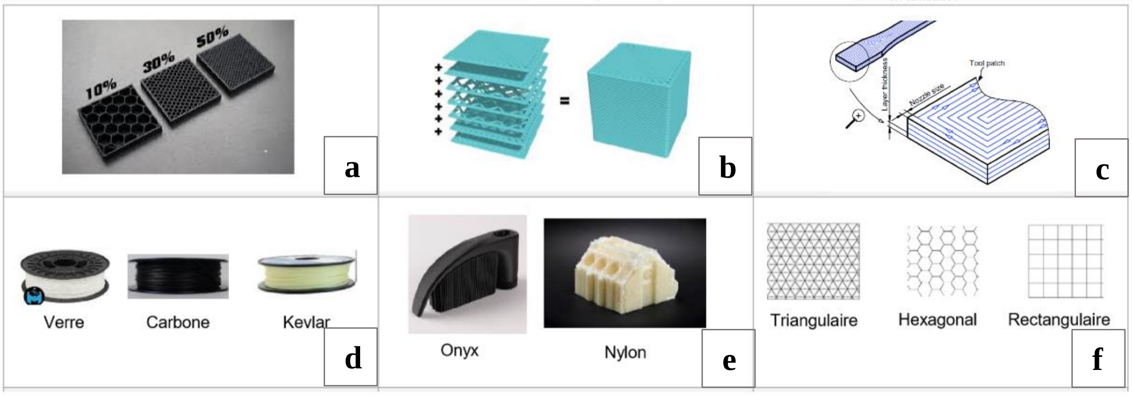

Fig. 2. FFF parameters in composites, (a) Effect of infill density, (b) Effect of the quantity of the layers, (c) Effects of tool path, nozzle size, and layer thickness, (d) Effect of the type of the used reinforcement material, (e) Effect of the type of the used matrix, (f) Effect of infill pattern

Regarding the type of applied material and the studied parameters, it was understood that almost all researchers tried to evaluate the effect of process parameters by means of the different characterization methods (e.g. tensile or bending).

2.2 Fused Filament Fabrication (FFF) process in polymers

The effect of in-process and post-process thermal treatment and the environment temperature or envelope temperature on the fabricated parts have been studied. Based on Fig. 3, diffusion, and neck-growth between of two adjacent filaments would be affected by the environment or envelope temperature change indicating the importance of the heat transfer during this process.

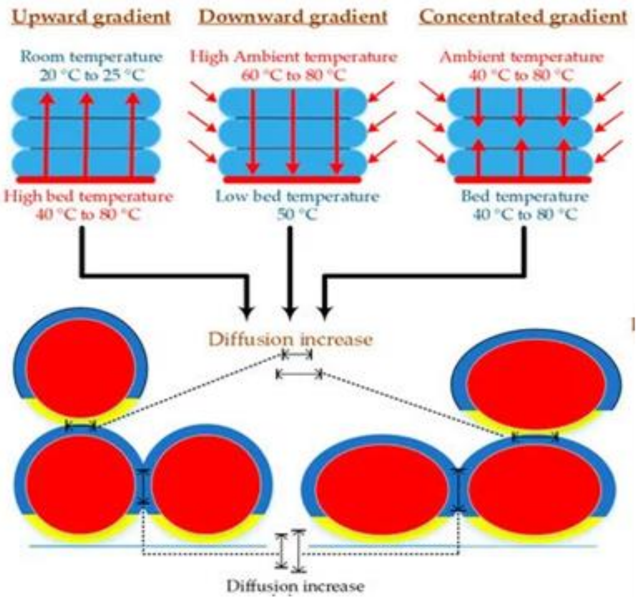

Fig. 3. In-process thermal treatment at the different type of heat gradient on printed structure [5]

Table 1 presents an overview of FFF process parameters for polymers without any reinforcements. One can note that these studies can be useful to understand FFF process in composite especially the effect of reinforcements to improve mechanical properties of structures. In fact, in this table different research works have been reviewed to show their importance. In these studies, some processing parameters such as raster, air gap, raster width, layer thickness, temperature, building orientation, and etc have been analyzed. The results of all studied to confirm the importance of temperature and building orientation effects on the mechanical properties of the printed sample. However, as mentioned this information could help us to better study the bonding filaments and consequently the mechanical properties of composite parts made by the FFF process.

Study	Materials	Parameters
Fodran, 1996 [6]	ABS	Fill gap, line width, slice thickness
Bertoldi, 1998 [7]	ABS	Building orientation, raster orientation
Es-said, 2000 [8]	ABS	Layer orientations
Rodriguez, 2001 [9]	ABS	Fiber gap, flow rate
Ahn, 2002 [10]	ABS	Raster orientation, bead width, color, temperature
Lee, 2005 [11]	ABS	Raster, air gap, raster width, layer thickness

Sun, 2008 [12]	ABS	Temperature variations with part building location
Sood, 2010 [13]	ABS	Layer thickness, orientation, raster angle, and air gap
Fatimatuzahraa, 2011 [1]	ABS	Raster (axial, crisscross, cross, and transverse)
Sood, 2012 [14]	ABS	Layer thickness, orientation, raster angle, air gap
Croccolo, 2013 [2]	ABS	Raster pattern, building orientation
Durgun, 2014 [15]	ABS	Raster angles, building orientation
Gorsky, 2014 [16]	ABS	Building orientation
Baich, 2015 [17]	ABS	Infill (low, high, double dense, solid)
Gorski, 2015 [18]	ABS	Orientation
Ziemian, 2015 [19]	ABS	Raster orientations
Onwubolu, 2016 [20]	ABS	Layer thickness, orientation, raster angle, and air gap
Tymark, 2014 [21]	ABS, PLA	Layer thickness, raster orientation
Ebel, 2014 [22]	ABS, PLA	Infill pattern, infill percentage
Rankouhi, 2016 [23]	ABS	Layer thickness, raster orientations
Letcher, 2015 [24]	ABS	Number of layers, raster orientation
Fernandez, 2016 [25]	ABS	Infill, fill pattern
Alvarez, 2016 [26]	ABS	Infill
Hernandez, 2016 [27]	ABS	Building orientations
Torrado, 2016 [28]	ABS	Raster patterns
Ransey, 2017 [29]	ABS	Building orientations, infill
Tanikella, 2017 [5]	Nylon, ABS, PC	Different materials, color, building orientation
Cantrell, 2017 [30]	ABS, PC	Raster, building orientations

Table 1. FFF process in polymers

Some researchers such as Michael Montero et al [31], have been done by comparing the mechanical behaviors of ABS printed samples with injection molded samples, which were made of ABS. In this research, influence of the five variables, which were air gap, road width (bead width), model temperature, color and orientation of raster were studied on the printed specimens. The variables and their levels were according to table 2. The used raw material was ABS P400.

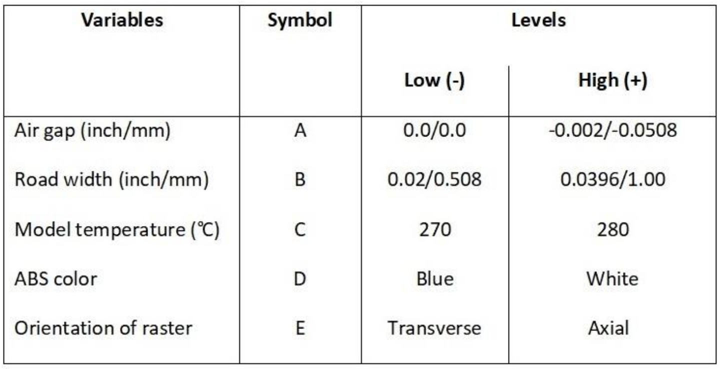

Variables	Symbol	Levels	
		Low (-)	High (+)
Air gap (inch/mm)	A	0.0/0.0	-0.002/-0.0508
Road width (inch/mm)	B	0.02/0.508	0.0396/1.00
Model temperature (℃)	C	270	280
ABS color	D	Blue	White
Orientation of raster	E	Transverse	Axial

Table 2. Variables and level settings [31]

It was proved that raster orientation and air gap had a significant impact on the tensile strength, according to the Fig. 4.

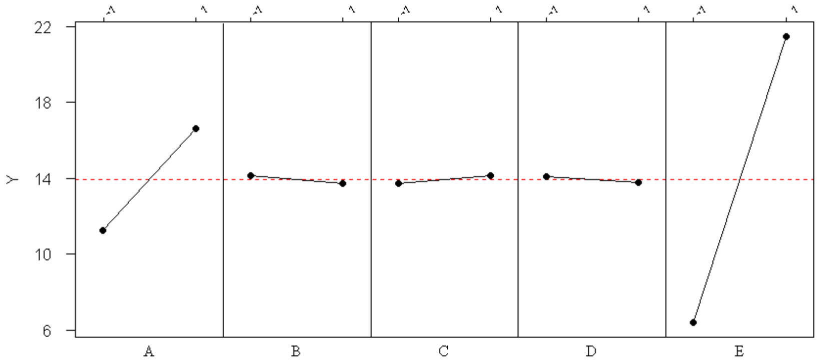

Fig. 4. Plot of tensile strength (MPa) versus the main effects [31]

To study the effect of raster angle and air gap on mechanical behavior of ABS printed parts, some specimens were prepared in five conditions, which were injection molded ABS P400, [0°] (axial), [45°/-45°] (crisscross), [0°/90°] (cross) and [90°] (Transvers) under two levels of zero and negative as deals of air gap. The results of tensile test with various raster compared with injection molded ABS P400, under condition of zero and -0.003 inch air gap, were according to Fig. 5.

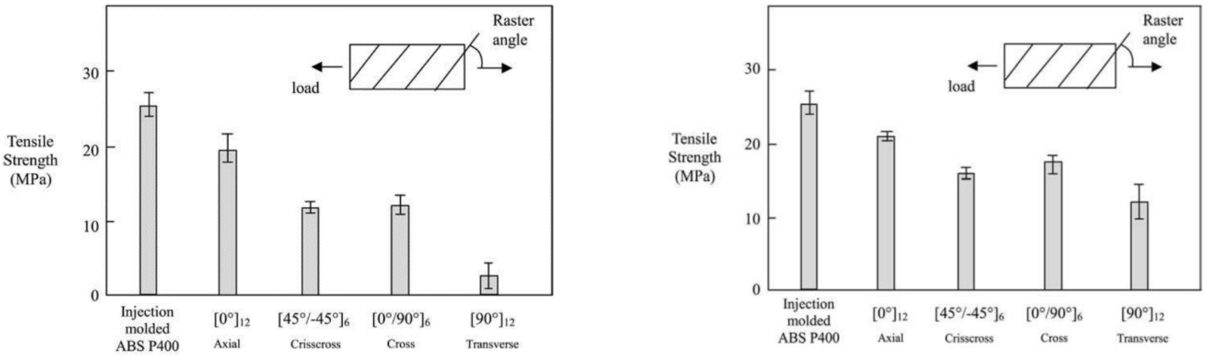

Fig. 5. Tensile strength with various raster (ZERO air gap in left and -0.003 inch in right) compared with injection molded ABS P400 [31].

So, in both conditions of air gap, the comparing of the tensile strengths (T.S) showed below trend:

$\text{T.S}_{\text{Injection molded}} > \text{T.S}_{[0°]} > \text{T.S}_{[0°/90°]} > \text{T.S}_{[45°/-45°]} > \text{T.S}_{[90°]}$

It is stated the both of strength and stiffness were increased, under condition of negative air gap. The tensile strength of the prepared Axial ([0°]) specimens didn't increase much under negative air gap. The effect of build direction on compressive strength was studied. Specimens were under compression test with zero air gap and fixed raster angle of [45°/-45°]. It was concluded that the compressive strength was greater than the tensile strength. To addition, the axial specimen showed fifteen percent higher compressive strength, in comparison with the transvers specimens. So, build direction didn't have significant impact on the compressive strength [31].

Bagsik et al. [32], used the PEI (Polyetherimide) as the raw material and printed some samples in the three directions X, Y, and z corresponding to the edge, flat and up respectively, according to Fig. 6, to study the effect of the build direction on the mechanical strength of the printed specimens. The tensile test was performed to evaluate the effect of the build direction.

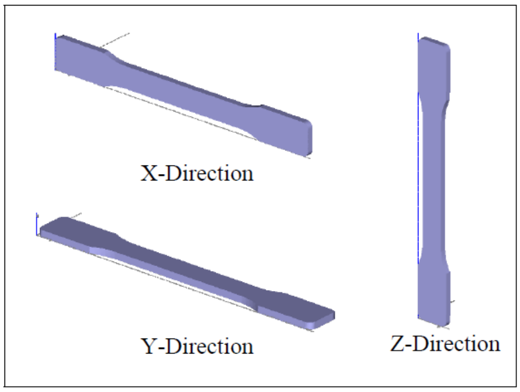

Fig. 6. Build Direction of Specimen for Tensile Test [32]

It was found that the highest strength was obtained by the specimens, which were manufactured in X-direction, then in Y-direction and then in the Z-direction. As the reason, it was stated that, the applied tensile stress influences the existence weld between the layers, which were not strong enough to be able to resist the applied tensile loading. But in case of the X- and Y-direction, the applied stress, effect on the structure in the layer direction. Then as the effect of the air gap and thickness of the used filaments, three stated build directions (X, Y and Z), negative air gap caused the best results (mechanical strength properties). Using the thicker filaments, were resulted in better mechanical data for X and Z build directions. But the thinner used filament, could improve the tensile strength of the Y- specimens.

As mentioned in the bibliography it was understood that parameters of FDM process have significant effect on mechanical properties of the final printed objects. The categorizing of the different parameters, have been done according to their importance, during the different researches. The effect of the five parameters of the process, namely layer thickness, part orientation, raster width, raster angle and air gap on mechanical behavior of specimens were studied [33 and 20]. According to Godfrey et al. [20], the minimum layer thickness can help improve the tensile strength. Negative air gap improves considerably the tensile strength. The minimum of raster width improves the tensile strength. It was stated that the part orientation has a significant role on tensile strength. In zero-part orientation, when the layers are parallel to the direction in which load is applied, the maximum tensile strength is obtained.

Ziemian et al. [19 and 34] during their focus on the experimental study of the effect of raster angle, stated that for achieving the highest tensile strength, the raster should be in direction of the longest dimension. Four raster angle (raster orientation) were considered and their effect on the tensile strength of printed samples were studied [34]. The four raster orientation were, longitudinal (0°), diagonal (45°), transverse (90°) and default (+45°/-45°). The reported results of tensile test are shown in the table 3.

Raster Orientation	**Mean Yield Strength (MPa), Std Dev**	**Mean Ultimate Strength (MPa), Std Dev**	**Mean Effective Modulus (MPa), Std Dev**
Longitudinal (0°)	25.51, 0.73	25.72, 0.91	987.80, 19.98
Diagonal (45°)	15.68, 0.27	16.22, 0.27	741.78, 20.28
Transverse (90°)	14.35, 0.08	14.56, 0.05	738.77, 7.91
Default (+45°/-45°)	18.90, 0.53	19.36, 0.39	768.01, 33.31

Table 3. Tensile test results [34].

So, as is clear, as raster aligned in direction with the longest dimension, the tensile strength increased. The fracture surface of tested specimens was studied in both of Macroscopic and Microscopic viewpoints, too. The Macroscopic fracture surface is Fig. 7.

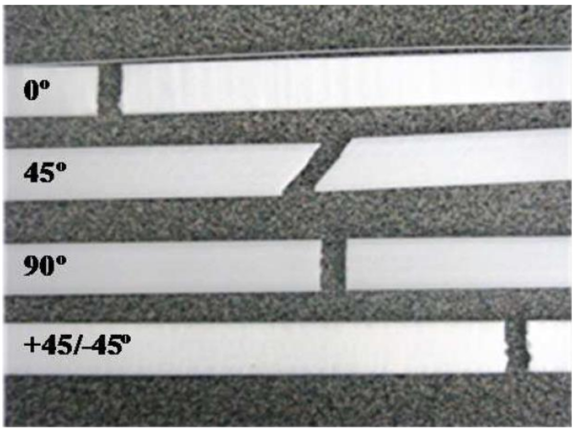

Fig. 7. Failure modes of the specimens with each of the four raster orientations [34]

According to Fig. 7, The longitudinal specimens, failed in transverse direction, primarily. But it was reported that some pull out of fibers and delamination intermittently evident was observed, too. The transverse specimens, failed in direction with raster orientation, which was 90°. The diagonal specimens were failed in direction with the raster orientation which was 45°. The specimens with default orientation (+45°/-45°), failed along +45° and -45° paths, which was in result of saw-tooth patter across the width of specimen. It is stated that the fracture path maybe is controlled by weak interlayer bonding which is due to residual stress from the volumetric shrinkage of the polymer layers during cooling and solidification. In addition, existence of air gaps and interlayer porosities, have an effect to reduce the load-bearing area between the layers and cased easy fracture path [34].

The Microscopic analysis of fracture surface was done, too. It has been stated that in case of 0°-orientation, the failure surface was predominantly brittle, with localized micro-shearing on each fiber face, according to Fig. 8. The tensile strength of 0° specimens, stickily was depended on the strength of monofilament (which was ABS filament in this research).

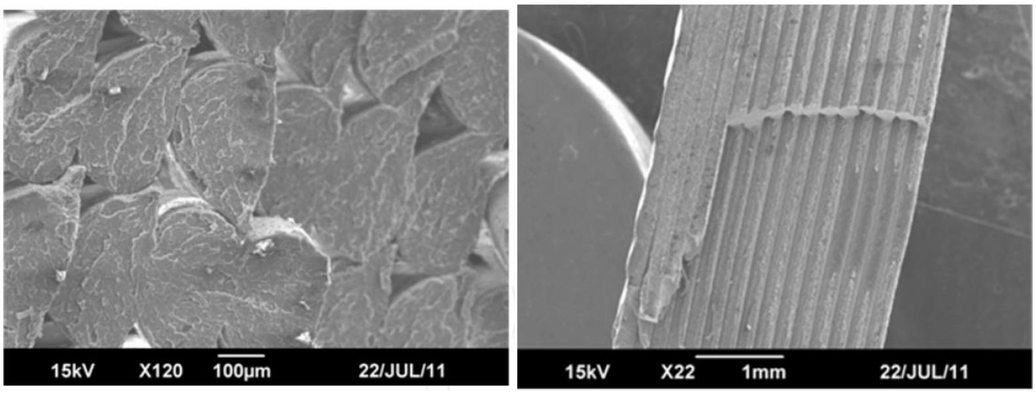

Fig. 8. SEM image of fracture surface of a 0° raster (left) and 90° raster (right) specimen [34]

According to the Microscopic analysis of fracture surface of 90° specimens (Fig. 8, right picture), It has been stated that the obvious crazing wasn't observed during the tensile test. It was stated that failure occurred between layered ABS filament, according to Fig. 8. According to the microscopic analysis of fracture surface of +45°/-45° specimens, multiple failures of both shear and tension were revealed on individual raster fibers, according to Fig. 9a. Microscopic image of 45° specimens, displayed a brittle shear failure on each fiber. In fact, each raster was pulled during the tensile test, then failed at 45 degrees relative to axis of applied load (Fig. 9b).

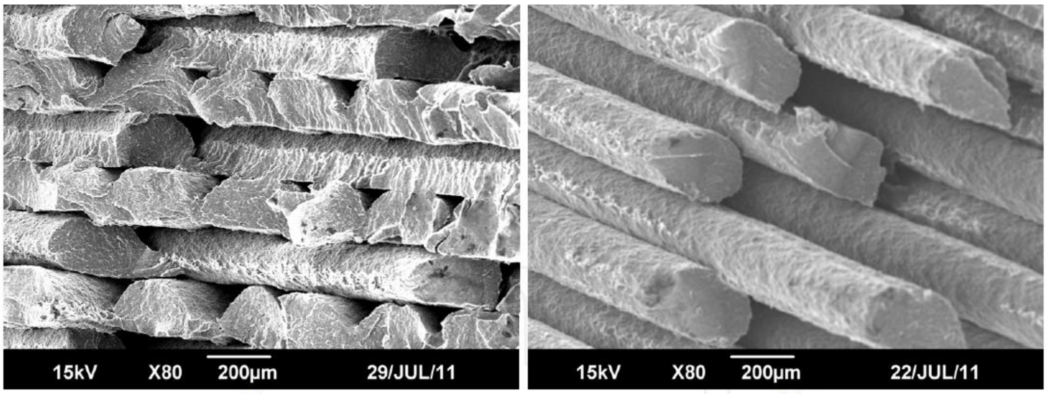

(a) (b)

Fig. 9. SEM image of fracture surfaces of (a) +45°/-45° and (b) 45° raster specimen [34]

Fatimatuzahran et al. [1], studied on the effect of the raster angle on the mechanical behavior of the printed samples, by use of ABS polymers, as raw material. As the tensile test results of prepared samples under crisscross (45°/-45°) and cross (0°/90°) orientations, the cross samples showed higher maximum stress than crisscross structures. But the distinctions weren't significant. It has stated that, when cross samples were applied tensile test, the 0° surface structure pulled in parallel direction of the tensile test. So, this 0° surface structure is one support, which caused higher tensile strength of cross samples. It was stated that 45°/-45°

(crisscross) samples, had more surface roughness at their edge, which were stress concentrator and resulted in easier fracture in comparison with cross (0°/90°) samples. This reason was considered as the main reason of the achieved higher tensile strength of cross samples during the applied tensile test. In addition, it was reported that the crisscross samples have showed more flexural strength, in comparison with cross samples. It was stated that, the layers are zero and ninety degrees in cross samples, so the orientations were parallel and perpendicular with the applied load. But in case of crisscross samples, the layers were neither perpendicular nor parallel with applied load in flexural test. So, that’s why, crisscross samples showed more flexural strength in comparison with cross samples. By the way, according to the SEM figures (Fig. 10) of the cross section view of crisscross and cross samples, the internal air gaps of crisscross samples were less than cross ones. So, the crisscross samples were more compact and dense in comparison with the cross samples.

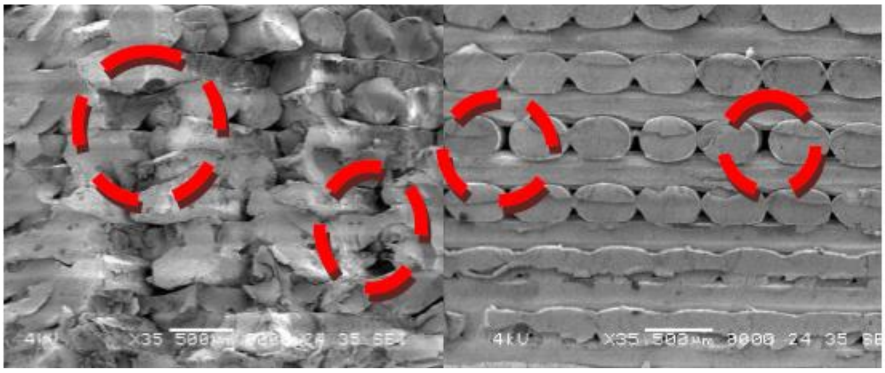

Fig. 10. Cross section view 45°/-45° (left) and 0°/90°(right) [1]

According to Ang et al. [35], air gap and raster width are the most remarkable variables in FDM process, which influenced on the porosity and mechanical properties of the printed specimens, by FDM. During the bibliography, it was found that the used machine affects the mechanical properties of the printed samples. For example, Tymrak et al. [36] and Alvarez et al. [37], used the same polymer to prepare some specimens but by means of the different printing machines, while the mechanical properties of the printed samples were different in comparison with each other.

Mostly, the thermoplastic polymers, which are amorphous polymers or those have the low levels of crystallinity are used for FFF. The main stated reason of this policy is due to the low degree of polymer shrinkage exhibition, which is essential to have accuracy in the produced components by 3D printing methods. One of the new novelty and advantage of additive manufacturing (AM) is the presence of the opportunities for recycling the thermoplastics for use as consumable additive manufacturing feedstock materials, so this policy- which is the using of the waste thermoplastic materials in accordance to the manufacturing the composite- could increase the value of polymers by enhancing their mechanical and properties. Fiber reinforcement was observed to prepare benefit of strength and shrinkage [38]. Addition to the strength desire, the reinforcements are added to conquer the non-printability regarding high coefficient of linear thermal expansion [38, 39].

2.3 FFF process in composites-based polymers

2.3.1 Powder reinforced polymers

Nikzad, et al. [40], used three types of materials as the development of the new powder reinforced composite materials by the FFF process. The main reason for using powder as a reinforcement (filler) is to improve the electrical properties and thermal conduction (using metals powders). The powders, which were utilized as reinforcement (filler) for improving the electrical or thermal conduction, often reduce the strength of the materials. Therefore, they are not often considered as mechanical reinforcements in polymer composite materials.

The first used material was Acrylonitrile Butadiene Styrene (ABS) thermoplastic, as the matrix. Other used ones were two composites used as feedstock materials, which were copper powder mixed in ABS matrix and another one was iron powder mixed in ABS matrix. According to characterize the related viscoelastic properties of these developed composites materials as feedstock in the FFF process, Dynamic Mechanical Analysis (DMA) technique has been used. The varying volume fractions of metal powders (5%, 10%, 20%, 30%, and 40%) were used according to produce the appropriate feedstock filament. The related shape of the used powder particles was spherical for copper and irregular for iron. The purity of both used powder (copper and iron) was 99.7% with two particle sizes of 10 µm and 45 µm for copper and one particle size of 45 µm for iron powders (Table. 4).

Composite designation	**Matrix**	**Metal filler type**	**Filler size (µm)**	**Filler loading (%)**
A1	ABS	Cu	10	5
A2	ABS	Cu	10	10
A3	ABS	Cu	10	20

A4	ABS	Cu	10	30
A5	ABS	Cu	10	40
B1	ABS	Cu	45	5
B2	ABS	Cu	45	10
B3	ABS	Cu	45	20
B4	ABS	Cu	45	30
B5	ABS	Cu	45	40
C1	ABS	Fe	45	5
C2	ABS	Fe	45	10
C3	ABS	Fe	45	20
C4	ABS	Fe	45	30
C5	ABS	Fe	45	40

Table 4. Metal/polymer composites constituents [40]

Fig. 11(a) is related to the variation of the measured thermal conductivity of the copper composites of the large used particle sizes with different copper content at different temperatures. According to Fig. 11, the observed temperature increase had a negligible influence. However, in the case of sample B4, which was related to the high concentration of the copper particles (30 vol. %), an obvious thermal conductivity increase, above the glass transition temperature of the matrix was observed. The increase of the particle’s mobility at the beyond the temperature of the matrix glass transition was reported as the reason.

The lower concentration of the copper particles up to the volume fraction of 10% (samples B1 and B2), could not useful, according to improve the thermal resistance of the ABS matrix. In the case of the volume fraction of 20%, the conductive chains of the copper were formed. In the other words, the volume fraction of the 20% copper powders was required to achieve a percolation concentration. This formation and its related effect on the thermal resistance were more tangible in the case of 30% volume fraction. As for the reason, easier mobilization thanks to the matrix state change from the solid to the liquid state at the above glass-transition temperature of the matrix.

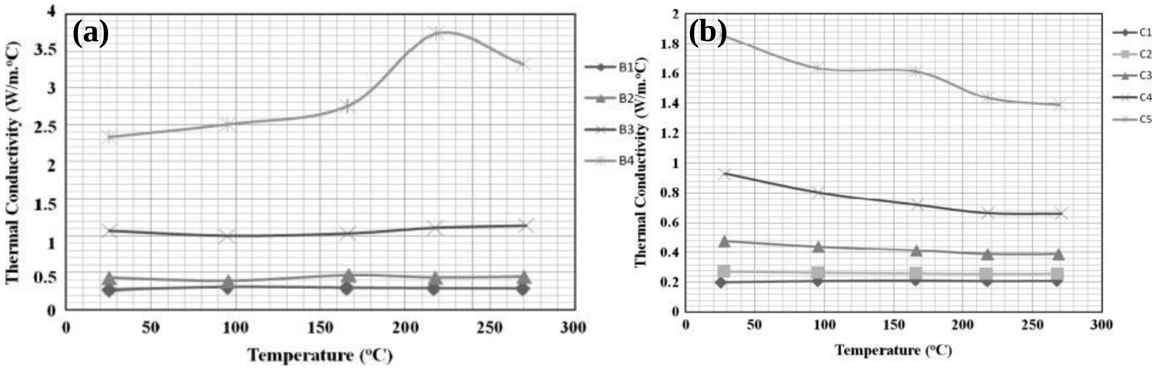

Fig. 11. Thermal conductivity of (a) copper-filled ABS and (b) iron-filled ABS composites at various temperatures [40].

According to Fig. 11(b), as the comparison of the effect of the iron and copper as the used reinforcements of the ABS matrix on the thermal conductivity of the fabricated composites, it was clear that the iron particles had lower influence. The effect of iron particles was sensible when the related particle concentration reached the 30% volume fraction (sample C4).

Fig. 12(a) is related to the dynamic mechanical result of the ABS reinforced by the used finer copper particle size. It was observed that below the glass-transition temperature, as the volume fraction of the used filler was increased, the storage modulus of the composite was increased, too. The trend was continued up to 30% of the filler volume fraction (sample A4). Nevertheless, the storage modulus of the composite was decreased as the volume fraction of the filler was increased by more than 30%. The agglomeration of the used reinforcement particles (sample A5) and accumulating of the voids have been stated as reasons for the weakening of the ABS matrix by the used finer copper particles, instead of strengthening the matrix.

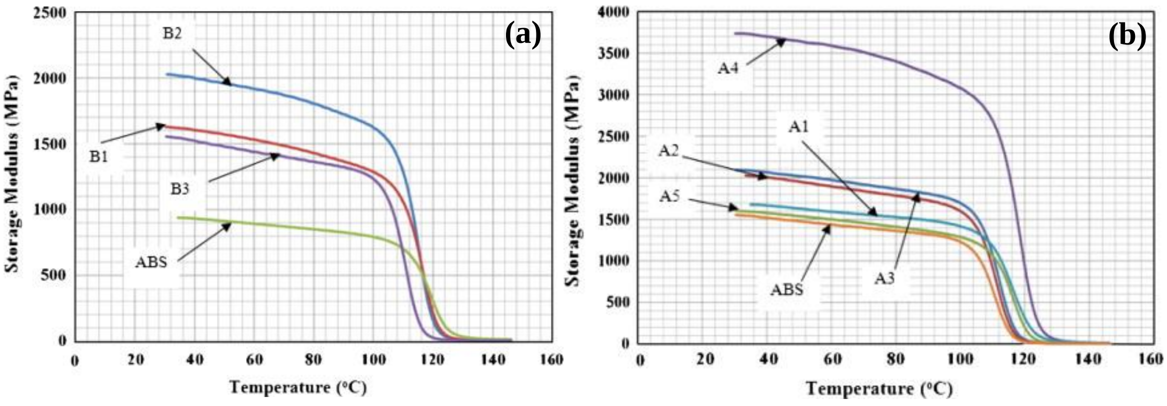

Fig. 12. The storage modulus of various Copper/ABS composites with the copper particle size of (a) 10 nm and (b) 40 nm at the different temperature values [40]

Fig. 12(b) shows the dynamic mechanical result of the ABS reinforced by the used coarser copper particle size. The storage modulus of the composite was increased as the volume fraction of the filler was increased up to 10%. However, the stated trend was inverted as the filler fraction was increased more than 10%. The weaker interlock of the filler matrix and the inappropriate distribution of the used fillers in the matrix were stated as the reason. In fact, the maximum achieved storage modulus in the case of the used larger copper particles was about 2 GPa, while it was reported about 3.5-4 GPa, in the case of the used finer copper particles as reinforcements.

Fig. 13 presents the dynamic mechanical result of the ABS reinforced by the used iron particles. The effect of the iron particles was considered up to 30% volume fraction, which caused the range of the 2.5-3GPa as the storage modulus (stiffness) of the fabricated composite. The stiffness values of the Iron/ABS composites were higher in comparison with the same used particle size of the copper as reinforcement, under the 10–20% volume fraction condition of the fillers.

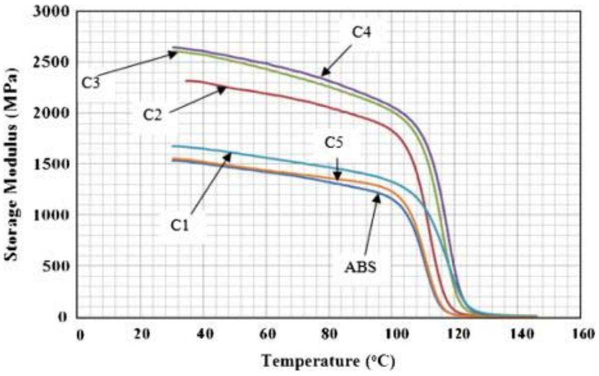

Fig. 13. The storage modulus of various Iron/ABS composites with the iron particle size of 45 μm at the different temperature values [40]

Hwang et al. [41] studied the thermo-mechanical properties of the developed metal/polymer composite and the printing parameter, by the FFF process. The used metal powders were copper and iron with the size of 24 μm and 34 μm, to reinforce the ABS matrix. The loading deal of the metal particles was varied to study the effects of the used metal powder on the mechanical behavior of the fabricated filament. It has been reported that by the increase of the metal content, the tensile strength of the specimens was decreased. As finding it reason, the microstructure of the cut plane of the printed specimens (ABS-CU composite) was observed (Fig. 14). It was observed more voids in the case of the 30 Wt. % of the copper particles in comparison with the use of the 10 Wt. % of copper particles. These voids caused the lower bonding between the layers, then the lower tensile strength of the specimens with 30 Wt. % copper particles in comparison with specimens with 10 Wt. % copper particles. In addition, the thermal conductivity of the prepared metal/polymer composite was progressed and improved by the increase of the metal content.

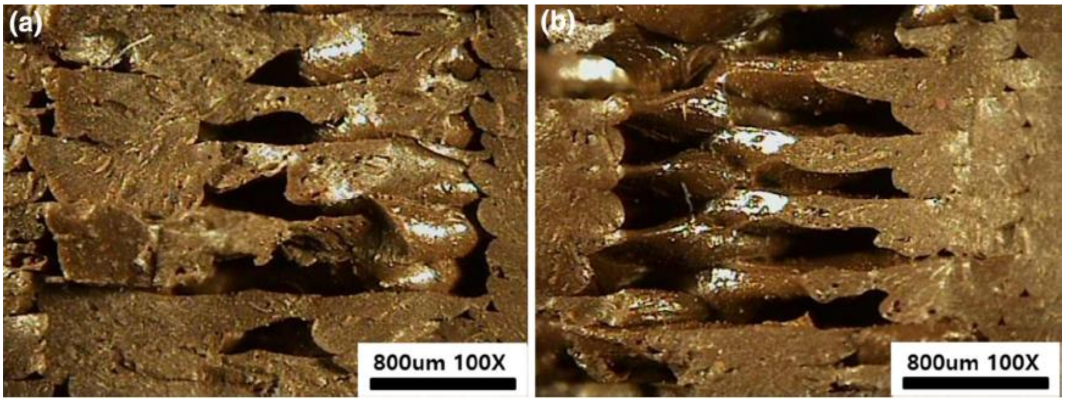

Fig. 14. The microscopic structure of cutting plane of specimens: (a) ABS-Cu10 wt. % and (b) ABS-Cu30 wt. % [41]

Isakov et al. [42], could improve the dielectric permittivity by adding $BaTiO_3$ and $CaTiO_3$ into the polymer matrix (ABS and PP) by the FFF process. Also, Shemelya et al. [43], could improve dielectric permittivity, X-ray attenuation factor, and impact resistance of PC (polymer matrix) by adding the Tungsten particles.

Boparai et al. [44] studied the tribological properties of the fabricated ABS and Nylon 6-Al-Al_2O_3, by the FFF method. As for tribology characterization, the wear test was carried out on the related FFF manufactured specimens with the dimensions of 10 mm as diameter and 30 mm as length. The wear test was performed following ASTM G 99 standard at room temperature. This research illustrated that the use of Al and Al_2O_3 as fillers could develop the wear properties, by comparison of the printed Nylon 6-Al-Al_2O_3 and the printed ABS parts. The related particle size of the used Al and Al_2O_3 were 41-44 μm and 125-149 μm, respectively. As the tribological test, the different loads were applied during 5 and 10 minutes at 1.36 (m/s), as sliding velocity. In the case of the fabrication of the nylon 6-Al-Al_2O_3 up to 40% of the filler materials (Al_2O_3 and Al) were used, as the filler of the nylon 6 matrix.

Table 5 shows the composition of each printed type of the nylon 6-Al-Al_2O_3 composites and the respective MFI of each composition. Indeed, the rheological behavior of composite material with consideration of temperature and viscosity within processing in the liquefier head section of FFF was studied employing the melt flow index (MFI) test. The MFI is introduced as an alternative measure of viscosity for comparative purpose. It is defined as the amount of the related polymer in ‘gm’ extruded in ‘10’ min via a capillary of standard dimensions (diameter 2.0955 ± 0.0051 mm and length 8.0 ± 0.025 mm), according to ASTM D1238–73 standard.

It has been reported that the MFI values of each composite were decreased by the decrease of Al and the increase of Al_2O_3. The increase of the amount of the large particle size in the reinforced matrix was stated as the decrease of the MFI value.

Composition	**Nylon 6**	**Al**	**Al_2O_3**	**MFI**
A	60	26	14	2.19
B	60	28	12	2.25
C	60	30	10	2.31

Table 5. Weight proportion and MFI of different compositions [44]

In addition, it has been understood that as the content of Al_2O_3 in the printed composites was decreased, the related material loss to the wear was increased, according to table 5.

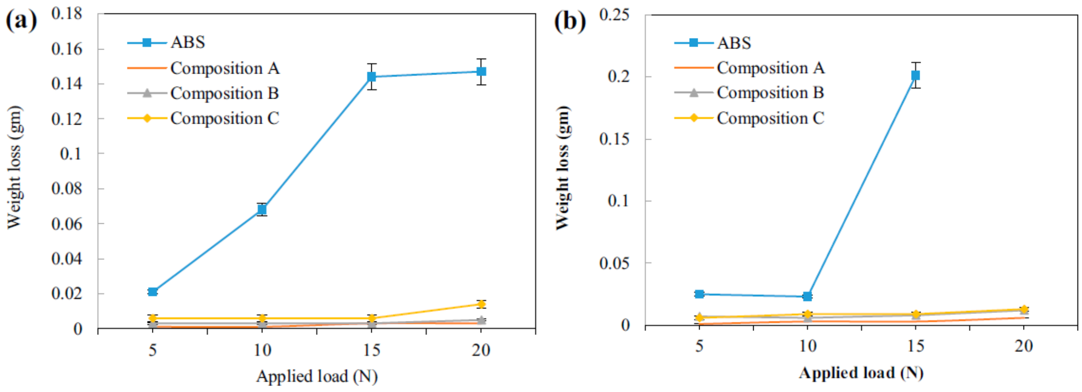

Fig. 15. Material weight loss with applied load for (a) 5 minutes and (b) 10 minutes, obtained from tribology evaluations [44]

It was stated that the ABS material had more friction force under all conditions, in comparison with composite ones. In fact, the presence of the Al_2O_3 in the reinforced nylon composites introduced such as the bearing, caused less material loss, too. So, because of the stated property of the existence of Al_2O_3 particles, the composition “A”, had the lowest friction load in comparison with the other compositions (B and C), according to Fig. 16. Also, the printed composites had the lower friction coefficient in comparison with the fabricated ABS parts. It was observed that the friction coefficients of the composite materials were changed, slightly by varying the applied load and duration.

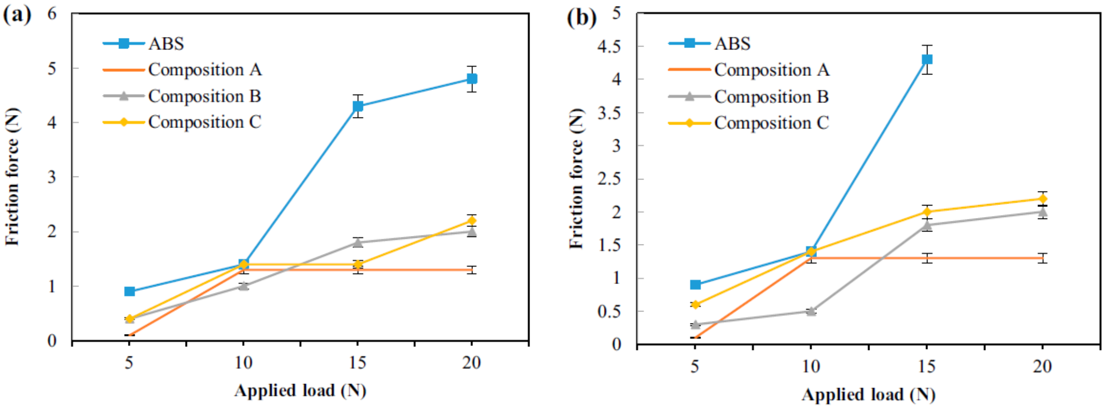

Fig. 16. Obtained curves related to friction force with applied load for (a) 5 minutes and (b) 10 minutes on ABS, nylon 6-26 Al-14 Al_2O_3 (composite A), nylon 6-28 Al-12 Al_2O_3 (composite B), and nylon 6-30 Al-10 Al_2O_3 (composite C), from tribology evaluations [44]

SEM observation revealed that in the case of the comparison between the printed nylon 6-Al-Al_2O_3 and ABS parts, the composite ones had higher wear resistance, thermal stability, and stiffness (Fig. 17).

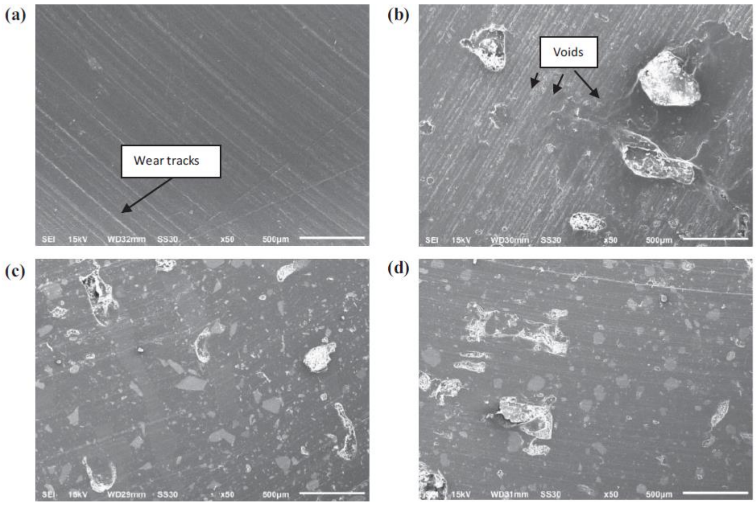

Fig. 17. SEM images of (a) ABS material, (b) composition 'A', (c) composition 'B' and (d) composition 'C', obtained from tribological observations [44]

2.3.2 Fused Filament Fabrication of fiber-reinforced polymers

2.3.2.1 Continuous fiber-reinforced

The strength of polymeric composites is mainly dependent on their two important components, which are the polymer matrix and the used reinforcement(s). In fact, the strength of polymeric composites, mainly originates from two aspects. First, the individual consideration, which is the strength of polymer matrix side and used reinforcement(s) side, separately. The second aspect is the related consideration of the collaboration of these two components, in the unique manufactured materials as composites, such as their adhesion. Between the two stated considerations, the second one sometimes is possible to be manipulated. In the case of the used 3D printer, which have one nozzle, different methods according to increase the impregnation of the fibers have been reported such below:

- Heating the fibers before entering to the nozzle, to increase the permeation of polymer [45].
- Heating of the used polymer (matrix) and passing the reinforcement through the polymer matrix, which has been in the molten state [46].
- Modification of the fibers by chemical solution before the feeding (sizing agent) [47].
- Printing without any heating and modification of the used fibers [48].

Matsuzaki et al. have studied the manufacturing of the PLA-continuous carbon composite by FFF. They have heated the fiber for fusing the fiber surface with polymer matrix in synchronized fiber and polymer filament feeding (one-nozzle 3D printing machine), according to Fig. 18. In fact, the used fibers have been heated before entering the nozzle, by nichrome wire. It has enhanced the infiltration and permeation of the carbon fiber bundle with used PLA resin. The heat has diffused to the resin, decreased viscosity of the PLA, and caused the increase in the tensile strength [45].

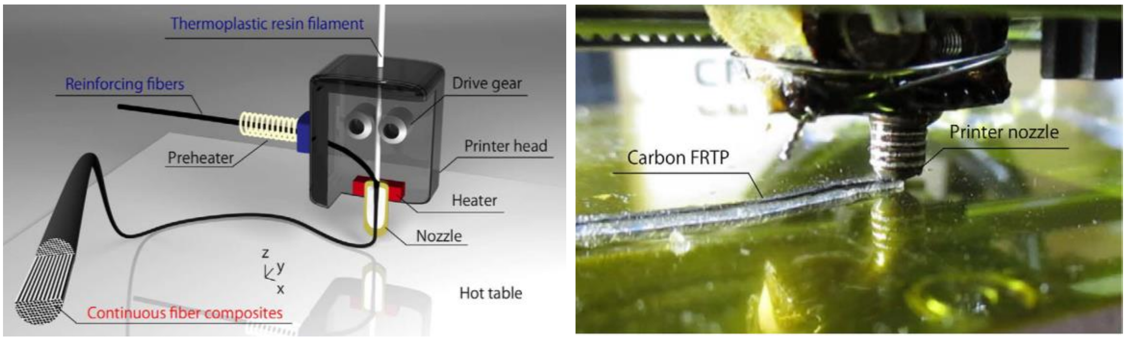

Fig. 18. Schematic of the 3D printer head used to produce continuous FRTPs using in-nozzle (Left) and photograph of the 3D printing of a CFRTP (Right) [45]

Haoa et al. [46] studied the continuous carbon fiber reinforced thermosetting composites by FFF. An epoxy resin (E-54(616)) was utilized as the thermosetting matrix material; also as for reinforcement, a carbon fiber bundle (HF10, 3000 fibers in a bundle) was applied. It is stated that the high costs related to manufacturing of the continuous carbon fiber reinforced thermosetting composites restrict their use in the automotive industries, but these materials have a wide application in astronautics and aeronautics, thanks to their special properties and behaviors, such as good corrosion resistance, good fatigue behavior, high specific stiffness, and high specific strength [49]. Therefore, the approaching of the new low-cost methods of manufacturing of these composite structures will attract the industrials' attention. The used method was proceeding the fiber bundle through the pool of epoxy and then entering the printing head. After printing onto the building platform, the specimens were cured in high-temperature chamber. The composites lamina, honeycomb, and grid were manufactured, as was stated, according to Fig. 19.

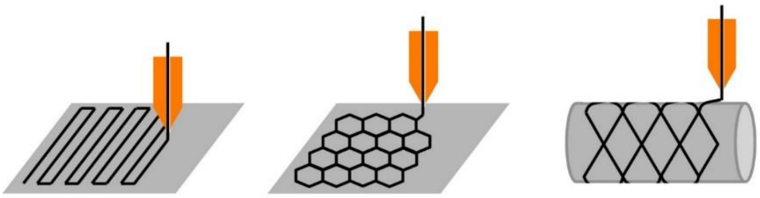

(a) Printing of the lamina (b) Printing of the honeycomb (c) Printing of the grid

Fig. 19. Scheme for the printing process [46]

Finally, the tensile and three-point bending behaviors of the printed composite lamina were characterized, therefore the fiber orientation of the three-point bending and tensile tested specimens were according to the lamina pattern (Fig. 19 (a)). The dimensions of the printed samples for the stated mechanical tests were 250 mm × 25 mm × 3 mm. The flexural strength and its related elastic modulus were 202 MPa and 143.9 GPa, respectively. In addition, the tensile strength and its related elastic modulus were 792.8 MPa and 161.4 GPa. These results were compared with similar printed reinforced thermoplastic composites and printed short carbon fiber reinforced thermosetting composites. The failure mechanism of the printed composite lamina was studied. The failure was started by in-plane matrix cracking. Then, the crack has expanded with an increase in the applied load. Eventually, the separation of the layers occurred, and the fiber and the matrix were debonded, which caused partial fiber breakage. The fractography of the printed continuous carbon fiber reinforced thermosetting composite lamina specimens were performed after tensile and three-point bending tests. The fractography was done by use of SEM observation of the fractured cross-section of the tested specimens (Fig. 20). The fiber breakage was started as the related dominant failure mode of the fiber-reinforced thermosetting composites. However, the fiber pull-out was stated as the dominant failure mode of the manufactured reinforced thermoplastic composites by 3D printing (according to [47]).

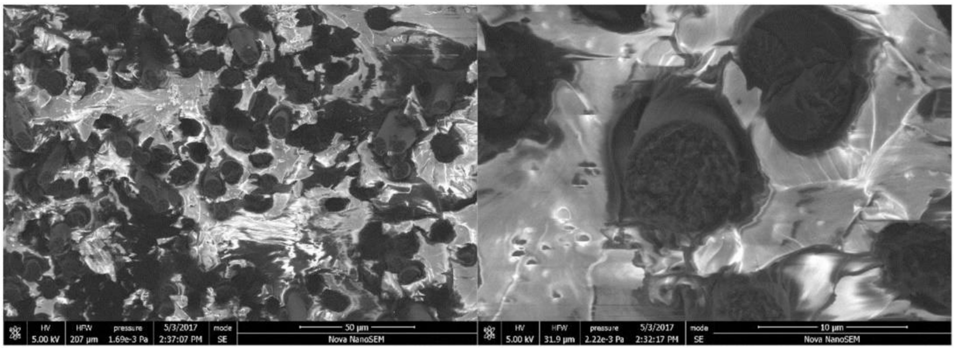

Fig. 20. SEM images of the fractured cross-sections related to epoxy resin (E-54(616)) reinforced with continuous carbon fiber composites [46]

In another study, Akhundi et al. studied the manufacturing of the PLA-continuous fiber (here, glass fiber yarn) composite part by FFF. In fact, the continuous glass fiber yarn entered polymer, which were molten in the nozzle, so the yarn was coated and partially impregnated with molten used PLA, as has been stated. It was concluded that the mechanical properties of produced composite by FFF was depended on the fiber volume content. It was noted that it is important to maximize the content of the fiber-volume to produce the composite part with high strength and modulus and then, to increase the accuracy of the prediction of the printed composite [50].

Nanya Li et al. [47] applied modification on carbon fiber bundles, which were reinforcement components of produced composite by infiltration in PLA sizing agent before the printing as the manufacturing process, to improve the mechanical properties. In fact, the used 3D-printing machine was a one-nozzle setup (according to Fig. 21) and the applied approach for fiber impregnation was "Modification of the fibers by chemical solution, before the feeding".

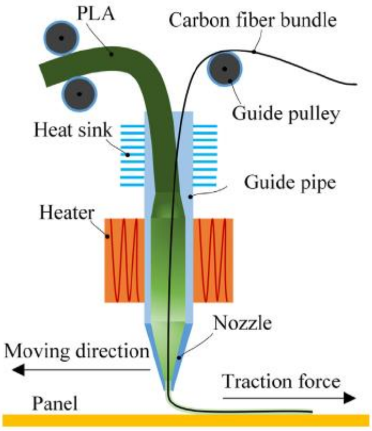

Fig. 21. Schematic of the designed extrusion device to printing continuous carbon fiber reinforced PLA [47]

Printed samples under three different conditions, which were PLA, carbon fiber reinforced PLA and modified carbon fiber reinforced PLA were produced. Then, the printed samples were characterized by mechanical tests.

According to Table 6, the flexure strength of the original carbon fiber was so close to the PLA samples. But the modified carbon fibers showed more strength (about 164%) than the original composite. As a reason, it was stated that this observation could be attributed to the reason that the three-point bending test and flexural property is affected by interfacial strength between matrix and reinforcement, significantly. In addition, the tensile strengths of the two kinds of carbon fiber composite (with and without modification), were significantly more than PLA printed samples.

Mechanical properties	PLA	Carbon fiber reinforced PLA	Modified carbon fiber reinforced PLA
Tensile strength (MPa)	28	80	91
Flexure strength (MPa)	53	59	156

Table 6. Statistic results of tensile and flexure strength of three different samples [47]

As the SEM observation, the microstructure of the original carbon fiber and modified carbon reinforced composites, before and after tensile test have been compared (Fig. 22). According to Fig. 22(a) and (b), the stronger interface and better wetting of carbon fibers by PLA resin, due to the applied modification was clear. According to Fig. 22(b), there are just small bridges between fibers (yellow circle), which transfer the loads between fibers. By the way, there were many voids between carbon fibers, which are representative of poor infiltration of PLA and fibers. On another hand, the higher infiltration and more bonding of matrix and modified carbon fiber are visible in Fig. 22(e). Finally, as for a comparison of the fractured surfaces of two kinds of original and modified composites (Fig. 22(e) and (f)), the complete coated fibers (cracked fibers) by PLA resin, were rare. On the contrary, most of the carbon fibers were completely coated by PLA resin, and the significant separation of fiber and matrix was not observed. This observation has been stated as the reason for the remarkable difference in flexure strength of the original carbon fiber composite and modified ones, which were studied [47].

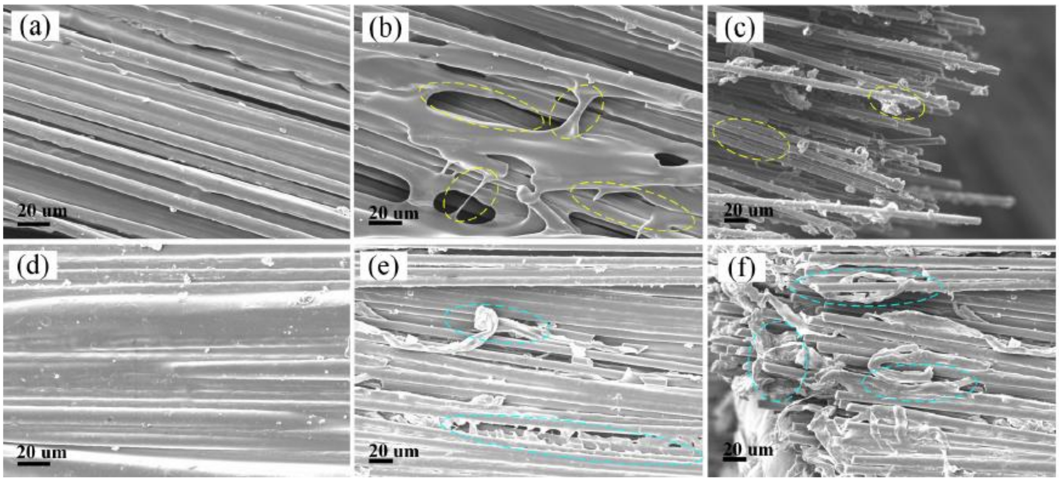

Fig. 22. SEM micrographs of printed composites, (a) fiber-matrix interface of carbon fiber reinforced PLA specimen, (b) carbon fiber reinforced PLA specimen after tensile test, (c) fiber pull-out of the specimen after tensile test, (d) fiber-matrix interface of modified carbon fiber reinforced PLA specimen, (e) modified carbon fiber reinforced PLA specimen after tensile test and (f) fiber pull-out of modified carbon fiber reinforced PLA specimen after tensile test [47]

Tian et al. [48] studied the continuous carbon fiber reinforced PLA composites, in which the reinforcement and PLA filament have been fed into the FFF machine, simultaneously. They studied the five parameters, which have affected the pressure and temperature of the fabricated PLA composite. The chosen parameters were temperature of liquefier, layer thickness, feed rate of filament, hatch spacing (which was introduced as the central distance between two adjacent lines) transverse movement speed. As the parameters were changed, the mechanical performance of manufactured specimens was changed. The obtained flexural strength and modulus from the 3-point bending test, as the criteria of the mechanical properties, were considered to optimize the stated selected parameters of the process.

The study on the effect of liquefier temperature was done in the range of 180-240 °C, in which the melting flow index of PLA at the temperature of 180 °C and 240 °C, were measured 2 g/10 min and 36 g/10 min, respectively according to the Fig 23.

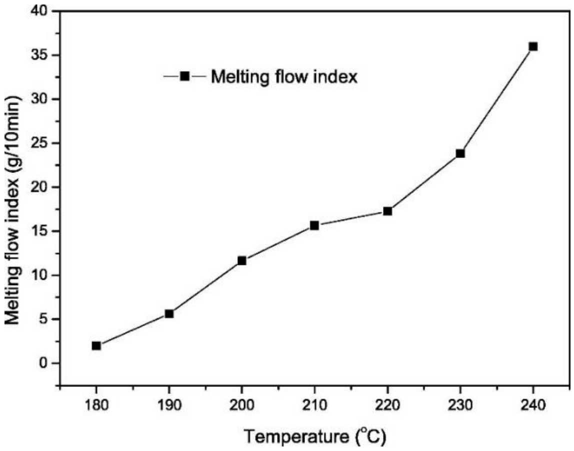

Fig. 23. Melting flow index of PLA with temperature from 180 °C to 240 °C [48]

The related results of the evolution of the flexural strength and modulus were reported in Fig. 24. Therefore, the flexural strength and modulus were increased as the temperature was increased (in the selected temperature range). The maximum flexural strength and modulus were related to the 240 °C, which were 155 MPa and 8.6 GPa, respectively. However, it was reported that the surface accuracy of the manufactured specimens, due to the overflow of molten PLA, was lost. So, as the optimizing the lower temperature, which was 230 °C was reported, according to have high flexural strength and modulus, and the reasonable surface accuracy. Normally, the final printed parts with a smoother surface and also without deflection and distortion are considered as desired printed parts in viewpoints of reasonable surface and dimension accuracy.

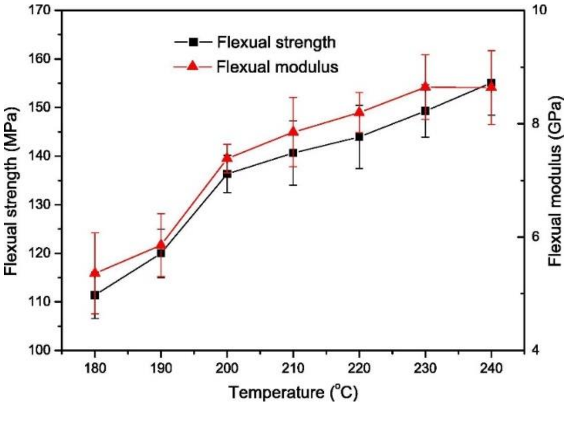

Fig. 24. Effect of the liquefier temperature on the flexural strength and modulus of 3D printed continuous carbon fiber reinforced PLA composites [48]

More details from the effect of temperature on the mechanical properties have been achieved by studying the multiple interfaces, which were the interfaces between fiber and matrix. Deposited adjacent lines and layers.

It was observed that the delamination was prepared between layers, because of inadequate bonding in the lower temperature of liquefier (180 °C) according to Fig. 25(a). But, by increasing the temperature up to 240 °C, no interface between the layer were not observed, because of increase of flowability of melt plastics by temperature (Fig. 25(d)). As an observation of the interface between the matrix and fibers, the impregnation of the matrix into the fiber bundle wasn't occurred in the lower temperature (180 °C) according to the Fig. 25(b), but by increasing the temperature up to 240 °C, the impregnation of PLA into the carbon fiber bundle was achieved (Fig. 25(e)). As the reason, by increasing the temperature, the melt flow index of the matrix was increased. It was observed that the matrix was broken first and could not transfer the applied load to the reinforcement fibers at lower temperatures. The fibers were pulled out (Fig. 25(c)). However, by increasing the temperature, the pattern of the fracture was changed, in which the fiber bundle breakage was observed (Fig. 25(f)). Therefore, that is why the flexural strength was increased by temperature increase.

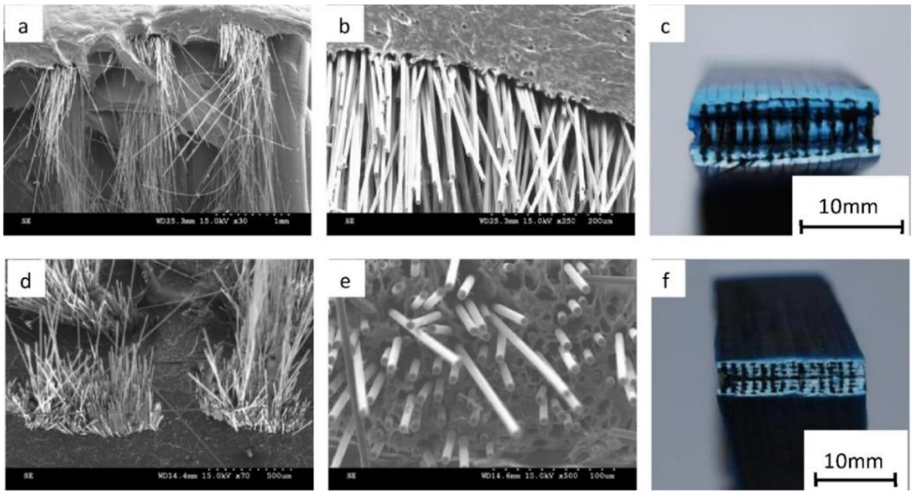

Fig. 25. Microstructures of the obtained fractured cross-section from the applied flexural test on the carbon fiber PLA composites with liquefier temperature of 180 °C (a, b, c) and 240 °C (d, e, f), respectively: (a) and (d) overall cross-section, (b) and (e) interface, (c) and (f) fracture pattern [48]

As the study on the layer thickness parameter, the thickness of 0.3 mm to 0.8 mm was selected [48]. The flexural strength was decreased by an increase in thickness value, according to Fig. 26.

In fact, the tight space for the just deposited melt materials and increasing of the contact pressure between the nozzle and surrounding deposited lines were prepared, by decrease of the layer thickness. As more detail, the microscopic observations were applied. In the case of the smaller thickness (0.5 mm), it was observed that the homogenous bonding between the layers without obvious delamination in the interfaces was achieved (Fig. 26(a)), also the carbon fiber bundles were impregnated with matrix (Fig. 26(b)), and the load was transferred from PLA to carbon fibers, as was revealed during the fractography. However, in the case of the larger layer thickness (0.7 mm), the weaker bonding (Fig. 26(d)), inadequate impregnation (Fig. 26(e)), and fiber pull-out and shear delamination were observed (Fig. 26(f)).

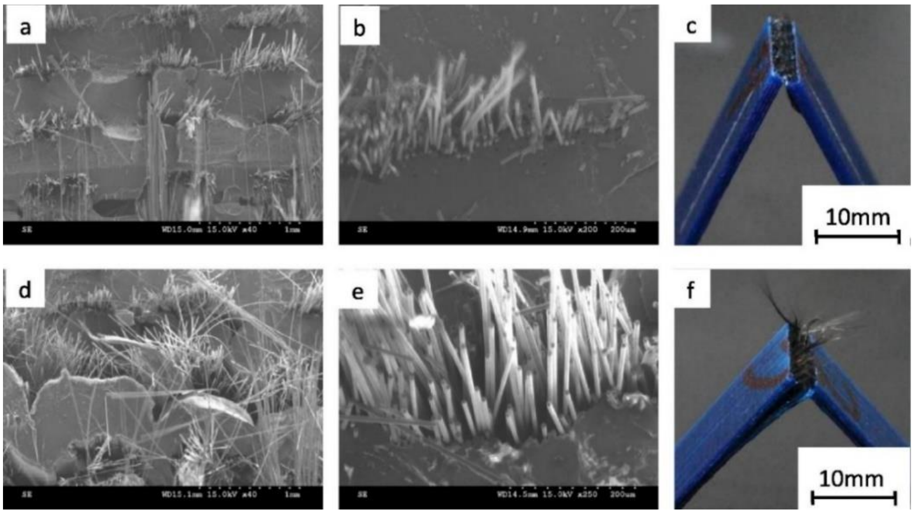

Fig. 26. Microstructures of the obtained fractured cross-section from the applied flexural test on the carbon fiber PLA composites with a layer thickness of 0.5 mm (a, b, c) and 0.7 mm (d, e, f), respectively: (a) and (d) overall cross-section, (b) and (e) interface, (c) and (f) fracture pattern [48]

The hatch spacing was studied from 0.4 mm to 1.8 mm. It was understood that as the hatch spacing was decreased from 1.8 mm to 0.4 mm, the average flexural strength and modulus were improved, simultaneously, from 130 MPa to 335 MPa and 6.26 GPa to 30 GPa, respectively (Fig. 27).

As microscopic observations, by decreasing the hatch spacing from 1.6 mm to 0.6 mm, the impregnation of the matrix into the carbon fiber bundle was improved, according to Fig. 28.

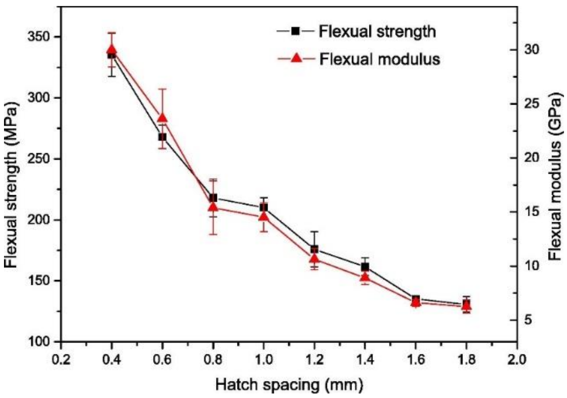

Fig. 27. Influence of hatch spacing on the flexural strength and modulus of the 3D printed carbon fiber PLA composites [48]

The feed rate of the filament (E) and the printing speed was studied, too. The feed rate of the filament affected the pressure and extrusion speed of molten material in the printing head and nozzle. According to Fig. 29, by increasing the feed rate from 60 mm/min to 80 mm/min, the flexural strength of the PLA composite was increased. But the flexural strength of the composite wasn’t improved anymore, by furthermore increasing the feed rate. The reason for this phenomenon could be the short impregnation period. The printing speed was found as an insignificant impact on the flexural strength, according to Fig. 29. As its reason, it was stated that the two contradictory factors which were the impregnation period, then pressure, and overall fiber contents, were influenced the flexural strength versus the printing speed.

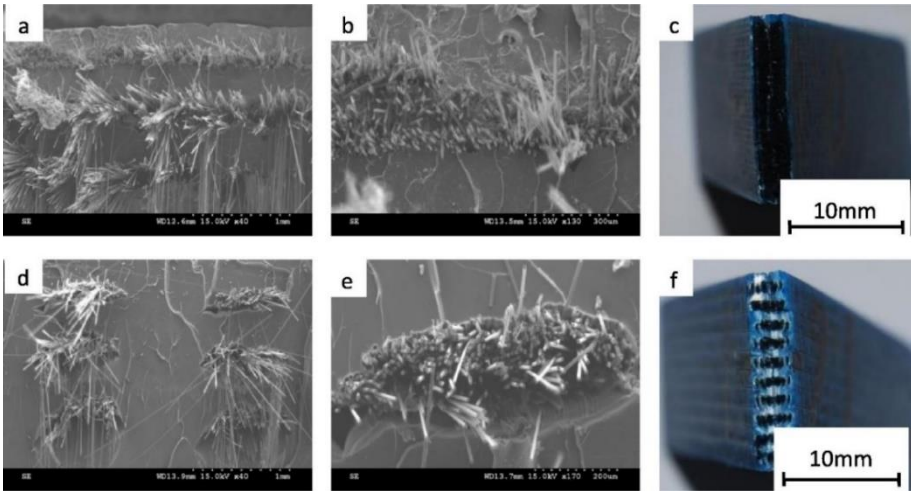

Fig. 28. Microstructures of the obtained fractured cross-section from the applied flexural test on the carbon fiber reinforced PLA composites with hatch spacing of 0.6 mm (a, b, c) and 1.6 mm (d, e, f), respectively: (a) and (d) overall cross-section, (b) and (e) interface, (c) and (f) fracture pattern [48]

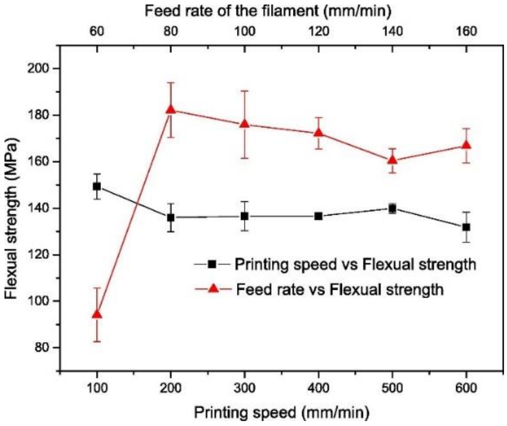

Fig. 29. Influence of feed rate of the filament and printing speed on the flexural strength of the 3D printed carbon fiber PLA composites [48]

Frank van der Klift et al. [51], studied the printed carbon fiber reinforced thermoplastic (CFRT) composite, fabricated by Mark One® printer. Three kinds of tensile test specimens were printed according to Fig. 30, with the same thickness and the quantity of the layers (10 layers). In fact, the first kind of the printed specimens were made of 100% Nylon (10 layers). The second type of the prepared samples (6CF) consisted of two layers of Nylon, six middle layers of carbon fiber reinforced thermoplastic, and two layers of Nylon, again. The third kind of printed specimens (2CF) was composed of four layers of Nylon, then two middle carbon fiber reinforced thermoplastic composite, and the four layers of Nylon.

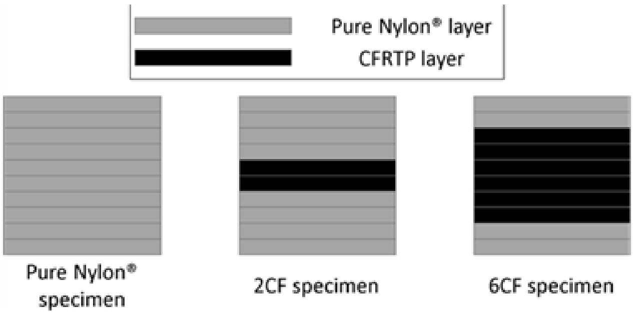

Fig. 30. Schematic drawing of the three types of samples created by the Mark One®. From left to right: 100% Nylon® specimen, 2CF specimen, 6CF specimen [51]

The 6CF specimens showed more tensile strength in comparison with other stated specimens. The tensile strength of the 2CF specimens was about one-third of the prepared 6CF. The cross-section of the 2CF and 6CF specimens were exposed to micro-observation, according to Fig. 31. The observed void areas in 6CF were more in comparison with 2CF specimens. In addition, it has been reported that the 2CF specimens were close to the rule of mixing for the composite specimens that were made by the conventional methods, against the

6CF specimens were not close. The existence of more void areas in 6CF has been stated as the reason for this matter.

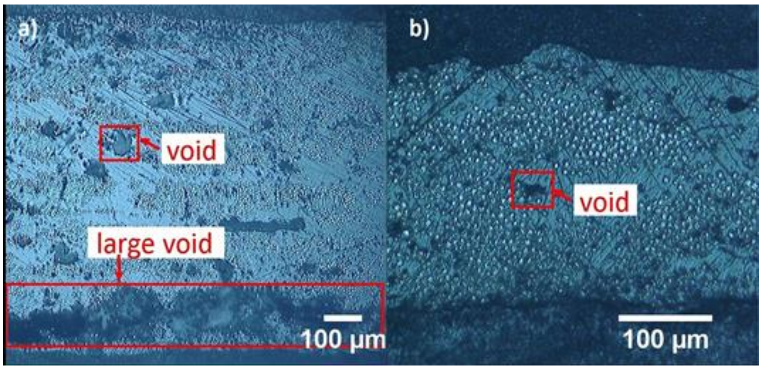

Fig. 31. Cross-sections of the carbon fiber (2 and 6 layers) reinforced Nylon specimens. (a): It shows a cross-section of the 6CF specimen. (b): It shows the cross-section of a 2CF specimen. As can be seen, there is a lot more void area visible in (a) than in (b) [51]

Kuldeep Agarwal et al. [52], studied on comparison of composite filament fabrication (CFF) which was Nylon-fiberglass reinforced polymer, and conventional composite processes, which was Epoxy-fiberglass, made by wet lay-up and vacuum bagging. System 1000 Epoxy resin with stated viscosity of 850 cps at 77°F and Saertex 955 g/m2 stitched unidirectional fiberglass have been utilized for matrix and reinforcement, respectively. The process parameters’ effect on the mechanical properties of the printed composite were studied. The tensile test and fatigue test were conducted to evaluate the mechanical properties. The dimensions of the tested specimens were 250 mm long, 25 mm wide, and 2.5mm thick. The standards of ASTM D3039 and ASTM D3479,28 have been utilized for tensile and fatigue tests, respectively. The tension-tension fatigue test at the frequency of 5Hz was applied. The applied parameters have been related to fiber volume fraction and fiber-layering technique. In the concentric infill pattern related to reinforcements, fiber rings were printed around the perimeter of the specimen, from the outer to the inner section of the specimen. In addition, in the isotropic infill pattern, fiber reinforcement is printed linearly and unidirectionally in a considered direction in a horizontal plane.

According to the mean stress-strain curves, related to the tensile test, (Fig. 32), the prepared specimens with a higher volume fraction of fiber, showed higher strength. The printed composite was stronger than the prepared composite by wet lay-up and vacuum bagging. The isotropic fill related to 0° orientation had a higher strength. Also, the 45° and 90° orientation had lower strength, in comparison with the 0° ones. In the comparison to the used conventional method, it was reported that the manufactured specimens by wet lay-up had about 30-40%

lower strength in comparison with manufactured specimens by vacuum bagging. Also, the better adhesion between the layers, which probably caused the delamination between the layers of the prepared composite, by wet lay-up, was the main failure mechanism.

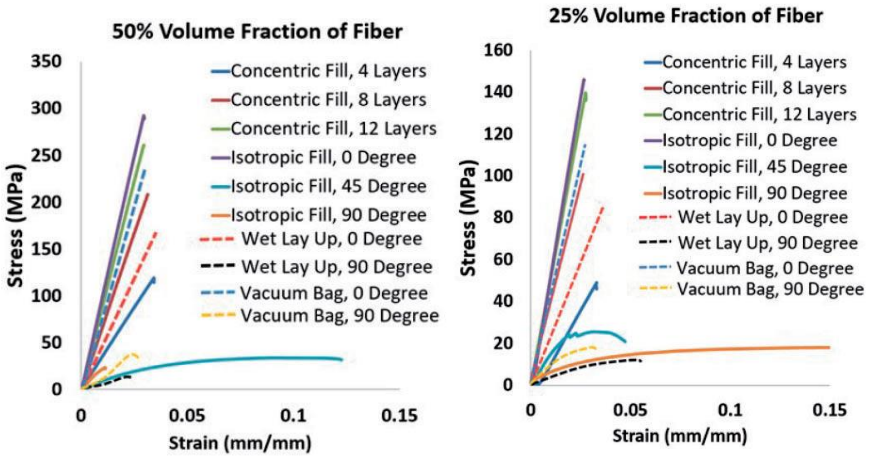

Fig. 32. Stress-strain curves after tensile test of 3D printed Nylon-fiberglass composites, compared with Epoxy-fiberglass composites manufactured by conventional composite processes for range of fiber orientations [52]

According to figures 33 and 34, the prepared 50% volume fraction composites had better fatigue performance in comparison with the prepared 25% volume fraction, according to the tension-tension fatigue results at the frequency of 5Hz. The printed isotropic longitudinal composite (0°) showed the highest fatigue property followed by the printed concentric, 12-layers specimens. Also, the vacuum bagging, as a conventional process, resulted in parts that had a fatigue performance just near to the concentric composite, also about 70-80% of the printed isotropic composite.

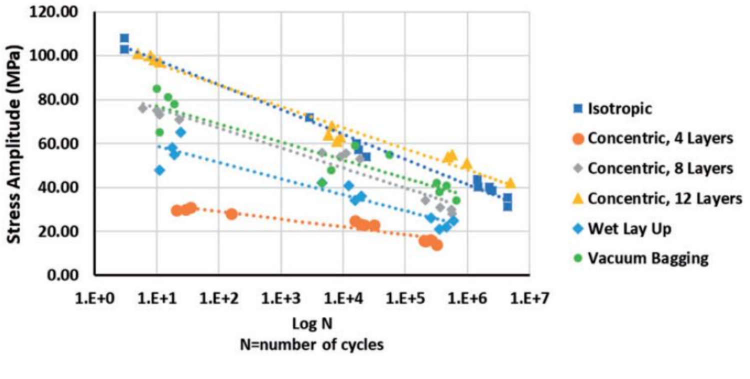

Fig. 33. Fatigue lifetime for 25% volume fraction related to 3D printed Nylon-fiberglass composites, compared with Epoxy-fiberglass composites manufactured by conventional composite processes, 0° orientation [52]

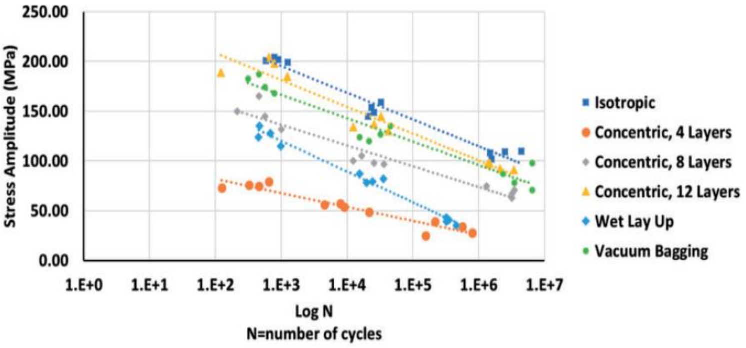

Fig. 34. Fatigue lifetime for 50% volume fraction, 0° orientation [52]

Oztan et al. [53], studied the microstructures related to the various three-dimensional-printed continuous fiber composites and their connection to the mechanical test results, which the tensile test was considered. The printed prepared samples were unidirectional carbon fibers in nylon matrix, unidirectional Kevlar fibers in nylon matrix, and Kevlar fibers in nylon matrix in the directions of ±45°. Also, the unreinforced nylon specimens with 100% infill density were printed by Mark One printer. The PLA specimens were printed in 100% infill density condition, by Ultimaker2 printer (Fig. 35).

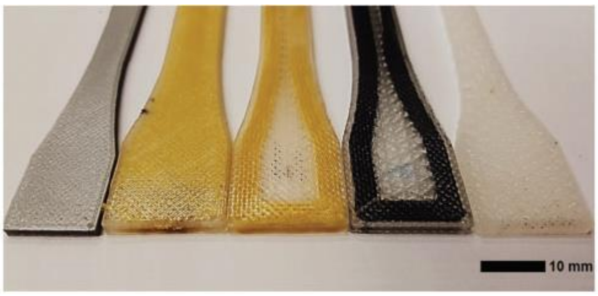

Fig. 35. 3D-printed samples were used in the research. Left to right: PLA sample produced using Ultimaker 2 printer, ±45° Kevlar fiber, unidirectional Kevlar fiber, unidirectional carbon fiber, and unreinforced nylon matrix [53]

The comparison between the manufactured polymer specimens by 3D printing and traditional methods (in which the PLA and nylon filament samples from the supply coil of the printer were used), was made, too. The related tensile test results of the unidirectional and the printed PLA and nylon were according to Fig. 36. According to the tensile test results, the tensile strengths of the printed polymers were lower than those, which were traditionally fabricated. This distance between the tensile strengths, were more obvious, in the case of the nylon samples. In fact, the related ultimate strength of the printed nylon was reported as half of the nylon's samples, which were traditionally fabricated. Also, the start of the stiffness loss has happened in the printed specimens, firstly in comparison with the traditionally fabricated ones. It was reported that the maximum tensile strain values were independent of the manufacturing methods, against the ultimate stress.

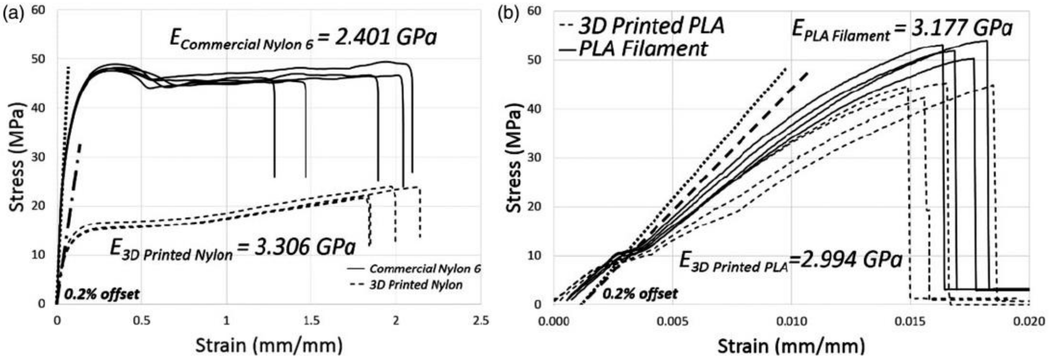

Fig. 36. Stress-strain curves of the 3D-printed and traditionally fabricated polymers. (a) Nylon specimens and (b) PLA specimens [53]

Then, the microscopic observations were applied according to Fig. 37. Fig. 37(a) is related to the cross-hatched pattern. The imperfect fusion of the layers (between the layers) is visible clearly. Also, a common defect of the printed material, which is the rectangular gap, was observed in Fig. 37(b). Fig. 37(c) is related to the insufficient material inter-diffusion between the printed lines, which causes the surface roughness on the upper print face. Fig. 37(d) is reported as the related SEM photo to the observed porosities in PLA samples, which caused the mechanical properties reduction.

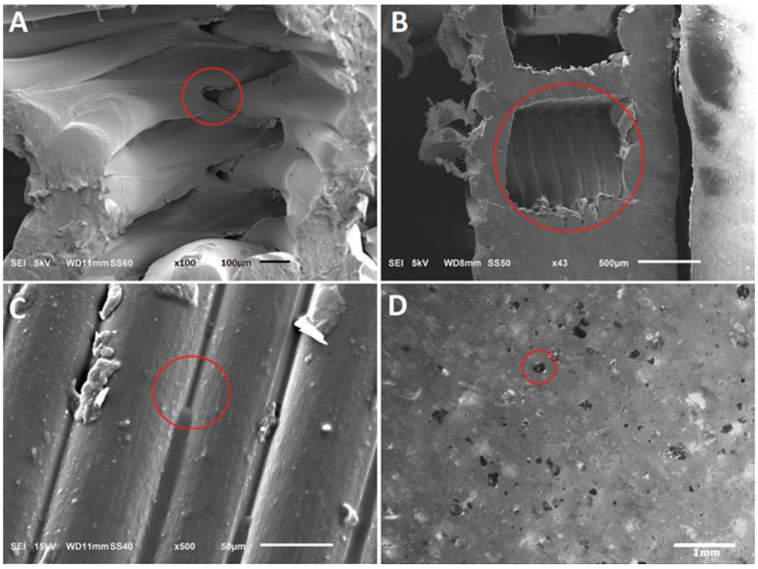

Fig. 37. Microstructural defects in 3D-printed, unreinforced polymer specimens. (a) Crosshatch voids in nylon sample, (b) fiber tow gaps in nylon sample, (c) surface roughness in nylon sample, and (d) micropores at the surface of PLA sample [53]

Therefore, according to the tensile test results of the printed reinforced composites (Fig. 38), it was reported that all tensile tested specimens had a linear-elastic behavior. The comparison between the matrix and the fiber types, also their related orientation, is clear according to Fig. 38. The printed carbon fiber reinforced composites had the highest tensile strength and the lowest failure strain, in comparison with the Kevlar fiber-reinforced composites. The fabricated Kevlar-reinforced composites, in the orientation of ±45°, had lower tensile strength in comparison with the unidirectional ones. It was reported that the strength of the unreinforced nylon samples was increased by a factor of 2-11, depending on the specimen direction.

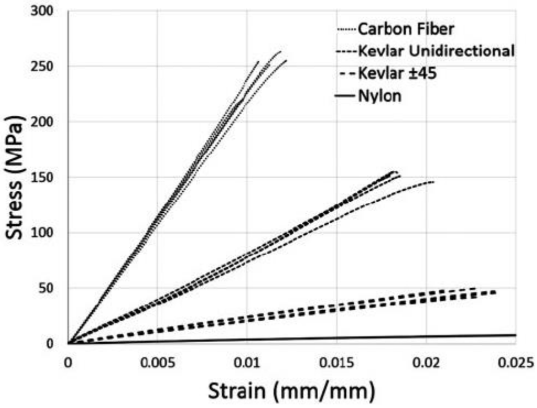

Fig. 38. Stress-strain curves of the 3D-printed composites (unidirectional carbon fibers in nylon matrix, unidirectional Kevlar fibers in nylon matrix, ±45°-oriented Kevlar fibers in nylon matrix, also the unreinforced nylon specimens with 100% fill density, according to Fig. 34) [53].

According to the related micro-observation (Fig. 39), the rupture of the carbon fibers was brittle; also there was no distortion or elongation of the broken ends. However, the fracture of the Kevlar fibers was ductile and the related elongation and distortion in the failure section were reported.

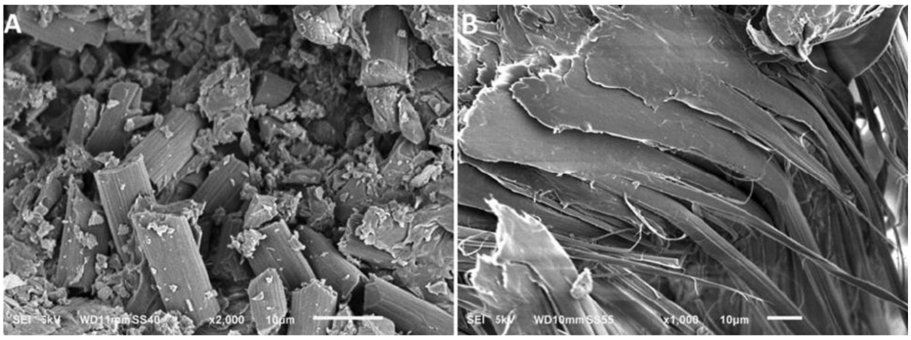

Fig. 39. SEM images of fractured fibers, (a) carbon fibers showing brittle damage morphology, and (b) Kevlar fibers showing significant elongation and distortion, after tensile tests [53]

Dong et al. [54], studied on the continuous Kevlar fiber reinforced nylon thermoplastic, manufactured by Mark One printer as FFF process. Four parameters were considered to study to understand the mechanical properties development, by use of the continuous Kevlar fibers as reinforcement into 3D printer reinforced nylon composites. These four parameters were as below:

1. Effect of fiber orientation
2. Effect of the layer position
3. Effect of volume fraction
4. Effect of the infill orientation

In addition, the details of the samples were as Table 7.

Sample No.	Total Layers	Layers of fibers	Direction of fibers	Position of fiber layers
1	20	10	0	6-15
2	20	10	90	6-15
3	20	10	0	2-6, 15-19
4	20	10	90	2-6, 15-19
5	20	0	-	-
6	20	18	0	-
7	20	18	90	-
8	20	10	0°-5, 90°-5	6-15
9	20	10	45°-5, -45°-5	6-15
10	Same as No.1 but with 0°- and 90°-degree Nylon			

Table 7. The design parameters of continuous Kevlar fiber reinforced composites (KFRCs) [54].

As the effect of the fiber orientation, samples 8 and 9 were studied. Sample 8 was consisting of 5 layers of 0°-Kevlar fibers and 5 layers of 90°-Kevlar fibers. Also, sample 9 was consisting of 5 layers of 45^o fibers and -45° fibers. It was stated that the continuous Kevlar fiber showed high elastic modulus in the longitudinal direction. The Young's modulus and tensile strength of the continuous KFRs in this research were higher than the printed short fiber-reinforced composites, reported by [55]. As the effect of the layer position, it was concluded that the fiber position does not have influence the related tensile modulus of the fabricated continuous KFRCs, by FFF. Also, it was understood that the related tensile stress of sample 3 was lower than sample 1, at the break.

As the effect of volume fraction, it was stated that the higher volume fraction of the used Kevlar fibers, could improve related tensile stress and elastic modulus to the break. But the condition of the fiber and nylon matrix may be causing the lower ultimate strength and elastic modulus of the continuous Kevlar fiber-reinforced composites than the predicted value from the rule of mixtures. As the effect of the infill orientation, the related infill angles of Nylon in the printed composite samples were ±45° by default, except sample 10. In fact, sample 10 was printed with 0° and 90° infill angles. The fiber direction in samples 1 and 10 was parallel to the tensile direction. It was stated that the effect of the infill angle of Nylon could be neglected, because it was much lower than the Kevlar fiber, according to the related stress-strain curves of sample 1 and 10. Also, this effect was studied by samples 8 and 9, too. The related stress-strain curves are as Fig. 40.

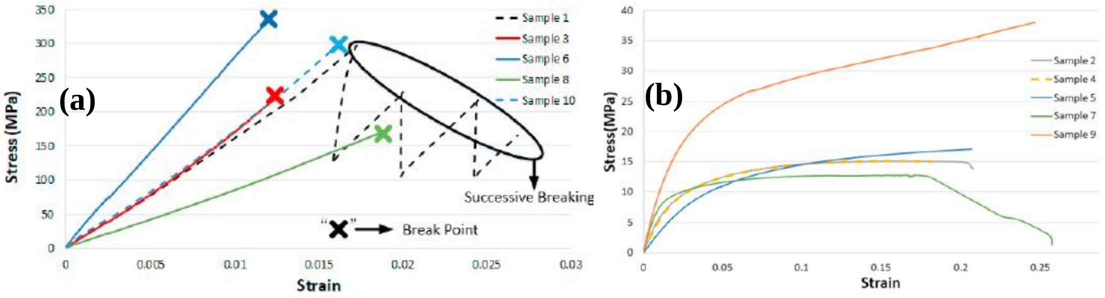

Fig. 40. Stress-strain curve and breaking points of 3D printed Kevlar fiber reinforced PLA composite with layups shown in Table 7 (a) samples 1, 3, 6, 8, 10 and (b) 2, 4, 5, 7, and 9 [54]

The failure mode of the tested samples was debonded on the Kevlar fibers orientation. In the case of the unidirectional specimens, in which the Kevlar fiber was in the same direction of the applied stress, the breakage of the unidirectional fibers was reported as the reason for the failure (Fig. 41(c)). Also, in the case of the 90° fibers (perpendicular to the applied tension stress), the failure between two fiber filaments was reported (Fig. 41(a) and (b)). In case of the failure, related to ±45° specimens, it was stated that the fibers did not break during the tensile test. The debonding between the Kevlar and nylon layers was stated as the reason for the ±45° printed specimens. Generally, the difference between the Poisson's ratio of nylon and fiber layers was stated as the reason for the fiber-nylon layers debonding.

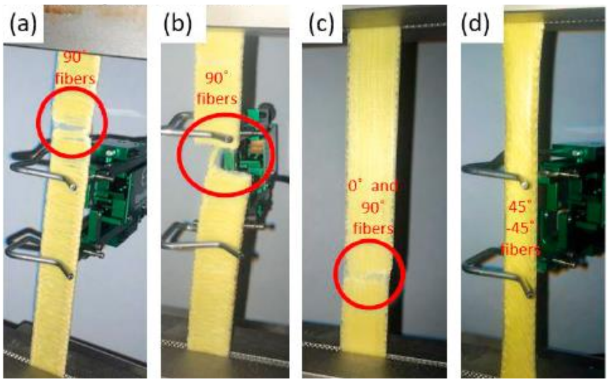

Fig. 41. (a) failure of sample 4, (b) failure of sample 7, (c) failure of sample 8, and (d) shear deformation of fibers in sample 9 [54]

Nekoda van de Werken et al. [56] investigated the mechanical properties of the manufactured continuous carbon fiber reinforced Nylon by 3D printing. The specimens were printed utilizing a Markforged commercial printer (Fig. 42).

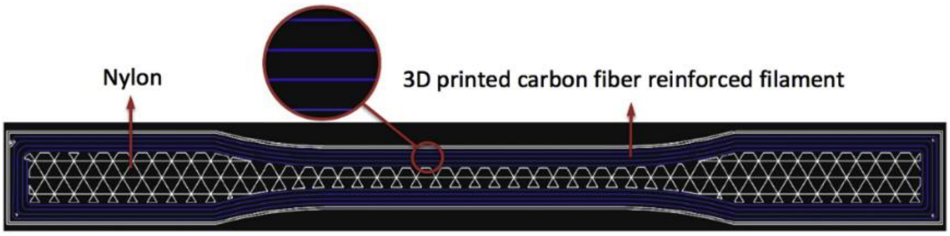

Fig. 42. The related 2D internal layer structure of a manufactured continuous carbon fiber reinforced Nylon by 3D printing [56]

The microstructure of the 3D printed continuous carbon fiber reinforced Nylon samples were characterized. The printed specimens were cut for cross-sectional microscopic observations. The microscopic observations showed that a huge number of voids were existed in the manufactured specimens by FFF. The existence of the voids was introduced as the reason for the failure of the samples at the lower stresses in comparison with the theoretically predicted stresses (Fig. 43).

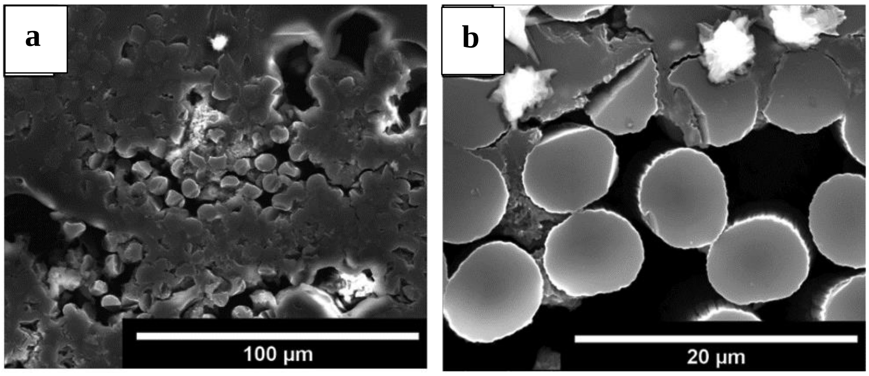

Fig. 43. The cross-sectional microstructure of the 3D printed carbon fiber reinforced Nylon specimens a) the existence of the voids in the 3D printed composite, b) the carbon fibers as for the reinforcement in the 3D printed carbon fiber reinforced Nylon composite [56]

According to the tensile tested specimens, the various failure modes such as delamination, inter-filament failure, and fiber failure were observed, like the prepared composite parts by conventional methods. According to the fiber pullout phenomenon observations, the weakness of the related interfacial strength between the matrix and reinforcement was shown (Fig. 44).

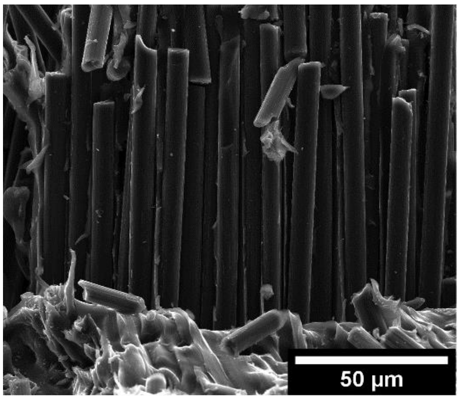

Fig 44. The fiber pullout phenomenon in the 3D printed carbon fiber reinforced Nylon composite [56]

It was stated that the approached strength of the manufactured specimens by 3D printing strictly depends on the part geometry and infill pattern. In fact, the interfaces between the non-reinforced and reinforced sections and regions and the fiber curvatures caused the multi-axial stress states, stress concentrations, and pre-mature failure in the printed parts.

Ali N. Sarvestani et al. [57] studied the effects of volume fraction and fiber orientation on mechanical properties of the manufactured carbon fiber reinforced polymer composites (CFRP) by FFF. Post fracture microscopy observations (Fig. 45) exhibited the fiber pullout phenomenon. The fiber pullout demonstrated that the interfacial strength between the fiber and polymer matrix was relatively low.

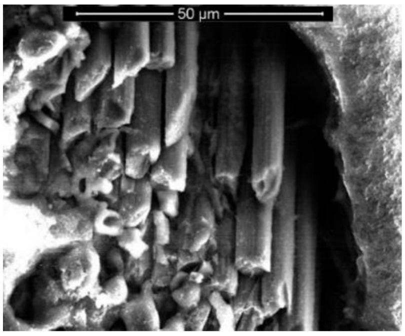

Fig 45. Post fracture microscopy observation 3D printed carbon fiber reinforced Nylon composite samples showing fiber pullout [57]

Different tensile test sample geometries related to carbon fiber reinforced Nylon composite, which caused different fiber volume fractions in the gauge section, were taken into account. The stated samples were printed by consideration of the different configurations for fiber orientation. Any of the samples weren’t broken in the gauge section and none of the samples failed just because of the fiber failure phenomenon. Other modes of damages such as fiber pull, matrix cracking, and delamination were reported (Table 8).

Sample Description	Fiber volume fraction in the gauge section	Modulus of Elasticity (GPa)	Failure Strength (MPa)	Prevalent Damage Mode (failure region)
ASTM D638-14 Type 1 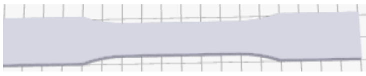	5	7.2	94.7	Matrix failure (grip region)
	12	17.5	258.1	Matrix failure (grip region)
	14	21.3	265.8	Matrix failure (grip region)
	28	55.7	270.4	Delamination (grip region)
ASTM D638-14 Type 4 	24	46.1	171.9	Matrix failure (grip region)
ASTM D3039/D3039M – 14 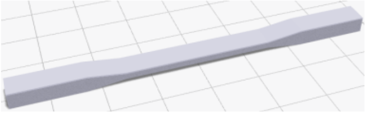	30	52.4	580.0	Fiber Failure + Delamination (gauge region)

Table 8. Tensile test results and prevalent damage modes of the 3D printed carbon fiber reinforced Nylon composite samples, by Mark Two, Markforged [57]

Yolnan Chen et al. [58] studied the effect of the orientation of the used continuous reinforcement on the tensile strength of the manufactured part by FFF. The considered orientations were “concentric” and “isotropic” infill. According to concentric layout, the reinforcement rings printed along the boundary walls of the part, but according to the isotropic fill the reinforcement located at the desired orientation in the one complete layer (Fig. 46).

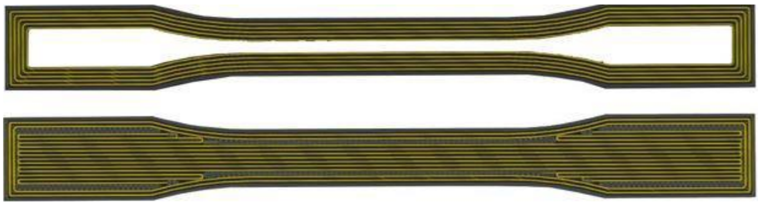

Fig 46. Cross-section view of concentric (top) and isotropic (bottom) infills [58]

PLA, ABS, nylon as for polymers, also Carbon fiber, glass fiber, and Kevlar fiber were used as reinforcements. In the case of composite fabrication, the nylon used as matrix and the stated fiber reinforcement materials were applied by Markforged printer.

Firstly, the carbon fibers were used for reinforcing the all below stated geometries and infills via FFF method (table 9). Then the best fiber orientations, which showed the highest yield stress were selected, and tested with Kevlar fibers and glass fibers.

Polymer Material	Fiber Material	Fiber Fill Type	Rings	Infill Type	Infill %	Machine
Nylon	None	None	0	Rectangular	75	Markforged
Nylon	Carbon	Concentric	2	Rectangular	75	Markforged
Nylon	Carbon	Concentric	4	Rectangular	75	Markforged
Nylon	Carbon	Concentric	5	Rectangular	75	Markforged
Nylon	Carbon	Isotropic	0	Rectangular	75	Markforged
Nylon	Carbon	Isotropic	2	Rectangular	75	Markforged
Nylon	Carbon	Isotropic	4	Rectangular	75	Markforged
Nylon	Carbon	Isotropic	5	Rectangular	75	Markforged

Table 9. Table of the printed tensile specimens [58]

As for concentric infill type, Fig. 47 exhibits the related stress-strain graph of the concentric infill reinforced nylon. The strongest specimen was reinforced by five concentric fiber rings (the highest-fiber volumetric fraction), which had a fracture stress level of 250 MPa. In addition, the reinforced specimens by two concentric fiber rings were the weakest ones.

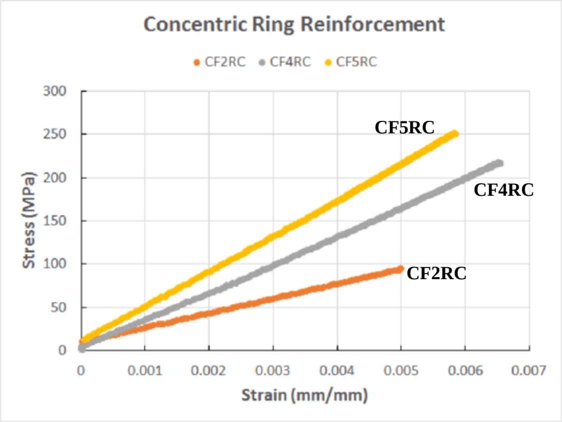

Fig 47. Stress-strain of the printed specimens with CF with concentric fiber rings. The selected concentric rings of Carbon Fiber were 2, 4, and 5 [58]

Fig. 48 is related to tensile test results of isotropic infill reinforced nylon. According to the below-obtained results, the reinforced specimens by isotropic infill with two concentric rings of the reinforcement exhibited the highest strength. The volumetric fraction of the reinforcement was reported as almost constant for all of the printed specimens.

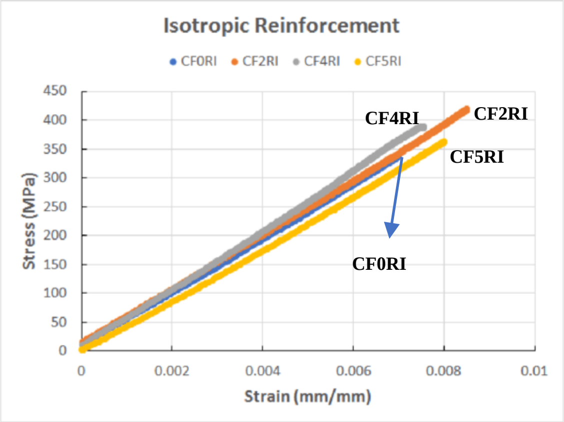

Fig 48. Stress-strain of the printed specimens with CF with isotropic infill of the carbon fiber. The selected Carbon Fiber infill were 0, 2, 4, and 5 rings isotropic infill [58]

The two aforementioned strongest fiber orientations were considered, and the specimens were printed with KV and FG, too. The reinforced specimens with CF showed the highest yield strength, while the obtained deformation resistance to fracture was lower in comparison with the reinforced sample by FG and KV. The comparison between the different types of reinforcement materials is prepared in Fig. 49.

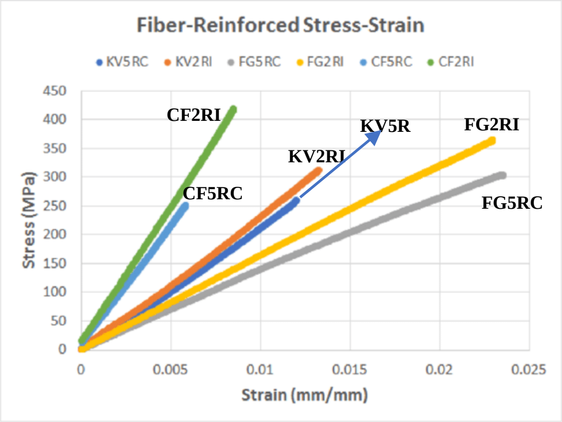

Fig 49. Tensile Stress-strain curves related to tensile specimens using the two best-obtained fiber orientations [58]

Astrit Imeri et al. [59], studied the effect of infill type and the fiber pattern on tension-tension fatigue characteristics under load ratio of 0.1 of 3D printed polymer composite. Nylon was selected as the matrix of the composite and the specimens were produced by Markforged Mark Two 3D Printer. The specimens were printed under “concentric” and “isotropic” infill patterns. The stated the existence of a correlation between the type of the used filler material and the selected infill pattern of the reinforcement printing. In fact, the carbon fiber exhibited a better fatigue resistance in comparison with other used reinforcements (glass fiber and Kevlar fiber). In the case of printing with the concentric pattern, the increase of the rings increased the fatigue life. As for the isotropic infill pattern, the fatigue behavior decreased by increasing the number of reinforcement rings.

Table 10 presents the summary of extracted mechanical data for continuous fiber systems loaded parallel to the printing direction. One can note from this table the effect of fiber percentage on the tensile strength and tensile modulus. By increasing the reinforcement volume fraction the tensile properties were increased. Moreover, the reinforcement type has a significant effect on the mechanical properties.

References	Materials	Tensile strength (MPa)	Tensile modulus (GPa)
Dickson et al. [60]	Nylon/CF 11vol.%	198	8.46
	Nylon/AF 8vol.%	110	4.23
	Nylon/GF 8vol.%	156	3.29
	Nylon/AF 10vol.%	161	4.76
	Nylon/GF 10vol.%	212	4.91
Van der Klift et al. [51]	Nylon/CF 6vol.%	140	14

	Nylon/CF 18vol.%	464.4	35.7
Yang et al. [61]	ABS/CF 10wt.%	147	4.19
Tian et al. [62]	PLA/CF 10wt.%	256	20.6
Li et al. [47]	PLA/CF 34vol.%	91	23.8
Melenka et al. [63]	Nylon/AF 4vol.%	31	1.77
	Nylon/AF 8vol.%	60	6.92
	Nylon/AF 10vol.%	84	9
Matsuzaki et al. [45]	PLA/CF 6.6vol%	185.2	19.5
	PLA/Jute fiber 6.1vol%	57.1	5.11
Bettini et al. [64]	PLA/AF 8.6 vol. %	203	9.34

Table 10. Summary of extracted mechanical data for continuous fiber (AF: Aramid Fibers, GF: Glass Fibers, and CF: Carbon Fibers) systems loaded parallel to the printing direction

2.3.2.2 Short fiber-reinforced

Weihong Zhong et al. [65], studied the fabrication of the reinforced ABS by short glass fibers as feedstock filament in the FFF process. As improving the properties of the ABS, short glass fiber as reinforcement was used. The strength of the short glass fiber reinforced ABS was increased, in comparison with the pure ABS. By use of the glass fiber reinforcement, the surface rigidity was developed, and the shrinkage was decreased. However, the handleability was decreased. In fact, the prepared composite feedstock wasn’t possible to be made into a continuous wound on a conventional cylindrical shape drum, and this brittleness caused the impossibility of the use of the prepared composite feedstock in the FFF machine. By use of a small amount of compatibilizer and plasticizer, these properties of the prepared composite feedstock were improved.

Fuda Ning et al. [55], studied on fabrication and properties of the reinforced ABS by short carbon fiber feedstock. The effect of the carbon fiber content and length were studied on the mechanical properties of the fabricated samples. The used carbon fiber powders had two average lengths of 100 μm and 150 μm. The pellets of polymer (matrix) and carbon fiber powders (reinforcement) with different contents of 3 Wt%, 5 Wt%, 7.5 Wt%, 10 Wt%, and 15 Wt% were blended, then were extruded for manufacturing the feedstock filament for the FFF process, according to Fig. 50.

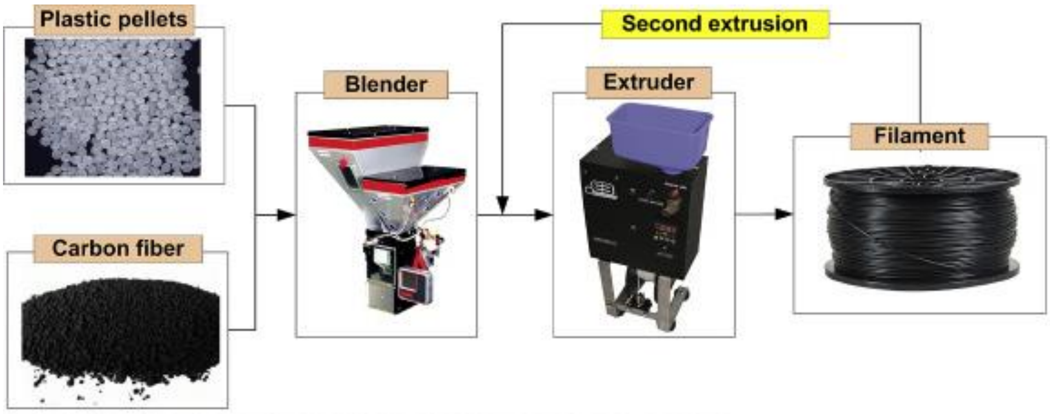

Fig. 50. Manufacturing the feedstock filament for the FFF process [55]

As the effect of the carbon fiber content on the tensile properties was surveyed (Fig. 51). As its effect on tensile strength, it was observed that with an increase of the used short carbon fiber content from 0 Wt.t% to 5 Wt.%, tensile strength was increased, too. Then, with an increase of the carbon fiber content from 5 Wt.% to 10 Wt.% the tensile strength decreased. But the strength was increased with the increase of the carbon fiber content from 10 Wt.% to 15 Wt.%. As the effect of the carbon fiber content on the young's modulus, the increase of the young's modulus was observed by the increase of the reinforcement content from 0 Wt.% to 7.5 Wt.%. But the sudden decrease of the young's modulus was observed by the increase of the carbon fiber from 7.5 Wt.% to 10 Wt.%. Again, with the increase of the reinforcement content up to 15 Wt.%, the young's modulus was increased. The ductility decreased by increase the content of the carbon fibers from 0 Wt.% to 10 Wt.%. But the ductility increase was reported with the increase of the carbon content from 10 Wt.% to 15 Wt.%. The lowest ductility was related to unreinforced plastic specimens.

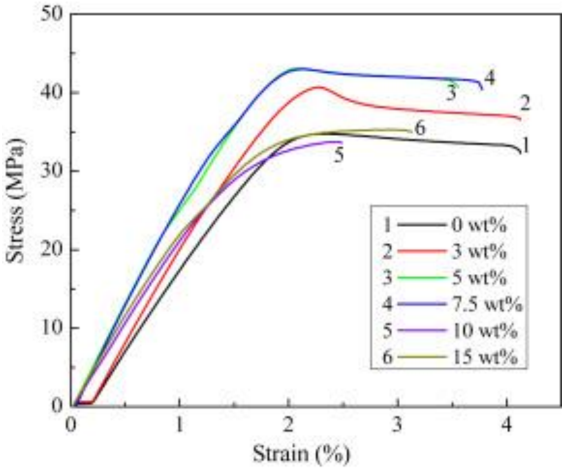

Fig. 51. Typical tensile strain–stress curves for specimens with different carbon fiber contents (The carbon fiber length is 150 μm), related to carbon fiber reinforced ABS composite [55]

Also, the effect of the carbon fiber length on the tensile properties of the printed samples was studied (Fig. 52). It was observed that the tensile strength and young's modulus of the printed composite samples with 150 μm carbon fiber, were more than ones were printed using 100 μm carbon fiber. The composite samples with 100 μm carbon fiber, had more toughness and ductility in comparison with ones 150 μm as carbon fiber length. As microscopy observation, it was observed that in the specimens with 10 Wt.% carbon fiber content, the porosity was severest. This phenomenon was stated as the probable reason for the smallest values of the tensile strength, toughness, yield strength and ductility, in the printed samples by the use of the 10 Wt.% carbon fiber as the reinforcement.

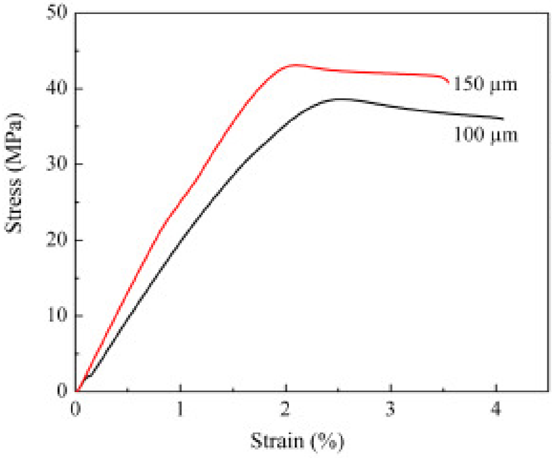

Fig. 52. Effects of carbon fiber length (Carbon fiber content is 5 Wt.%), related to carbon fiber reinforced ABS composite [55]

Tenkinalp et al. [66], studied the effects of the two important parameters which were porosity and fiber orientation on the mechanical properties of the printed reinforced ABS, by short carbon fiber (0.2-0.4 mm). The related results of the printed samples also were compared with the prepared composite parts, by compression molding (CM). The printed samples had void formation which was due to the inappropriate adhesion and bonding between the polymer matrix and fiber reinforcement, according to the Fig. 53. As a comparison against the printed samples, there was almost no voids in the samples which were prepared by compression molding (CM). The printed samples were very high fiber oriented but the prepared composite parts by CM were less oriented. As the tensile test results, the related results of the printed specimens were almost close to the prepared ones by compression molding (CM). In fact, two main parameters completed and affected strength, which were the orientation of the fibers and existence the negative porosity. In the case of the printed samples, the fibers were in direction of the applied load and could overcome the negative effect of the porosity existence.

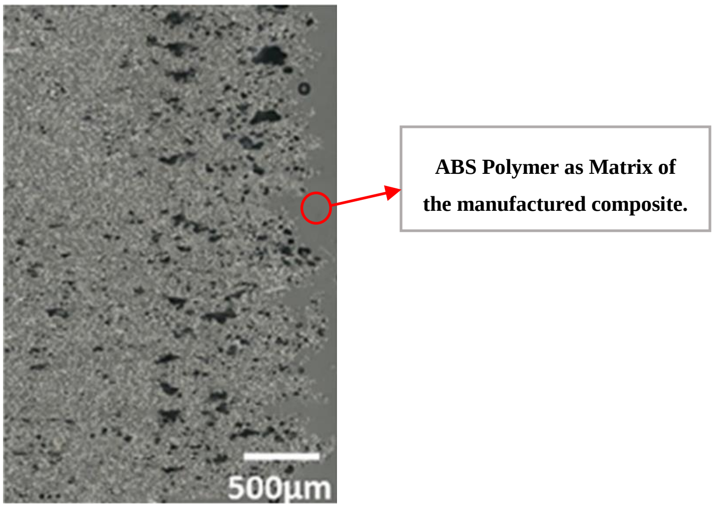

Fig. 53. Micrograph of the polished surface of the printed ABS/30 Wt.% carbon fiber composite [66]

In addition, it was reported that the tensile strength of the printed neat-ABS samples was higher than the neat-ABS prepared by CM. As a result, it was stated that the FFF method increased the molecular orientation of the polymer chains, which increased the tensile strength in the FFF process. Also, as the content of the fiber was increased, the voids between the beads decreased, but the void content inside the bead, increased.

Lonnie J. love et al. [67], studied the reinforced ABS by short carbon fiber composite parts. They showed that the use of carbon fiber (CF) with polymer (matrix) as a feedstock of AM process could increase the stiffness and strength of the final printed parts. They could demonstrate that the use of CF, can decrease the coefficient of thermal expansion (CTE) and increase the thermal conductivity, which greatly caused the reduction of the distortion of the final printed parts. In fact, by the increase of the thermal gradients were reduced through the final printed parts. Also, by reducing the CTE, the strain of the material during the cooling from the deposition temperature to ambient conditions decreased. So, the impacts of these two important factors could reduce the distortion of the parts during additive manufacturing.

Yasa et al. [68], studied the impact toughness of the fabrication parts by FFF. They studied the effects of the infill density and build orientation of the printed chopped carbon fiber reinforced nylon (Onyx) and the printed unreinforced one, on the impact toughness property. The three different build orientations of A, B, and C according to Fig. 54(a), were considered. The samples were printed according to ISO 179 Plastics Determination of Charpy Impact Properties. The dimension of the prepared specimens was according to Fig. 54 (b). The printed specimens that were unnotched, were tested on a Ceast Impactor equipment located in TUBİTAK MAM at room temperature.

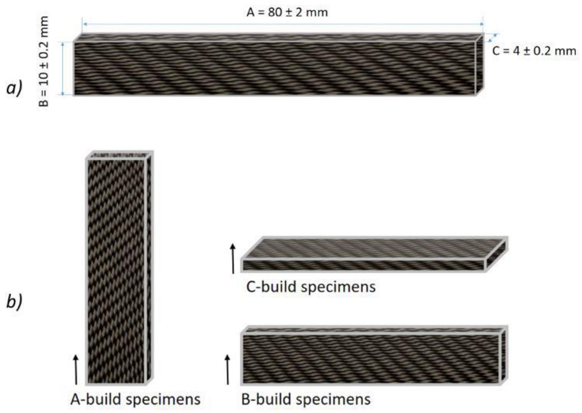

Fig. 54. (a) The geometry of the printed specimens according to ISO 179, (b) Naming of the specimens built along different axes [68]

The Nylon had better toughness in comparison with Onyx, about 2.5 times better. Also, the specimens, which received an impact in between two layers (A-Build Onyx 100%) had lower toughness (about 10 times) compared to specimens that received an impact, not between deposited layers (C-Build Onyx 100% and B-Build Onyx 100%). As for the effect of the infill density, by changing the infill density to 75%, the toughness decreased about 50%. However, by further infill density reduction by another 25% reduction to reach 50% infill density, the toughness reduced only less than 5% (Fig. 55). Generally, it was concluded that the impact toughness is a severe anisotropic property.

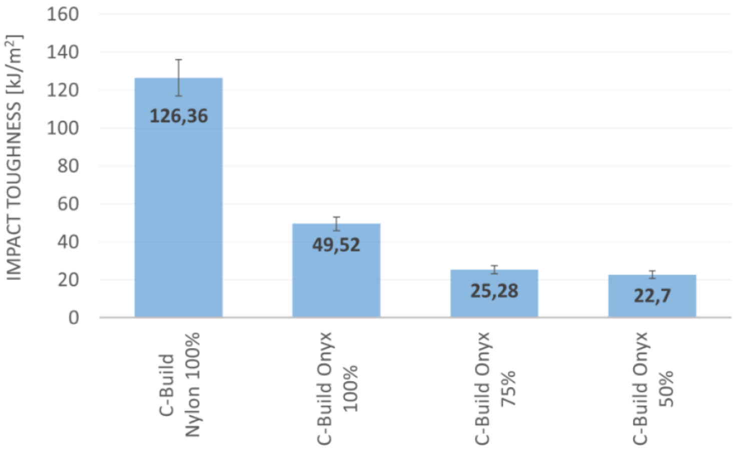

Fig. 55. The Charpy impact toughness results of specimens built with different densities [68]

Carneiro et al. [69], studied on FFF process of polypropylene (PP). As a part of their research, they compared the tensile properties of PP and glass reinforced PP (GRPP). They indicated that the use of glass fibers as reinforcement was effective in the FFF process. It was reported that the modulus and strength of PP were increased about 30% and 40%, respectively, by the use of glass fibers as reinforcements.

The flow of reinforcements is an important aspect of the FFF process of composites. The flow of an 8vol. % carbon fiber reinforced epoxy through the tip of a nozzle was modeled by Lewicki et al. [70]. They considered the carbon fibers as discrete particles in the simulations. Therefore, fiber-fiber interactions and fiber-wall interactions were taken into account. The fibers were considered as separate domains and particle-particle interactions were implemented with frictional, inelastic contact forces. Moreover, fluid dynamics equations have been used. Fig. 56 demonstrates the orientation evolution of an initially randomly oriented arrangement of fibers.

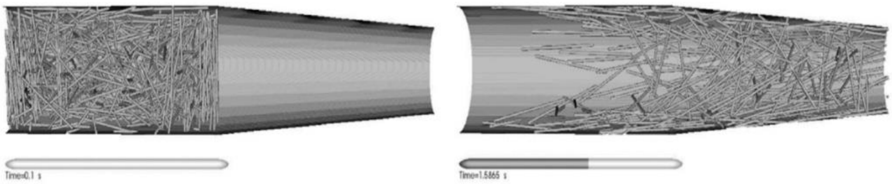

Fig. 56. Fiber orientation evolution with time at a constant pressure [70]

Ankit Gupta et al. [71], studied the mechanical properties of the FFF manufactured polycarbonate reinforced with short carbon fiber (SCF) composite. The specimens were printed with different volume fractions of short carbon fibers (3%, 5%, 7.5%, 10%) and different printing speed values of 25, 50, and 75 mm/s. It was found out that the two selected variables, which were volume fractions of short carbon fibers and printing speed, affect the mechanical properties of the printed specimens, greatly.

It is stated that as the volume fraction of the used short carbon fiber reinforcement was increased, the suitable load transferring from polymer matrix to reinforcement was increased, up to 7.5% of reinforcement. Further increase amount (more than 7.5%) of the used short carbon fibers, didn’t increase the tensile strength of the printed specimens anymore (the tensile strength decreased or become stable on a specific value), Fig 57a.

As for the reason of the tensile strength decrease related to the printed specimens with more than 7.5% short carbon fibers (as reinforcement), the local accumulation of reinforcements (Fig. 58b) in the polymer matrix was introduced. It is stated that many locations were remained dry in the polymer matrix which resulted in decreasing the strength of the printed composite. Also, the observed fiber pullout (Fig. 58c) and fiber breakage (Fig. 58d) phenomena were increased more by the increase of short carbon fiber percentage, which caused the creation of more voids and the further decrease of the tensile strength. In addition, the pure polycarbonate exhibited more tensile strength in comparison with reinforced samples (printed composite materials). The lack of perfect alignment of the short carbon fibers as the used reinforcements were stated as the reason for this decreasing in strength.

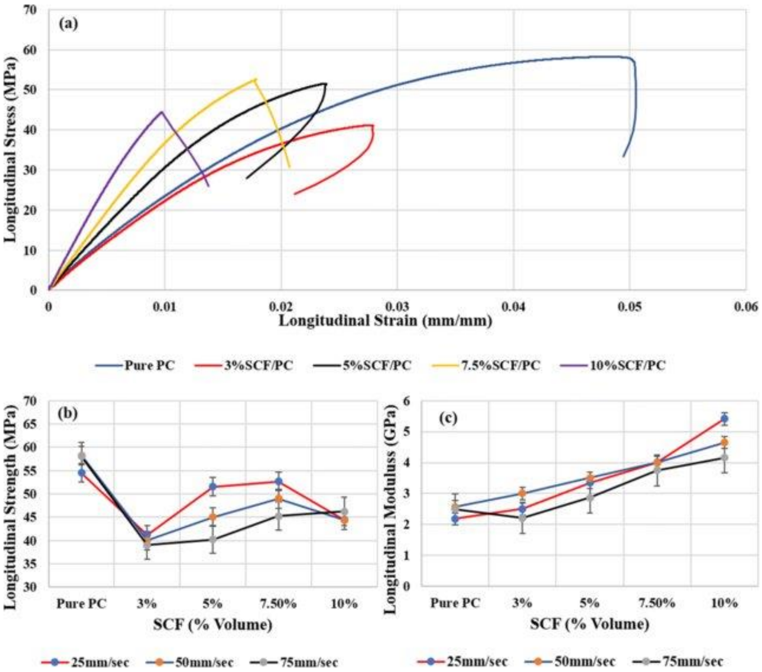

Fig. 57. a) Obtained longitudinal stress-strain curves for the different percentage of short carbon fiber reinforcement. b) Reinforcement percentage effect on longitudinal strength at printing speed of (i) 25mm/s, (ii) 50 mm/s, (iii) 75 mm/s. c) Reinforcement percentage effect on longitudinal modulus at printing speed of (i) 25 mm/s, (ii) 50 mm/s, (iii) 75 mm/s [71]

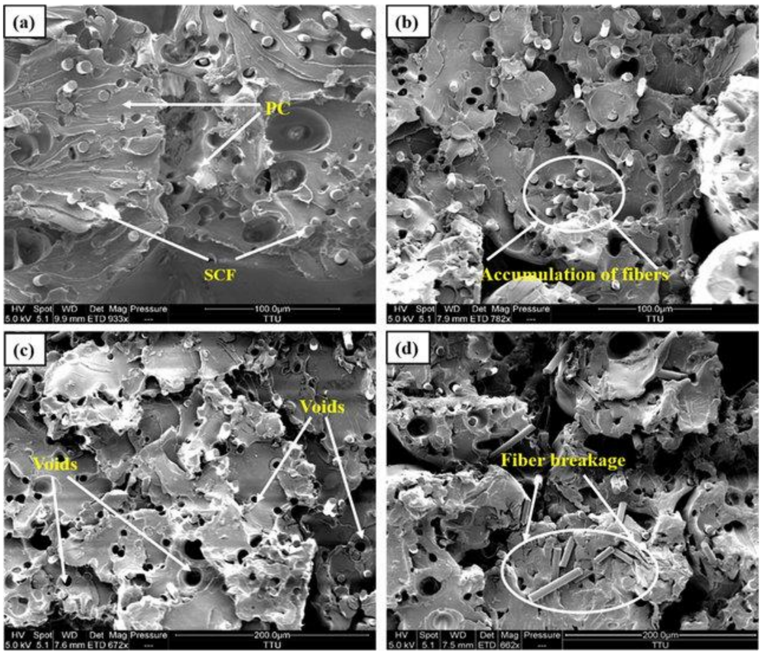

Fig. 58. The obtained SEM images of the printed samples after tensile testing. a) the distribution of fibers and matrix, b) the observed accumulation of the short carbon fibers at one place. c) short carbon fiber pull-out and d) short carbon fiber breakage at a high percentage [71]

Tables 11 and 12 present the summary of extracted mechanical data for discontinuous fiber systems loaded parallel and perpendicular to the printing direction, respectively. In Tables 11 and 12, one can note that the difference in properties along and transverse to print direction due to short fiber alignment. The scattering in properties is due to processing conditions.

References	Materials	Tensile strength (MPa)	Tensile modulus (GPa)
Ninge et al. [55]	ABS/CF 3wt.%	40.8	2.1
	ABS/CF 5wt.%	42	2.45
	ABS/CF 7.5wt.%	41.5	2.5
	ABS/CF 10wt.%	33.8	2.15
	ABS/CF 15wt.%	35	2.25
Tekinalp et al. [66]	ABS/CF 10wt.%	52	7.7
	ABS/CF 20wt.%	60	11.5
	ABS/CF 30wt.%	62	13.8
	ABS/CF 40wt.%	67	13.7
Hill et al. [72]	ABS/CF 20wt.%	66.8	8.4
Kunc [73]	ABS/CF 13vol.%	53	8.15
Love et al. [67]	ABS/CF 13vol.%	70.69	8.91
Duty et al. [74]	ABS/CF 20wt.%	65.7	11.9
	ABS/GF 20wt.%	54.3	5.7
	ABS/GF 40wt.%	51.2	10.8
Duty et al. [75]	ABS/CF 20wt.%	47.7	10.87
	ABS/CF 15wt.%	61.9	11.88
	PEI/CF 20wt.%	61.1	8.36
Perez et al. [76]	ABS/Jute fiber 5wt.%	25.9	1.54
Shofner et al. [77]	ABS/VGCF 10wt.%	37.4	0.8
Ferreira et al. [78]	PLA/CF 15wt.%	53.4	7.54
Shofner et al. [79]	ABS/VGCF 5wt.%	27	1.27
	ABS/5wt.% SWNT	32.5	1.74
Compton and Lewis [80]	Epoxy/SiC/CF 10wt.%	66.2	24.5
Mahajan et al. [81]	Epoxy/CF 15wt.%	66.3	4.05
Gardner et al. [82]	PEI/CNT 4.7wt.%	125.3	3
DeNardo [83]	PPS/CF 50wt.%	92.2	26.4

Table 11. Mechanical data for discontinuous fiber systems loaded parallel to the printing direction

References	Materials	Tensile strength (MPa)	Tensile modulus (GPa)
Duty et al. [75]	ABS/chopped CF 20wt.%	6.8	1.98
	ABS/CF 15wt.%	5.8	1.83
	PEI/CF 20wt.%	4.3	1.1
Love et al. [67]	ABS/CF 13vol.%	7	1.52
DeNardo [83]	PPS/CF 50wt.%	9.72	2.6
Ferreira et al. [78]	PLA/CF 15wt.%	35.4	3.92
Mahajan et al. [81]	Epoxy/CF 15wt.%	46	2.84
Duty et al. [74]	ABS/CF 20wt.%	10.3	2.1
	ABS/GF 20wt.%	15.3	2.5
Compton [80]	Epoxy/SiC/CF 10wt.%	43.9	8.06
Hill et al. [72]	ABS/CF 20wt.%	12.8	2.6
Kunc [73]	ABS/CF 13vol.%	13	2.2

Table 12. Mechanical data for discontinuous fiber-loaded perpendicular to the printing direction.

2.4 Conclusion

The prepared literature review section summarizes past published work on Fused Filament Fabrication (FFF) with fiber reinforced polymeric materials. Influencing parameters in the FFF process such as road width, print speed, layer thickness, feed rate and build temperature of the model (both liquefier and envelope temperature), fiber orientation, the layer position, volume fraction, and infill orientation have been studied. These parameters considered in the strength/bonding or physicochemical characterizations of FFF-fabricated parts have been presented in detail. An overview of mechanical properties of printed parts for different composite material systems is presented and discussed. Three types of reinforced polymers in the FFF process have been considered: powder reinforced polymers, continuous fiber-reinforced polymers, and short fiber reinforced polymers. This study covers the way for the development of a design support system for components printed with the FFF process. Indeed, the industrial world is using this technology more and more in the production of the complex small series parts. The knowledge produced by this report will help to better formalize methods and tools to optimize the design process of composite parts under different mechanical constraints.

3 Material description, 3D printer device and characterization methods

3.1 Materials

The used materials as raw materials were polyamide 6 (PA6) with commercial name of Nylon White, and reinforced PA6 by chopped carbon fiber with commercial name of Onyx. Onyx and Nylon White material were fabricated and developed by MarkForged®. As for the continuous reinforcement, the continuous glass fibers were utilized for continuous reinforced composite manufacturing. The used glass fibers were also supplied by MarkForged®. The fiber filaments consisted on a mixture of a bundle of long fibers and a polymer (nylon), forming a pre-impregnated-like material. The diameter of the glass fiber bundles was approximately 300 μm with the density of 1.5 g/cm^3. The average individual fiber diameter of the used glass fibers within the bundles was 8.5 μm. The quantity of fibers per bundle was around 1000. The polymer accumulation appears around fibers but porosity was very low. This fact leads to conclude that porosity appears on the printed laminates as a consequence of a non-adequate bonding between filaments [84]. The manufactured specimens for the experimental purposes were made of PA6, short carbon fiber-reinforced PA6 composites, continuous glass fiber-reinforced PA6 composites, and reinforced short carbon fiber-reinforced PA6 by continuous glass fiber, according to the below explanations.

3.1.1 Manufactured specimens made of polyamide 6 (PA6)

The manufactured specimens made of PA6 were fabricated by the utilization of Nylon White filament which was developed by MarkForged®. The nominal diameter of this filament was about 1.75 mm. The reported elongation value at break is 150% [85]. The manufactured specimens made of PA6 were considered for experimental studies of the effects of some process parameters on thermal and mechanical properties of the printed specimens, the effect of the deposition direction of continuous glass fiber, and the effect of density of continuous glass fiber on the mechanical behavior of the printed specimens.

3.1.2 Short carbon fiber-reinforced polyamide 6 composite (CF-PA6) specimens

The manufactured specimens made of short carbon fiber-reinforced PA6 composites were fabricated by the utilization of Onyx filament which was developed by MarkForged®.

The nominal diameter of this filament is about 1.75 mm. In fact, this filament which has been introduced as a matrix for fabrication of the polymer composite parts, is also a composite material by itself. It is a combination of engineering plastic as matrix and chopped carbon fibers as reinforcements with the mass content of 93.49% and 6.51%, respectively. The mass content values were calculated by pyrolysis processing of a piece of the used filament. It is a specially tuned PA6 copolymer (polyamide) filament with a chopped carbon fiber blend, adding a great strength and a unique stiffness to FFF printing. The used Nylon White (PA6) and Onyx (CF-PA6) filaments have a diameter of 1.75 mm. The manufactured specimens made of short carbon fiber-reinforced PA6 composites were considered for experimental studies of the effects of some process parameters on thermal and mechanical properties of the printed specimens, the effects of the infill density and infill pattern, and the fatigue behavior of the printed specimens.

Technical data sheet of the used materials is tabulated in table 13, was obtained from [85].

Properties	**Onyx (PA6-CF)**	**Nylon (PA6)**	**Glass fiber**
Tensile Modulus (GPa)	2.4	1.7	21
Tensile Strength (MPa)	/	/	590
Tensile Stress at Break (MPa)	37	36	/
Tensile Strain at Break (%)	25	150	3.8
Flexural Strength (MPa)	71	50	200
Flexural Modulus (GPa)	3	1.4	22
Heat Deflection Temp (°C)	145	41	105
Density (g/cm^3)	1.2	1.1	1.5

Table 13. Technical data sheet of the used materials [85].

3.1.3 Continuous glass fiber-reinforced polyamide 6 (PA6) composite specimens

The manufactured specimens made of continuous glass fiber-reinforced PA6 composites were considered for experimental studies of the effects of the infill density and infill pattern. These specimens were made of Nylon White filament and continuous glass fiber spool which have been developed by MarkForged®.

3.1.4 Reinforced short carbon fiber-reinforced polyamide 6 (PA6) by continuous glass fiber

The manufactured specimens made of reinforced short carbon fiber-reinforced PA6 by continuous glass fiber were manufactured by use of Onyx filament as short carbon fiber-reinforced PA6 and continuous glass fiber spool for structure reinforcement. These specimens were considered for experimental studies of the effects of the infill density and infill pattern, and the fatigue behavior of the printed specimens.

3.2 Methods

3.2.1 Introducing the case study model

During the FFF/FDM process, each deposited raster has its own effect on different aspect of the manufactured part. In other words, the thermal, mechanical, and rheological characteristics of the final manufactured parts are affected by the different deposition mechanisms. The deposition mechanisms strongly affect the:

- Inter-diffusion of adjacent filaments and thus bonding
- Quality and finish surface of the final part
- Mechanical strength of the final part

During this study, it is tried to design a test model/sample which let us to realize the requirements. An extruded filament faced with various heat transfer mechanisms due to the different heat sources among the manufacturing process. Consequently, the physical contacts resulting from the deposition mechanisms, also play an important role in the characterization and analysis. So, a single deposition road (a single wall layer sample) has been modeled including the following characteristics (Fig.59):

- Homogeneous deposition of filaments on top of each other
- Unidirectional deposition of filaments (Consideration the time of deposition for each filament)
- Same convection of layers with the environment
- Same conduction between layers
- 1st layer: conduction with support (and with 2nd layer) simultaneously (for thermal characterization)

- 2nd, 3rd, …, nth layers: same conduction with each other
- Symmetric effect of environment and platform temperature on the solidification of material while cooling down.

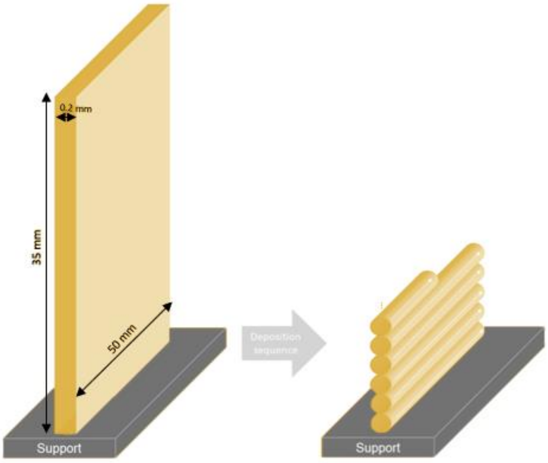

Fig. 59. Schematic of the designed test case

3.2.2 3D Printers

Two different printers have been utilized during our studies. To study the effects of the process parameters, Flashforge ADVENTURER-3 was utilized. This printer permits us to choose the different values for the main excerpted and studied process parameters, which were bed temperature, nozzle temperature, layer height, and print speed. Then, the effect of each stated process parameters were studied on the rheological behavior of the raw materials through the FFF process and consequently the final manufactured parts. The different components of this printer are introduced below (Fig. 60):

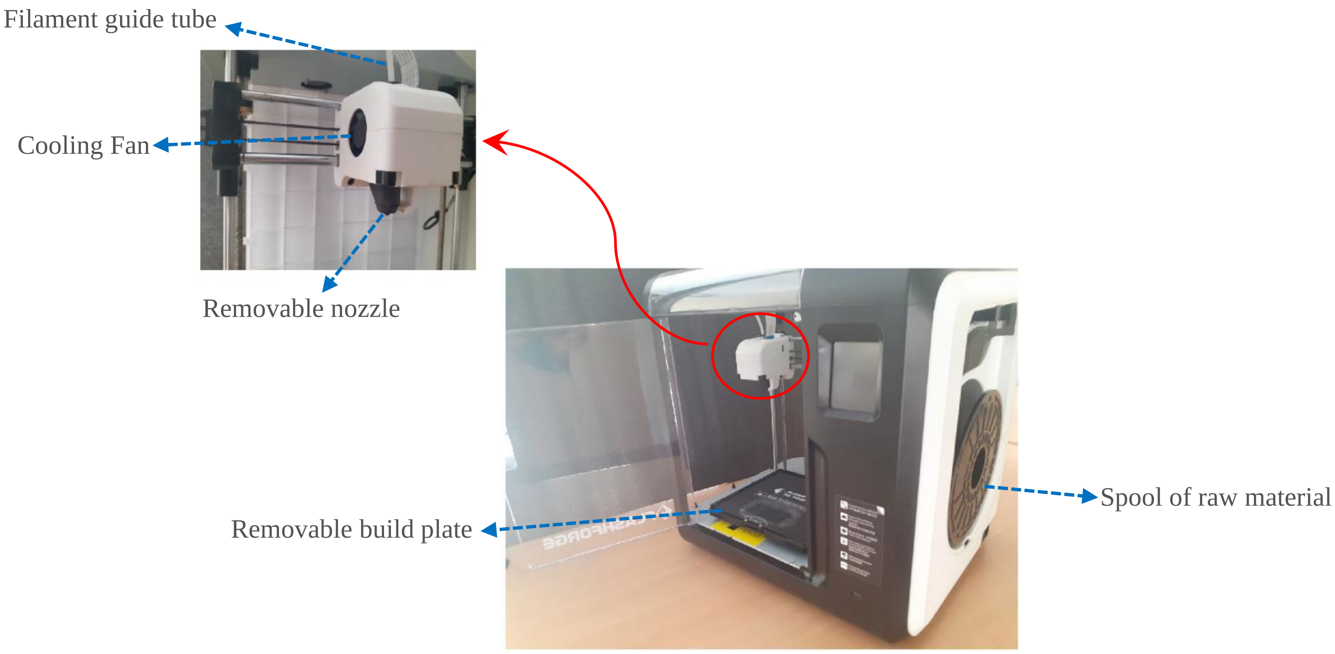

Fig. 60. The different components of Flashforge ADVENTURER-3.

As for studying the infill percentage, infill pattern effects and fatigue behaviors, Markforged-Mark Two printer was utilized. In fact, one of the Markforged’s desktop printers, is Mark Two Printer (Fig. 61). This printer is used to print the parts from Nylon White (PA6) or Onyx (PA6 reinforced by chopped carbon fibers) which are manufactured by Markforged. By the way, it is possible to use continuous reinforcements fibers (carbon or, glass or Kevlar) for manufacturing the continuous fiber-reinforced polymer composites by means of Markforged-Mark Two printer. Some of the stated technical specifications related to Mark Two printer are listed in Table 14 [85].

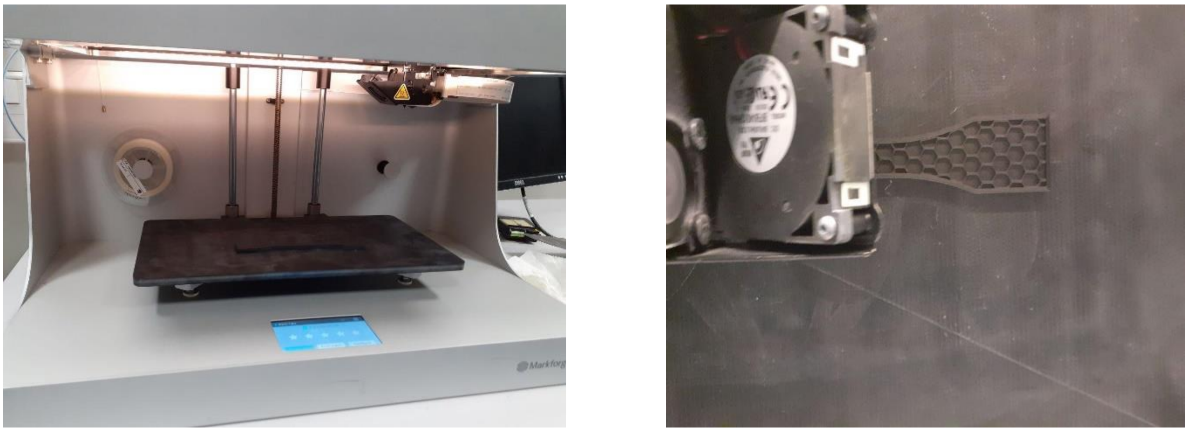

Fig. 61. Mark Two printer (Left) and printer during the print of the required specimens.

Build Volume	320 x 132 x 154 mm (12.6 x 5.2 x 6 in)
Plastics Available	Onyx, Nylon White
Fibers Available	Carbon fiber, fiberglass, Kevlar, HSHT fiberglass (High-Strength High-Temperature Fiberglass)
Layer Height	100 µm default, 200 µm maximum
Infill	Closed cell infill: multiple geometries available

Table 14. Technical specifications for Mark Two printer [85].

The Mark Two 3D printer has two nozzles, the first is related to Onyx or Nylon White (Matrix) and second nozzle is allocated to the deposition of continues fibers (Carbon fiber, fiberglass, Kevlar, HSHT fiberglass) as reinforcements. In fact, this machine can print two kind of materials independently and, hence, it has two nozzles. The different components of mark two printer are clarified in below (Fig. 62).

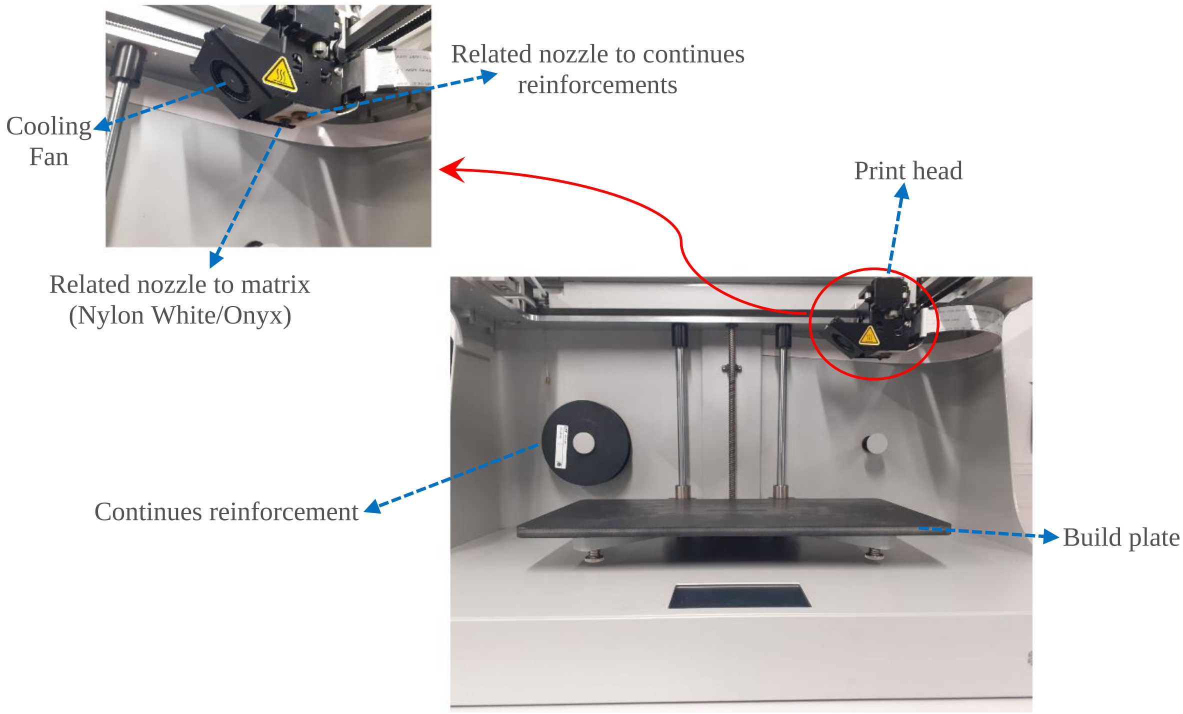

Fig. 62. The different components of Markforged-Mark Two.

As was stated, Mark Two has the ability to fabricate parts with different infill patterns and percentages. It is possible to choose three types of infill patterns, which are rectangular, triangular and hexagonal (Fig. 63).

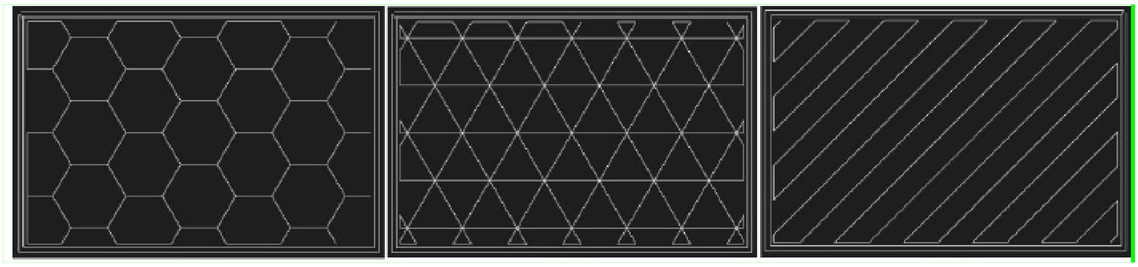

Fig. 63. Infill patterns displayed in the Mark Two printer slicer (Eiger software).

3.2.3 Selected subset of process parameters

There are miscellaneous process parameters provided by different 3D printer machines. The process parameters play an important role in terms of the adhesion between the printed layers and mechanical property of the manufactured parts by the additive manufacturing process. The main prepared process parameters of FlashForge Adventurer 3 printer, examined in this work are tabulated in table 15.

Condition No.	$T_{Liquefier}$ (°C)	T_{Bed} (°C)	V (mm/s)	Layer height (mm)
No. 1	220 230 240	25±0.5	15	0.1
No. 2	240	25±0.5	13 15 17	0.1
No. 3	240	25±0.5	15	0.1 0.2 0.3
No. 4	240	25±0.5 50±1 70±1 90±1	15	0.1

Table 15. The excerpted FFF process parameters

In other words, the effects of four main process parameters of liquefier temperature ($T_{Liquefier}$), bed platform temperature (T_{Bed}), print speed (V), and layer height (h) on the manufactured specimens by FFF were studied. The printing conditions of specimens for evaluation purposes of the liquefier temperature, print speed, layer height, and bed platform temperature effects are sorted as conditions NO. 1, 2, 3, and 4 in table 15, respectively.

3.2.4 In-situ monitoring of temperature evolution

An Optris PI450 infrared camera was used in the conducted study of the process parameters effects on thermal and mechanical properties of polymer and polymer-based composites using FFF process. The stated infrared camera was used by considering the determined and specific distance from the extruder to achieve a suitable plain field of view (FOV) of the all consecutive printed and deposited layers (Fig. 64). As for some technical data of the used infrared camera, the related frame rate, optical resolution, frequency, wavelength range, and accuracy values were 80 Hz, 382*288 pixels, 32 Hz, 8-14 μm, and 2%, respectively. Also the composite self-heating during the applied fatigue test has been measured on the surface of the specimen by means of the stated camera.

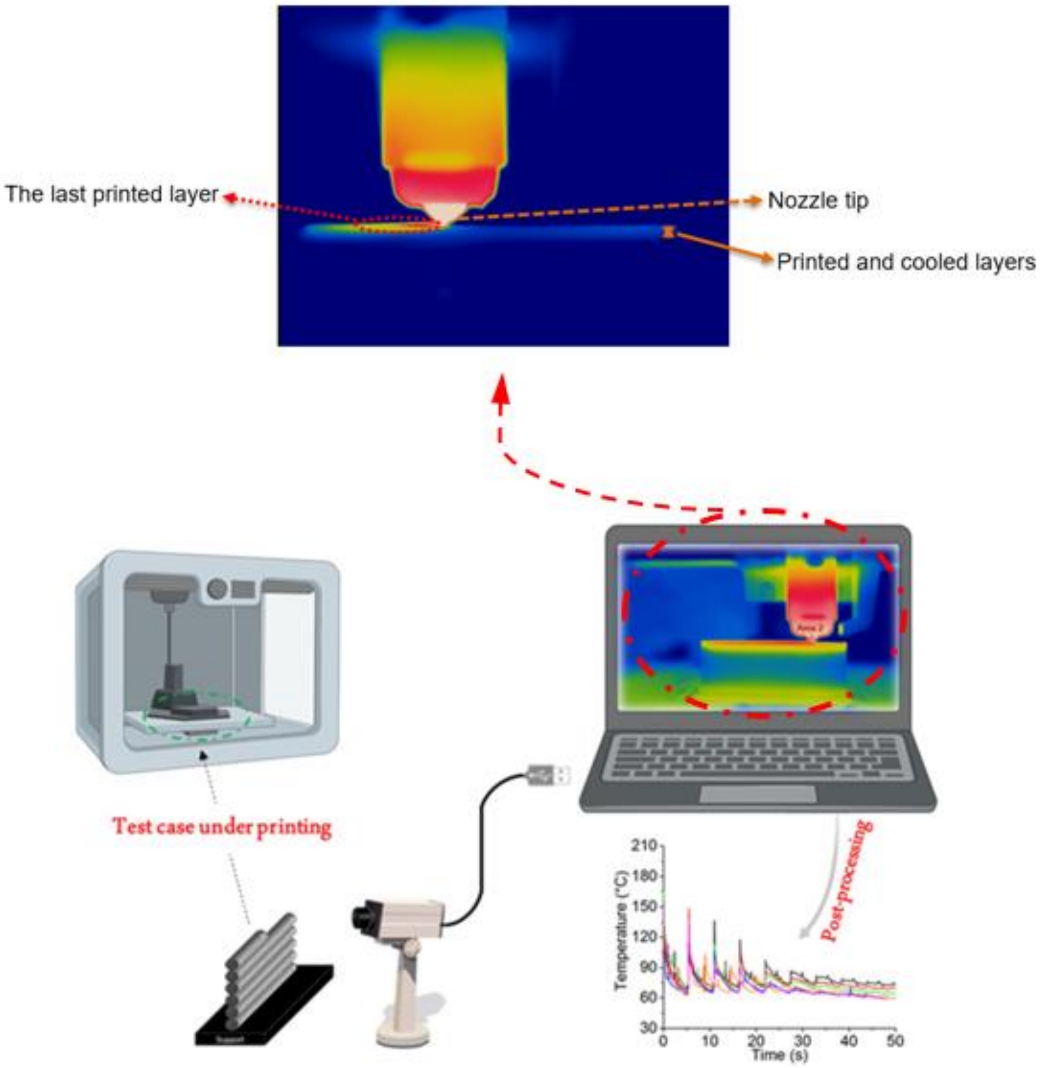

Fig. 64. In-situ monitoring of temperature evolution during FFF process

3.2.5 Microstructural observations

The ZEISS Optical microscope (OLYMPUS BH2) with 100 and 200 µm magnifications was utilized for observation of the used raw material, which was reinforced PA6 by about 6.5Wt% chopped carbon fiber (CF-PA6). As for qualitative observation of the printed specimens at the different selected process parameters the Scanning Electron Microscope (HITACHI 4800 SEM – high resolutions) was applied.

3.2.6 Physico-chemical characterization

3.2.6.1 Differential Scanning Calorimetric (DSC)

By means of DSC, the difference of temperature between the sample and reference during heating was determined. Differential Scanning Calorimetry provided the possibility to determine glass transition and crystallization temperature, heat capacity of the used raw materials and printed specimens at the selected processing parameters. The measurements were carried out by means of DSC Q1000. It allows the characterization of used filaments. The DSC characterization of the raw materials was carried out in three ramps in the temperature range of -20°C to 220°C. The thermal history of the sample was erased in the first ramp. So, the obtained results are measured under controlled conditions. The heating and cooling rate values were 10 °C/min. While, the DSC characterization of the printed specimens were performed in two ramps (heating and cooling) with the heating and cooling rate values of 10 °C/min and the temperature range of 20°C to 220°C.

3.2.6.2 Infrared spectroscopy (FTIR)

This method involves the interaction of infrared radiation with matter. It covers a range of techniques, mostly based on absorption spectroscopy. The IR spectrum can be visualized in a graph of infrared light absorbance (or transmittance) on the vertical axis vs. frequency or wavelength on the horizontal axis. Typical units of frequency used in IR spectra are reciprocal centimeters (sometimes called wave numbers), with the symbol cm^{-1}. The PerkinElmer FT-IR spectrometer was utilized to characterize the used filaments (Onyx and Nylon) by comparing the obtained curves and patterns with the reported ones by other researchers.

3.2.7 Thermo-mechanical behavior analysis

Thermo-mechanical analysis (DMTA) flexural tests have been attained under the multi frequency situation to measure the major transition temperatures and the viscoelastic characteristics on the printed samples, using the DMA Q800 instrument from TA Company. The flexural test was conducted at the following condition: temperature range varying from 10 to 80 ºC, temperature rate of 2 ºC/min, and the frequencies of 1, 2, 5, 10, and 30 Hz.

3.2.8 Rheological characterization

The rheological characterization of the Onyx and Nylon White filament was determined by means of Rheometer MCR502 from Anton paar. The experimental tests were applied under the protected atmosphere by Nitrogen flow. The filaments of the stated raw material were cut into several pieces to cover the utilized parallel plate configuration surface. By aid of this experiment, the viscoelastic behaviors of materials in both of the Newtonian and Non-Newtonian zones at the different applied printing temperature values of 210°C, 220°C, 230°C, and 240°C were determined.

3.2.9 Mechanical characterizations

3.2.9.1 Quasi-static tensile test

As for studying the process parameters effects, the tensile specimen was cut from the printed specimen (Fig. 65), which were printed under the decided parameters. The related dimension of the used sample for mechanical test was according to ISO 527-2 (Fig. 66). Quasi-static tensile experiments have been achieved with the INSTRON 4301 machine under the displacement rate of 5 mm/min. In fact, according to the printed specimen (Fig. 65), the prepared mechanical test samples were from the printed single wall layers, which had 0-degree as raster angle. A minimum of three specimens were prepared to perform tensile tests.

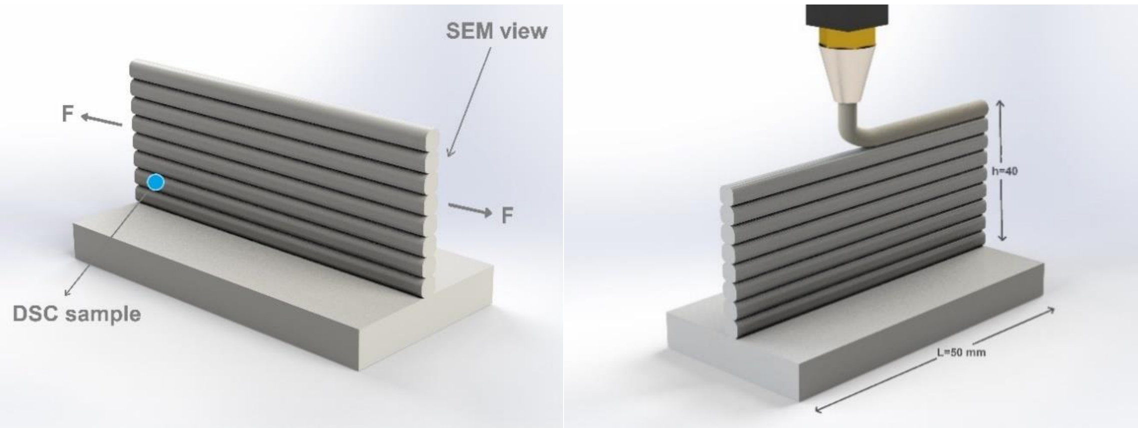

Fig. 65. Schematic of the printed specimen and sampling for different characterizations

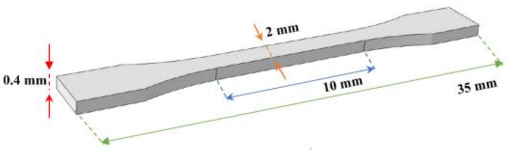

Fig. 66. Geometry of the used specimen

To study the effect of infill patter and infill density of the printed material, the samples were cut according to the standard ISO 527-1. The related dimension of used sample for mechanical test is according the Fig. 67. Quasi-static tensile experiments have been achieved with the INSTRON 5966 machine, loading cell of 10 kN, and the displacement rate is 5 mm/min. In order to reproducibility of the results, at least four samples were carried out in Tensile Test study.

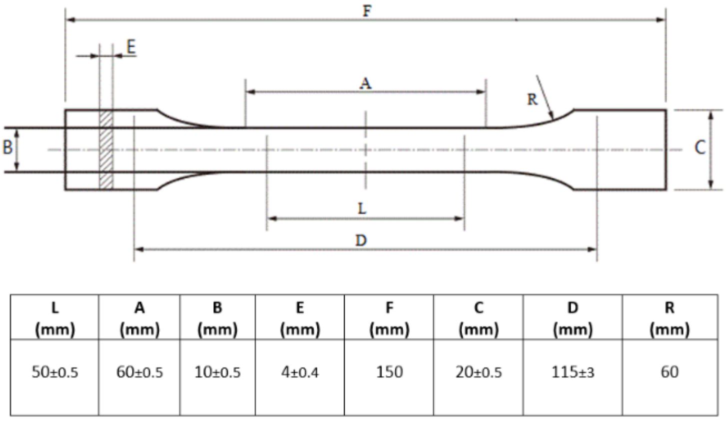

L (mm)	A (mm)	B (mm)	E (mm)	F (mm)	C (mm)	D (mm)	R (mm)
50±0.5	60±0.5	10±0.5	4±0.4	150	20±0.5	115±3	60

Fig. 67. Specimen geometry and its related dimensions for tensile and fatigue loadings

3.2.9.2 Fatigue test

Three points bending fatigue tests have been performed at different applied maximum strain (ε_{max}). This experiment was performed on carbon fiber-reinforced PA6 composites (CF-PA6) and reinforced (CF-PA6) with continuous glass fiber specimens. The minimum applied strain (ε_{min}) was chosen to be equal to 10% of the maximum applied strain. The chosen strain-ratio was thus ($R_{\sigma} = 0.1$), and the mean strain-level was equal to 0.55 ε_{max}. During fatigue loading, the temperature rise was measured, too.

Three points bending fatigue tests have been performed at different applied maximum strain (ε_{max}). The minimum applied strain (ε_{min}) was chosen to be equal to 10% of the maximum applied strain. The chosen strain-ratio was thus ($R_{\sigma} = 0.1$), and the mean strain-level was equal to 0.55 ε_{max}.

During the fatigue tests, the temperature rise, due to the composite self-heating, has been measured on the surface of the specimen using an infrared camera (Raynger- MX4). An Optris PI450 infrared camera was used (Fig. 68).

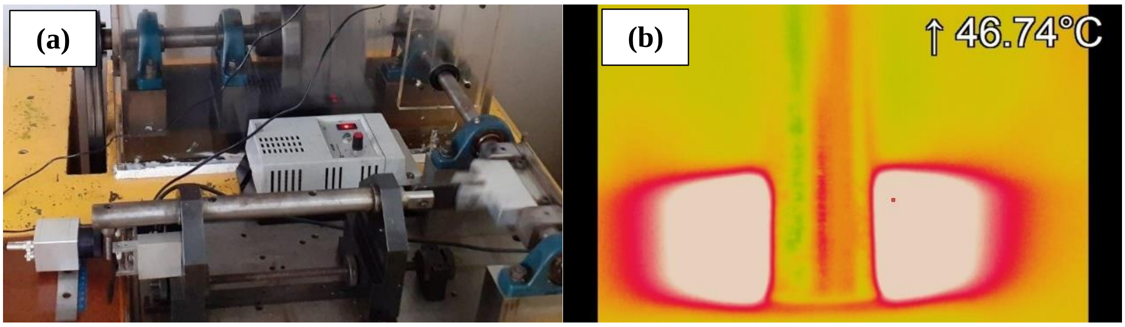

Fig. 68. The sample under the three-point bending fatigue test (a) temperature measurement during the fatigue test by the infrared camera (b)

Also, the macroscopic damage evolutions have been estimated through the measurement of Young’s modulus evolutions. Microscopic damage observations were performed by subjecting CF-PA6 specimens into a fatigue loading under specific loading amplitude with a frequency of 10 Hz. The observation area corresponded to a polished thickness surface of the rectangular composite with a geometry of 120 × 10 × 4 mm^3.

4 Results and discussions

In this section, the obtained results of the all applied characterization methods will be discussed. Firstly, the obtained results will be presented then will be followed by the related discussions. As it was stated, for improving and solving the weak adhesion between the deposited layers in FFF process, it is important to identified the material parameters, machine parameters, and the process parameters. To achieve this aim, the solution is to consider both temperature and viscosity parameters. And establish the Time-Temperature-Transformation diagram for process optimization. This helps us to determine the processability area. Then, by understanding the effect of the effective parameters on the performance of the manufactured parts, the optimum parts in viewpoints of mechanical properties and dimensional stability will be able to be manufactured and achieved.

4.1 Primary characterizations

4.1.1 Microstructural analysis

According to the observation of the carbon fibers (Microscopy Observation) under the optical microscopy, the size range of the disturbed chopped carbon fibers was about 10 to 312 micrometers, according to Fig. 69(a). In fact, Fig. 69 (a) is related to microstructure observation of chopped carbon fibers in the utilized PA6-CF filament, after pyrolysis at 500°C for 5h. Also, it was observed that the chopped carbons of the CF-PA6 filament, were directional (Fig. 69 (b)). Moreover, the microstructure of CF-PA6 reinforced with glass fiber can be observed in Fig. 69 (c). The continuous glass fiber is marked at the top of figure 69 (c).

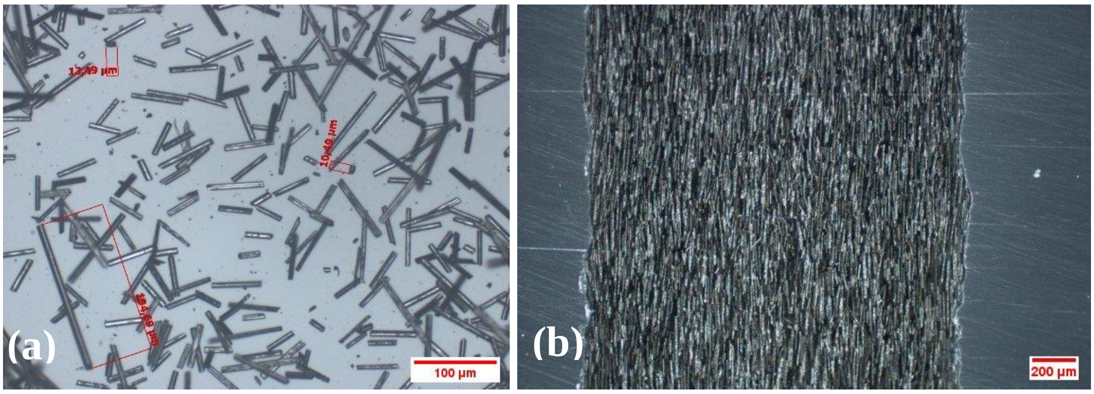

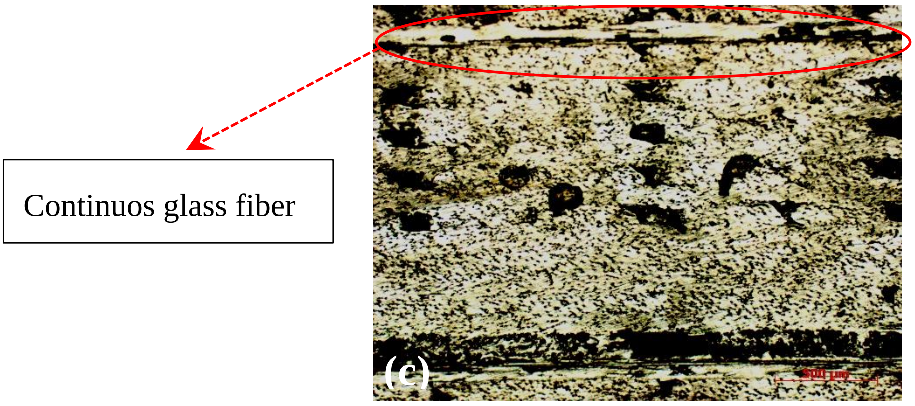

Fig. 69. Microscopy observation of the chopped carbon fibers in the used CF-PA6 filament (a), a piece of CF-PA6 filament (b), and CF-PA6 reinforced with continuous glass fiber (c)

4.1.2 Thermal analysis

As for characterizing the used filament, the DSC method was applied on the pieces of the used raw materials, commercially named Nylon White (PA-6) and Onyx (CF-PA6). As for the result, the below curves (Fig. 70 (a) and Fig. 70 (b)) were obtained. The obtained glass transition, melting and crystallization temperatures were identified in Fig. 70.

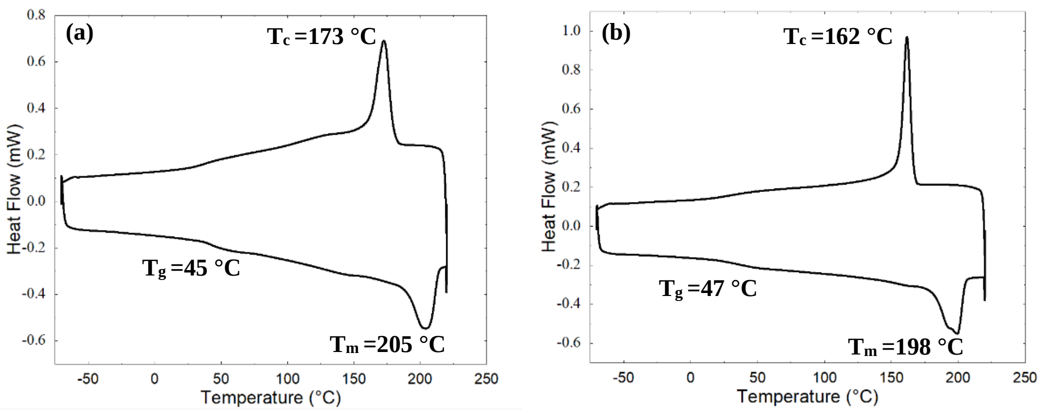

Fig. 70. DSC characterization of (a) PA6 filament and (b) short carbon fiber-reinforced PA6 (CF-PA6) filament

4.1.3 FTIR results

As for characterizing the used filament, the used filaments were applied FTIR characterization. According to the obtained results (Fig. 71 and Fig. 72) in comparison with the reported pattern curve by Krylova et al. [86], it was found out that Nylon White filament and also the matrix of Onyx filament were PA6.

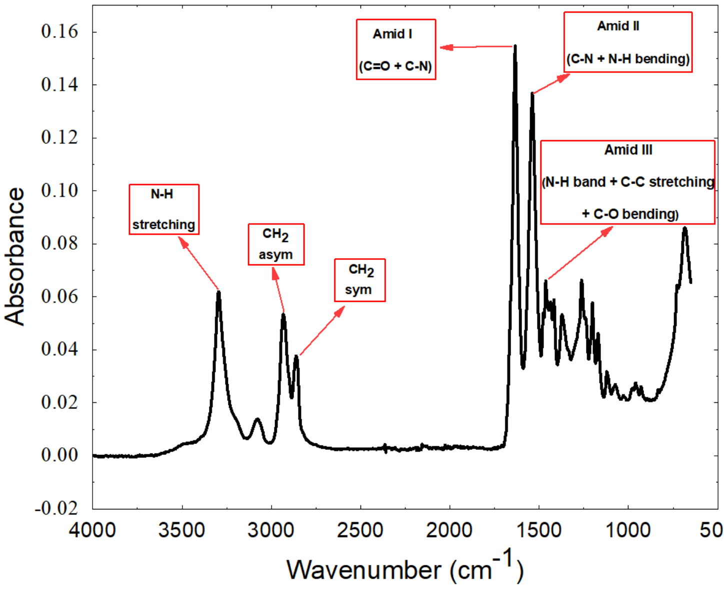

Fig. 71. FTIR spectrum of CF-PA6 (Onyx)

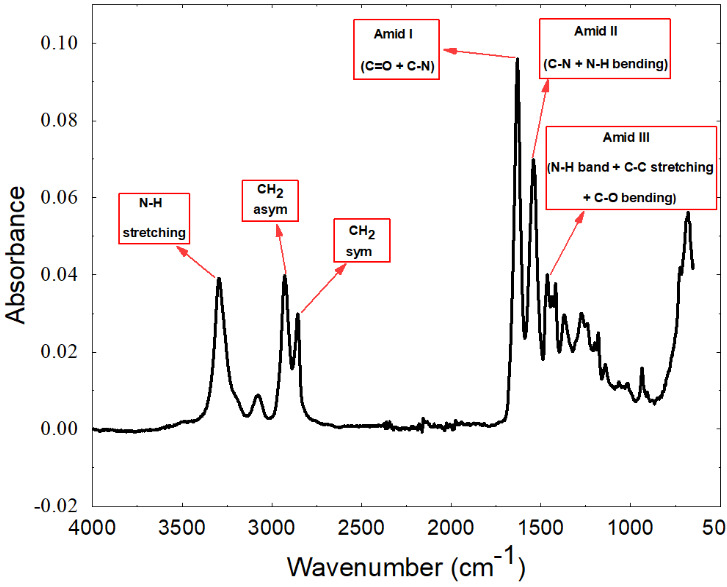

Fig. 72. FTIR spectrum of PA6 (Nylon White)

4.1.4 Thermo-mechanical behavior characterization

The thermo-mechanical behavior characterization of PA6-CF filament was conducted using the DMTA test. As for the result, the below curve (Fig. 73) was obtained. Main transition temperatures due to molecular mobility as a function of the temperature have been measured using the DMTA test. As it can be noticed, CF-PA6 presented a glass transition of nearly 47 ºC.

Main transition temperatures due to molecular mobility as a function of the temperature have been measured using the DMTA test. This test can be useful to analyze the induced self-heating phenomenon and to relate it to the measured temperature rise during a fatigue test at different amplitudes.

The elastic or viscous response of CF-PA6 can be measured as a function of temperature using DMTA; it is possible to understand the true internal damping of the system. One can suppose that CF-PA6 has rigidly stability at ambient temperature while the storage modulus continuous to decrease slowly until 80°C due to the increase of macromolecular chain mobility.

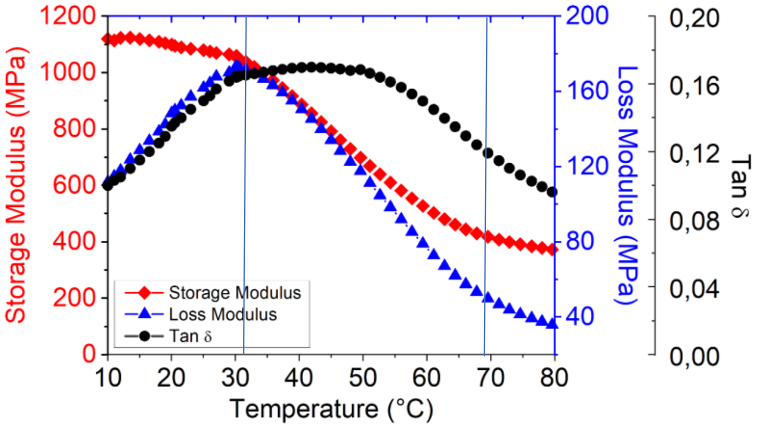

Fig. 73. DMTA test result: Evolution of the storage, loss moduli, and loss factor versus temperature

However, since the thermomechanical behavior of the polymer determines the diverse transitions and change of physical state of polymer, DMTA test is implemented using the alternating bending configuration (with the frequency of 1Hz). The obtained result is shown in Fig. 73 including three physical state: glassy state, glass transition zone, and rubbery state. As can be seen in Fig. 73, the material shows a glassy state up to ~30 °C. In glassy state, E' is relatively high (~1100 MPa). The second zone (30 °C <T< 65 °C) correspond to glass transition zone. E' decreases drastically from ~1100 MPa to a value lower than 400 MPa. The rubbery state of the material is then the zone of temperature higher than 65 °C. Presumably, the value of E' is low and the sample is relatively soft.

4.1.4.1 Viscoelasticity modeling by Cole-Cole principle

Various approaches have been used to study the viscoelastic properties in the temperature range between the glassy and rubbery domain, and different models have been proposed to predict these properties. These models generally represent the curve of E" (loss modulus) as a function of E’ (storage modulus), and the curve is known as the Cole-Cole diagram. For the validation of the theoretical model, experimental data obtained by the dynamic mechanical, thermal analysis (DMTA) tests are required. After DMTA tests, an asymmetric Cole-Cole diagram has been plotted (Fig. 74). The behavior of polymers can be analyzed by the bi-parabolic model according to the Perez model, the equation is as follow:

$$E^{*} = E_0 + \frac{E_\infty - E_0}{1+(i\omega\tau)^{K} + Q(i\omega\tau)^{K'}} = E' + iE'' \tag{Eq. 1}$$

With

$$E' = E_0 + (E_\infty - E_0)\,\frac{1+\cos(\frac{k\pi}{2})(\omega\tau)^{-K} + Q\cos(\frac{k'\pi}{2})(\omega\tau)^{-K'}}{D} \tag{Eq. 2}$$

$$E'' = (E_\infty - E_0)\,\frac{\sin(\frac{k\pi}{2})(\omega\tau)^{-K} + Q\sin(\frac{k'\pi}{2})(\omega\tau)^{-K'}}{D} \tag{Eq. 3}$$

and

$$D = [1+\cos(\frac{k\pi}{2})(\omega\tau)^{-K} + Q\cos(\frac{k'\pi}{2})(\omega\tau)^{-K'}]^2 + [\sin(\frac{k\pi}{2})(\omega\tau)^{-K} + Q\sin(\frac{k'\pi}{2})(\omega\tau)^{-K'}]^2 \tag{Eq. 4}$$

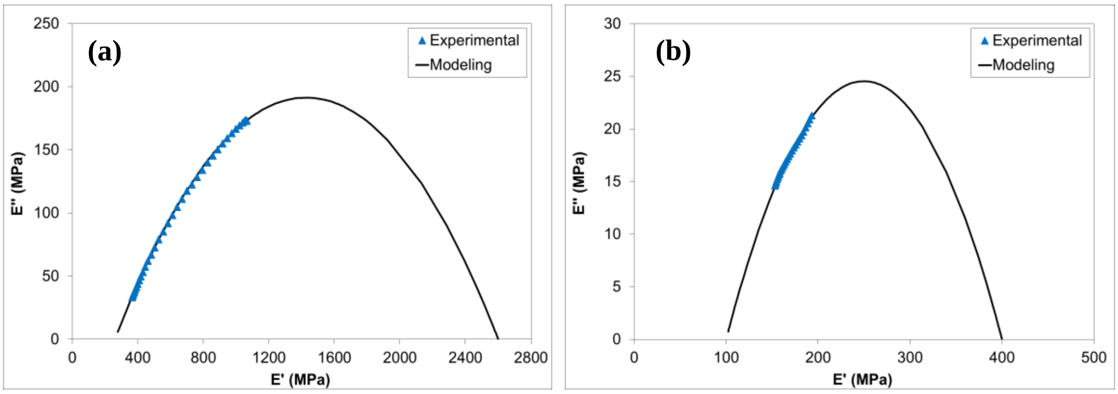

Fig. 74. Cole-Cole plot of (a) CF-PA6 + GF and (b) CF-PA6

Where k and k´ and Q are the constants of this model. ω = 2πf is the angular frequency (f = frequency) Furthermore, E* is the complex shear modulus: E_∞ and E_0 are the value of modulus at the respectively glassy and rubbery states. k and k´ depend on the slope of the tangents at the beginning and the end of the Cole-Cole diagram (dE”/dE’), Q is a constant related to the maximum value of E". τ is the average relaxation time.

Material	Frequencies (Hz)	E_0 (MPa)	E_∞(MPa)	k	k'	Q	τ (s)
CF-PA6	1	100	400	0.2	0.22	0.5	0.5
CF-PA6 + GF	1	260	2600	0.2	0.22	0.5	0.5

Table 16. Perez model parameters for CF-PA6 and CF-PA6 + GF

The values of the model's parameters are shown in table 16. The theoretical curve fits perfectly with the experimental results, signifying that the bi-parabolic model can accurately predict the viscoelastic behavior of CF-PA6.

4.2 Effect of process parameters on thermal and mechanical properties of polymer-based composites

The Fused Filament Fabrication (FFF) process of polymer-based composites has been developed due to its capability to make complex geometries and shapes with reasonable mechanical properties. However, the improvement of mechanical properties of the obtained parts and products are still under study and are interesting for designers. There are several strategies to enhance these desired properties of produced pieces, for example optimizing the process parameters and/or using different architecting designs. It has been attempted to evaluate the effects of some important and overriding process parameters (liquefier temperature, print speed, layer height, and platform temperature) on the temperature evolution and mechanical behavior of PA6 reinforced with chopped carbon fibers samples produced by Fused Filament Fabrication (FFF). Due to deposition of multilayers, there is a cyclic profile of temperature in the FFF process which is a considerable note related to fabrication and consequently the strength of the manufactured parts. In parallel with the study of process parameters effect, this cyclic temperature profile has been measured. The preliminary results related to physicochemical and mechanical properties revealed that differences in crystallinity percentage exist and failure stress/strain can be considered as an indicator to evaluate the mechanical properties of FFF manufactured products. Moreover, measuring the temperature profile of the deposited filaments revealed that process parameters have a considerable influence on the cooling process of deposited filaments which itself affects the bonding of adjacent filaments. The higher temperatures led to slower cooling rate. Finally, the results confirm the impact of mentioned parameters roles on the bonding formation in the FFF process and also the subsequent obtained mechanical properties of the printed parts. Therefore, selection of the optimized and suitable process parameters is an important design consideration.

As was stated in the previous section (3.2.1), a specimen with single wall layers, which was formed from the deposited layers (with 0-degree as raster angle) were considered for experiments and the subsequent analyses (Fig. 65). This specimen had the below condition during the manufacturing:

A reference sample with specific process parameters was printed (liquefier temperature: 240°C, print speed: 15 mm/s, layer height: 0.1 mm, platform temperature: 25°C). Then the effect of the selected process parameters (Table 15) have been taken into account to be compared with the stated reference process parameters. In this regard, physicochemical and mechanical characterizations were conducted, also the temperature profile of the first deposited layer was monitored in-situ through deposition of the next deposited layers. Finally, the obtained results were utilized to evaluate the impact of each process parameter on the manufactured objects.

The obtained tensile test curve and the tensile properties values of the reference sample from the tensile test are presented in Fig. 75 and the prepared table in the appendix section. Three samples have been tested. The failure stress and failure strain are about 60 MPa and 30%.

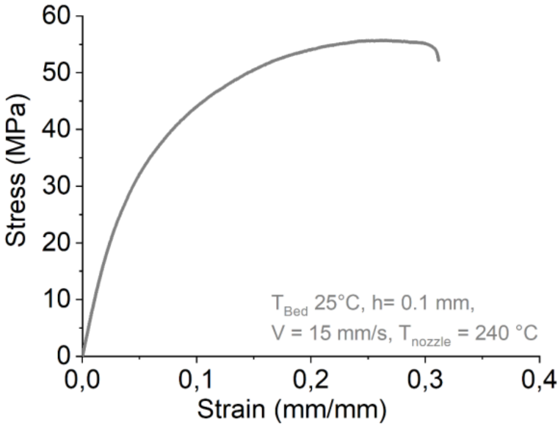

Fig. 75. Tensile results for reference sample

Some efforts were made using local measurements to record the temperature profile of the deposited consecutive layers in different locations. The recorded temperature profile was considered for the first deposited layer during the deposition of other layers in a sequence of deposition at a determined location from the commencement of deposition (Fig. 76). The objective was to find out the temperature profile of the deposited consecutive layers during the FFF process by means of spot in-situ measurement.

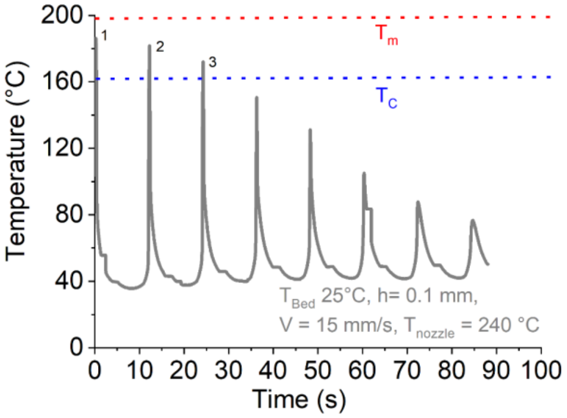

Fig. 76. The obtained curve related to the temperature profile of the first printed layer during the deposition of other layers in the reference sample

4.2.1 Influence of liquefier temperature

The effect of the liquefier temperature as one of the most important process parameters has been considered. According to obtain the possibility to study the effect of liquefier temperature, three different values of 220, 230, and 240 ºC were considered for comparing their results, in case of manufactured samples made of CF-PA6 and also PA6. According to the obtained DSC curves corresponding to the printed specimens under different liquefier temperature (220, 230, and 240 ºC), by changing the liquefier temperature the crystallization degree and the related heat flow values of the crystallinity was changed (Fig. 77), not significant. The obtained crystallization degree of the manufactured PA6-CF samples corresponding to the stated different liquefier temperature values are tabulated in table 17.

The obtained results from DSC curves related to the crystallinity zone were taken into account significantly. Because the diffusion and consequently the adhesion and bonding of the printed layers occurs in this zone, also it can also directly affect the dimension accuracy of the printed samples.

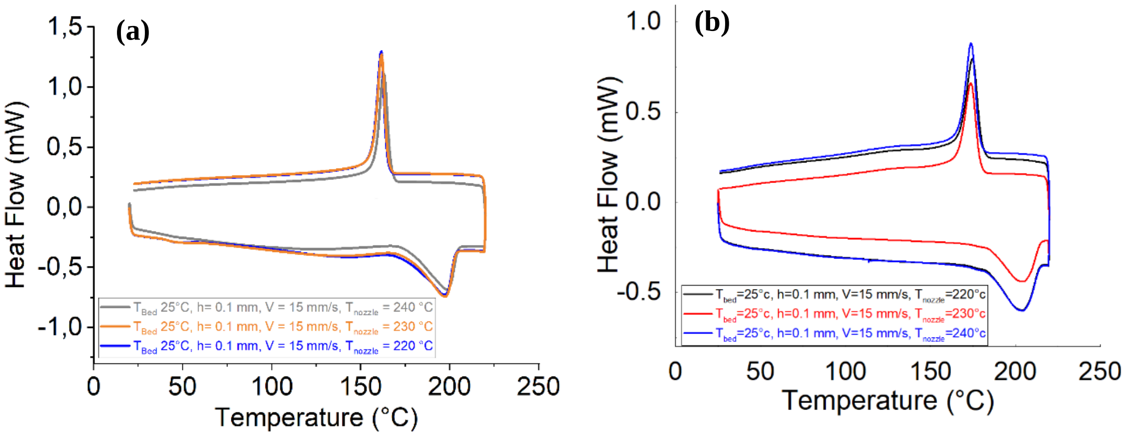

Fig. 77. DSC results for fabricated samples CF-PA6 (a) and PA6 (b) under the different liquefier temperatures

	Conditions	T_c (°C)	T_m (°C)	%Crystallinity
No. 1	$T_{Liquefier}$ = 220 °C	161.5°C	197.5°C	19.97%
	$T_{Liquefier}$ = 230 °C	161.7°C	197.7°C	20.26%
	$T_{Liquefier}$ = 240 °C	162.8°C	198.7°C	20.51%

Table 17. The obtained values related to different properties from DSC curves of the printed CF-PA6 samples

Fig. 78 illustrates the tensile behaviors of the printed CF-PA6 specimens under the considered and stated liquefier temperature values. The maximum tensile strength of the printed specimens under the liquefier temperature of 220 °C, 230 °C, and 240 °C were 49±1.5, 51±3, and 55±0.6 MPa, respectively. Also, the crystallinity percentage of the manufactured samples under 220, 230, and 240 °C were 19.97%, 20.26%, and 20.51%, respectively. So, as it was revealed from the obtained results, by increase of the liquefier temperature, the crystallinity percentage was increased, slightly. Also, this (slight) increasing trend was observed in the obtained tensile strength by increase of the liquefier temperature in parallel with crystallinity increasing, in the Fused Filament Fabrication (FFF) process of the CF-PA6 composite. Also the increase of Young's modulus was observed with the increase of the liquefier temperature of FFF manufacturing of CF-PA6.

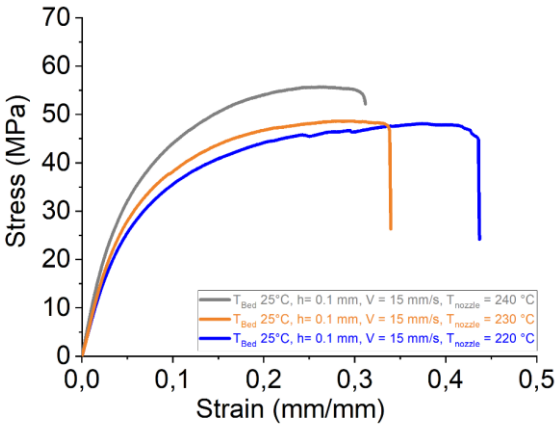

Fig. 78. Tensile behavior of printed CF-PA6 specimens under the various liquefier temperatures

The obtained crystallization degree of the manufactured PA6 samples corresponding to the stated different liquefier temperature values are tabulated in table 18.

	Conditions	T_c (°C)	T_m (°C)	%Crystallinity
No. 1	$T_{Liquefier}$ = 220 °C	174.83°C	204.51°C	12.51%
	$T_{Liquefier}$ = 230 °C	173.73°C	207.74°C	12.75%
	$T_{Liquefier}$ = 240 °C	174.02°C	207.82°C	14.40%

Table 18. The obtained values related to different properties from DSC curves of the printed PA6 samples

Fig. 79 illustrates the tensile behaviors of the printed PA6 specimens under the considered and stated liquefier temperature values. The maximum tensile strength of the printed specimens under the liquefier temperature of 230 °C, and 240 °C were 55.48±0.78, and 68.92±0.9 MPa, respectively. The manufactured sample made of PA6 under the liquefier temperature of 220 °C had the lowest strength. This weakness didn't let us even to cut the printed single wall samples to prepare the related tensile test specimen, because of the occurred fracture in the interface of the deposited layers during the cutting/punching process. Also, the crystallinity percentage of the manufactured samples under 220 °C, 230 °C, and 240 °C were 12.51%, 12.75%, and 14.40%, respectively.

So, as was found out from the obtained results, by increase of the liquefier temperature, the crystallinity percentage was increased, too. Also, this increasing trend was observed in the obtained tensile strength.

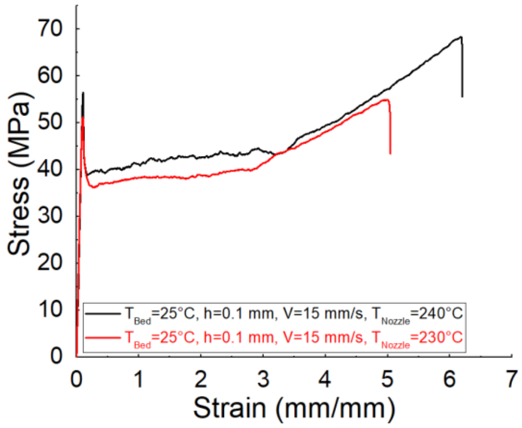

Fig. 79. Tensile behavior of printed PA6 specimens under the various liquefier temperatures

As it was observed, the crystallinity percentage of the manufactured CF-PA6 sample were more than correlated PA6 manufactured samples. In fact, the chopped carbon fibers in CF-PA6 had been the preferable crystalline nucleation sites. Also, the strength of the CF-PA6 sample from the printed single wall part, had lower strength in comparison with the ones made of PA6. Because, the rotation and sort of turbulent movement of chopped carbon fibers among the printing process when the matrix is liquid and even semi solid caused narrow sections in some sections of solidified raster (Fig. 80). The narrow sections appear because of the lack of enough fluidity of matrix and increase of the viscosity due to the existence of chopped carbon fibers. These sections were stress concentration zones which caused less strength of the prepared CF-PA6 samples from the printed single wall parts.

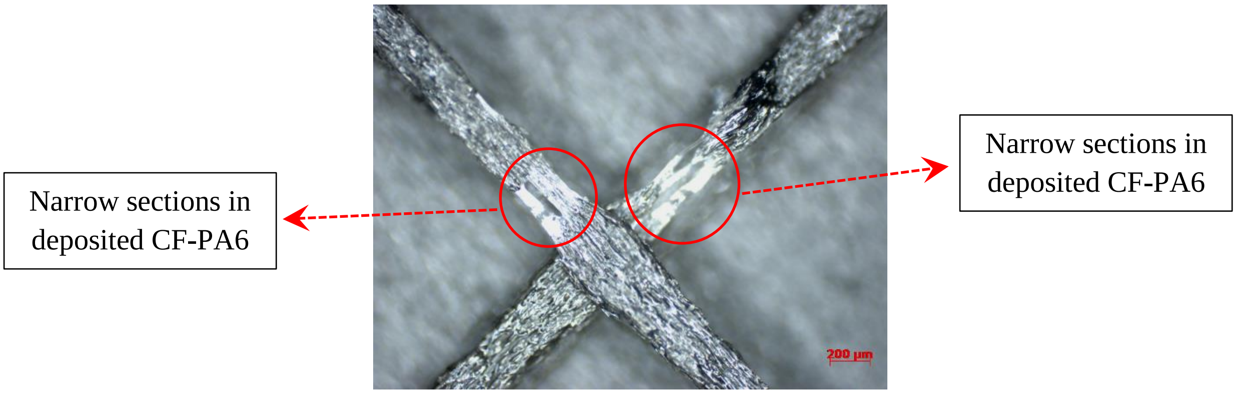

Fig. 80. Observed narrow sections in the deposited CF-PA6 raster

Also, scanning electron microscopy (SEM) observations of the CF-PA6 manufactured samples related to the liquefier temperature values of T_{liq}=240 ºC and T_{liq}=220 ºC were done and presented in Fig. 81.

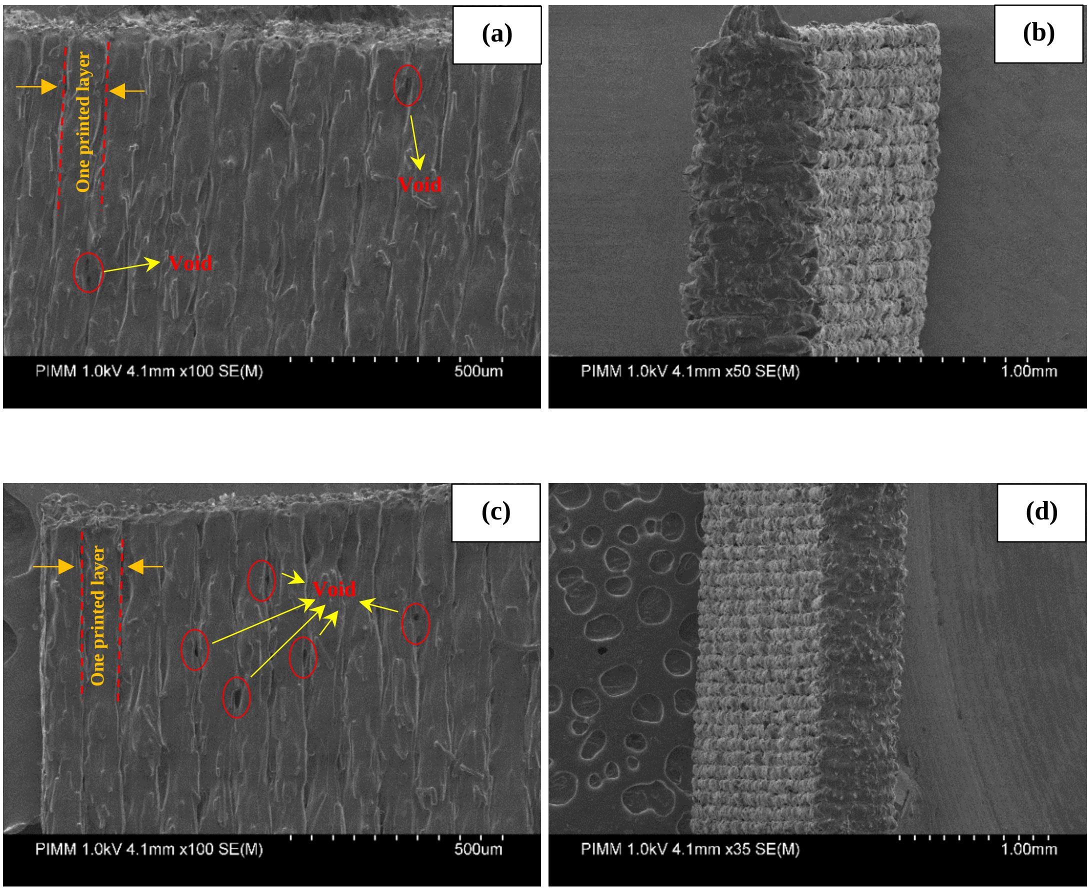

Fig. 81. SEM micrographs of manufactured CF-PA6 samples at T_{liq}= 240 ºC (a, b) T_{liq}= 220 ºC (c, d)

The existence of the micro voids between the printed layers, which caused the poor mechanical properties of the FFF manufactured specimens in comparison with the manufactured parts by conventional manufacturing methods are marked on the SEM photographs. The micro voids in the interface of the printed layers can originate from lower viscosity of PA6 and caused the poor adhesion and poor strength of the interface of the layers, which could be the local crack propagation location and subsequence fracture. In the captured SEM photographs, the micro voids were more sensible in the related micrograph to the printed specimen at the liquefier temperature value of 220 ℃ (less liquefier temperature).

4.2.2 Influence of print speed

The Influence of the print speed as one of the other process variables was studied. The importance of this parameter can be highlighted in terms of the production speed. For study the influence of the print speed, three different print speed values of 13 mm/s, 15 mm/s, and 17 mm/s were considered to print the required specimens. According to the obtained DSC curves of the CF-PA6 printed specimens from the used different print speed values (13 mm/s, 15 mm/s, and 17 mm/s), there is no noticeable change in the obtained degree of crystallinity values (Fig. 82, Table 19).

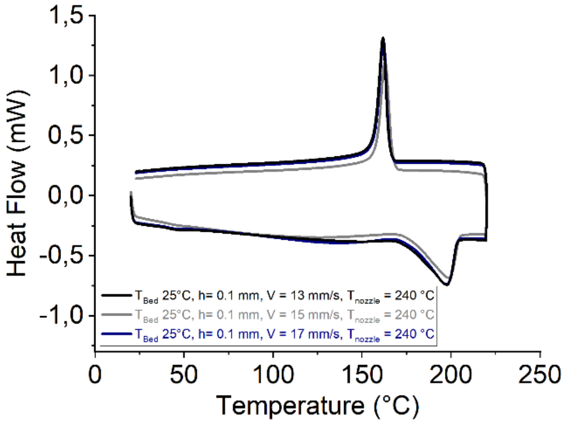

Fig. 82. Obtained DSC curves from CF-PA6 printed samples at different print speed

	Conditions	T_c (°C)	T_m (°C)	%Crystallinity
No. 2	V = 13 mm/s	161.68°C	197.71°C	20.77%
	V = 15 mm/s	162.82°C	198.72°C	20.51%
	V = 17 mm/s	161.94°C	197.60°C	20.64%

Table 19. The obtained values related to different properties from DSC curves of the CF-PA6 printed samples at the different print speeds

According to the applied tensile tests on the CF-PA6 printed specimens at the stated different print speed values, the tensile strength values of 65±0.5 MPa, 55±0.6 MPa, and 63±1.3 MPa were obtained related to the printed specimens at the print speed values of 13 mm/s, 15 mm/s, and 17 mm/s, respectively (Fig. 83). Also, the same evolution of Young's modulus (such as the tensile strength) was observed from the obtained tensile test results related to the prepared specimens at the stated print speed values. So, the tensile properties of the printed specimens at the print speed values of 13 mm/s and 17 mm/s were closer to each other in comparison with the obtained results related to manufactured samples at 15 mm/s. One can note that the degree of crystallinity of the printed sample with the print speed of 13 mm/s was slightly higher, which showed higher tensile strength, too. However, according to the SEM micrographs of the manufactured specimens at the print speed value of 13 mm/s, the micro voids at the interface of the printed layers were observed (Fig. 84) and the printed sample has not good dimensional accuracy. Due to the weak dimensional stability, it seems the printed sample with the print speed of 15 mm/s has the optimized process condition (Fig. 95).

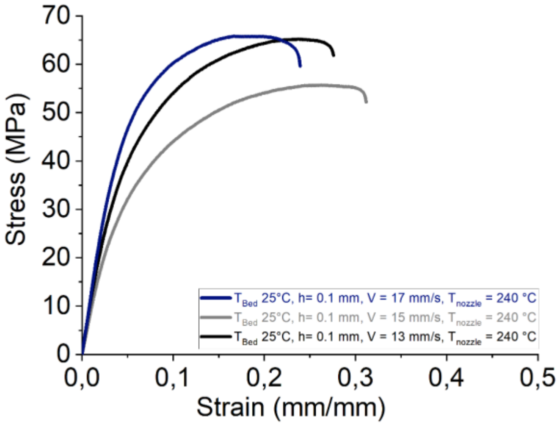

Fig. 83. Tensile behavior of CF-PA6 printed specimens at the different print speed values

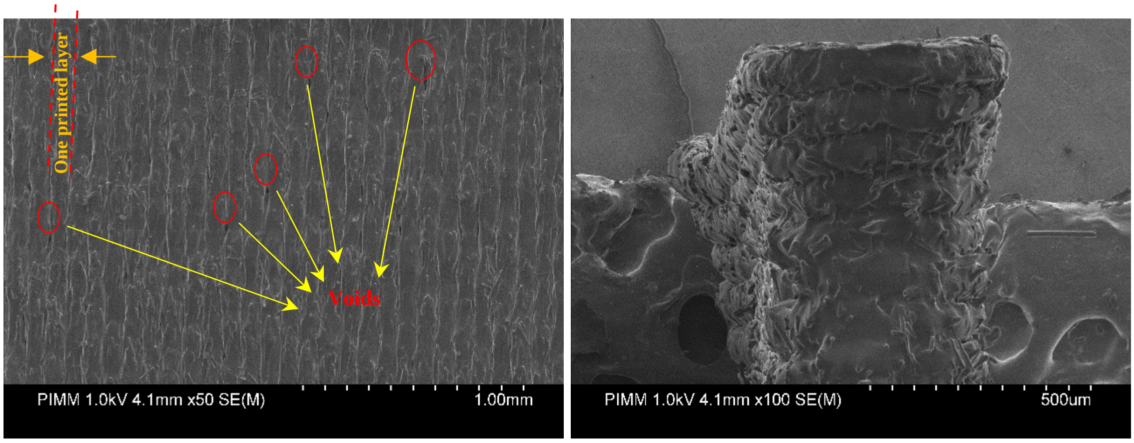

Fig. 84. SEM micrographs related to the CF-PA6 printed specimens at V = 13 mm/s

The obtained crystallization degree of the manufactured PA6 samples corresponding to the stated different print speed values are tabulated in table 20.

	Conditions	T_c (ºC)	T_m (ºC)	%Crystallinity
No. 2	V = 13 mm/s	169.98°C	206.80°C	15.46%
	V = 15 mm/s	174.02°C	207.82°C	14.44%
	V = 17 mm/s	170.17°C	206.71°C	15.67%

Table 20. The obtained values related to different properties from DSC curves of the PA6 printed samples at the different print speeds

Also, according to the applied tensile tests on the PA6 printed specimens at the stated different print speed values, the tensile strength values of 57.78±0.84 MPa, 68.92±0.9 MPa, and 66.84±3.71 MPa were obtained related to the printed specimens at the print speed of 13 mm/s, 15 mm/s, and 17 mm/s, respectively. By considering the STDEV values, the strength of the manufactured PA6 samples by print speed values of 15 mm/s, and 17 mm/s were so close. So, as for general observation it was found out that by increase of the print speed, the strength was increased, too.

<u>- Effect of fiber presence on temperature profile of the deposited filaments:</u>

To analyze this phenomenon, in-situ temperature measurements of the manufactured CF-PA6 for different print speeds of 13 mm/s, 15 mm/s, and 17 mm/s are presented in Fig. 85. The results exhibit that by an increase of the printing speed, the temperature evolution of the first printed layer remains above the crystallization temperature in the printed specimens with the three considered printing speed values. The same was observed in the obtained curve from in-situ temperature measurements of the manufactured PA6 parts Fig. 86. One can note that the print speed enhancement modifies the rearrangement of polymer chains and the consequently obtained degree of crystallinity by decreasing the cooling time. The latter can be the reason for the poor dimensional stability.

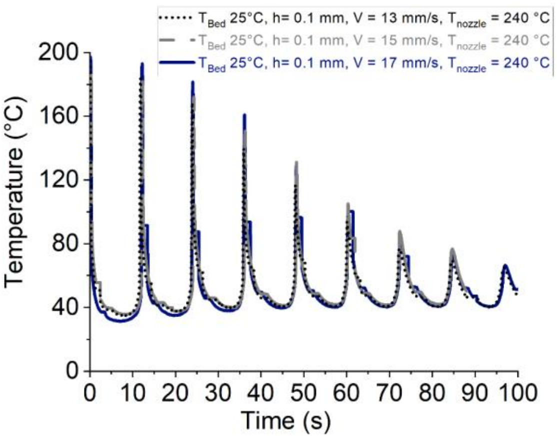

Fig. 85. In-situ temperature measurement for different print speed (CF-PA6)

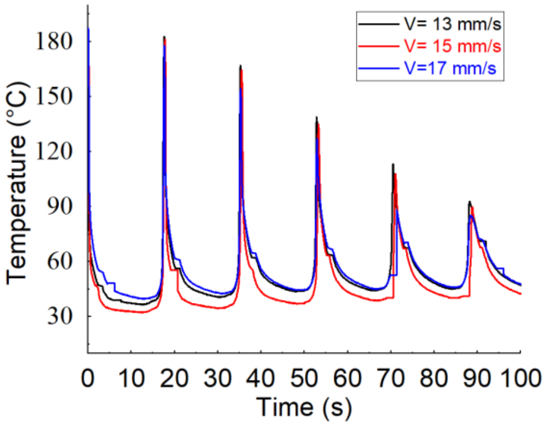

Fig. 86. In-situ temperature measurement for different print speed (PA6)

According to Fig. 87, the obtained Time-Temperature curve related to printed samples made of PA6 and CF-PA6 under the print speed of 15 mm/s, had almost the same Temperature-Time curve. This evolution can confirm that the presence of the chopped carbon fibers has no significant effect on the Time-Temperature curve of the deposited filaments in the considered process parameters. The later could help to optimize the process manufacturing.

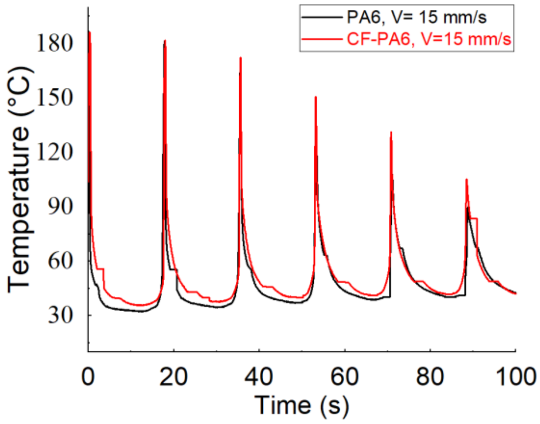

Fig. 87. In-situ temperature measurement of manufactured PA6 and CF-PA6 samples at the print speed 15 mm/s

4.2.3 Influence of layer height

The effect of the layer height as one of the process parameters was studied in the Fused Filament Fabrication (FFF) process of CF-PA6. Printing process was set on three different values of 0.1 mm, 0.2 mm and 0.3 mm as three different layer height values for studying the impact of this process parameter on the mechanical behavior of the obtained specimens. According to the obtained tensile test results, the printed specimens with the selected layer height values of 0.1 mm, 0.2 mm, and 0.3 mm have tensile strength of 55±0.6 MPa, 49±2.5 MPa, and 56±2.5 MPa, respectively (Fig. 88). Also, the crystallinity percentage values of 20.51, 19.27, and 21.22 were obtained related to the printed specimens with the layer height of 0.1 mm, 0.2 mm, and 0.3 mm, respectively (table 21).

For more analyzing, in-situ temperature measurements of the manufactured CF-PA6 for different layer height values of 0.1 mm, 0.2 mm, and 0.3 mm are presented in Fig. 89.

According to the stated results, it is proposing that there are two competitive factors in terms of the mechanical behavior of the manufactured samples by the FFF process of CF-PA6 with the different layer height (the stated layer height values). The two factors which compete with each other by increase of the layer height were (i) decrease of the liquidity (or fluidity) of the printed layers, and (ii) increase of retained temperature in the printed layers. The effect of the decrease of the liquidity (or fluidity) has overcome the second competitive factor in the obtained samples by changing the layer height from 0.1 mm to 0.2 mm in the FFF process of CF-PA6. Which caused the decrease of the adhesion and bonding of the printed layer and consequent tensile strength of the printed samples with the layer height of 0.2 mm in comparison with printed ones related to the layer height of 0.1 mm. The stated increase of the fluidity has been concluded from the observed peaks obtained from the temperature evolution (Time-Temperature) curves, in which the recorded maximum temperature value of each printed layer with layer height of 0.1 mm was more as comparing with the deposited layer with the height of 0.2 mm (Fig. 90). Fig.90 is related to the peaks of the fourth CF-PA6 deposit layers with height of 0.1 mm and 0.2 mm related to the obtained Time-Temperature curve from In-situ temperature measurement.

Also, the crystallinity percentage was decreased a bit by the increase of the layer height from 0.1 mm to 0.2 mm. While it is proposed that the effect of the increased retained temperature in the printed layers has overcome the first competitive factor, in the case of the FFF process of CF-PA6 with the layer height 0.3 mm. According to the Time-Temperature curve (the bottom of the curves) related to the printed layer height of 0.3 mm (Fig. 91) one can be observed that more temperature value, which can cause the polymer chains rearrangement and the consequent increase of the mechanical behavior, due to the crystallinity percentage increment.

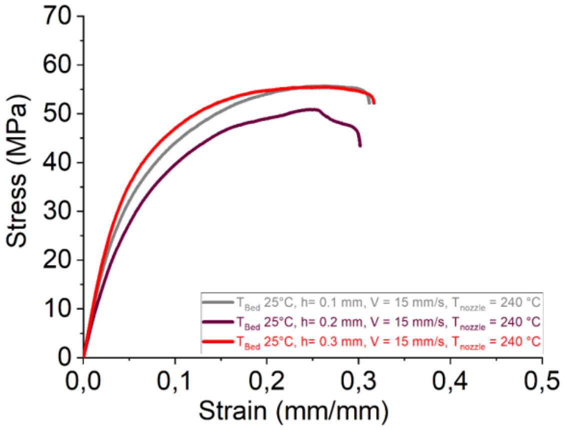

Fig. 88. Tensile behavior of the printed specimens with the various layer height

Conditions		T_c (°C)	T_m (°C)	%Crystallinity
No. 3	h = 0.1 mm	162.82°C	198.72°C	20.51%
	h = 0.2 mm	161.50°C	197.79°C	19.27%
	h = 0.3 mm	161.68°C	197.48°C	21.22%

Table 21. Obtained different properties from DSC curves with the various layer height

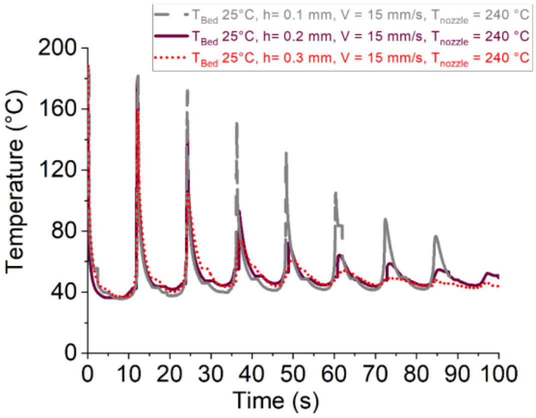

Fig. 89. In-situ temperature measurement of the printed specimens with the various layer heights

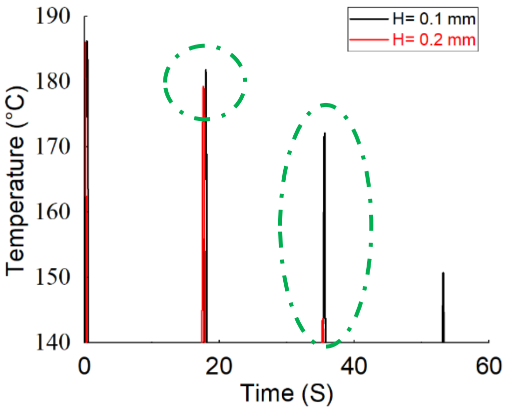

Fig. 90. Peaks of the fourth CF-PA6 deposit layers with height of 0.1 mm and 0.2 mm obtained from In-situ temperature measurement

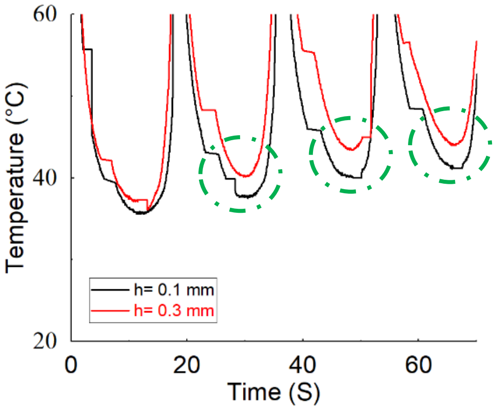

Fig. 91. Bottom of the fourth CF-PA6 deposit layers with height of 0.1 mm and 0.3 mm obtained from In-situ temperature measurement

The obtained crystallization degree of the manufactured PA6 samples related to 0.1 mm, 0.2 mm, and 0.3 mm were 14.4%, 15.31%, and 15.69%, respectively. The tensile strength of manufactured PA6 samples with layer height of 0.1 mm and 0.2 were 68.92±0.9 MPa and 72.57±0.8 MPa, respectively. So, by considering the increase in the strength of manufactured PA6 samples by increase of layer height from 0.1 mm to 0.2 mm, it was found out that the decrease of the liquidity (or fluidity) factor wasn't sensible in case of PA6 samples. Therefore, the decrease of the liquidity (or fluidity) factor can be also due to existence of chopped carbon fibers which are solid components in the liquid/semi-liquid polymer matrix components of composite material during the FFF process.

From these results, it seems that the printed composite specimens with layer height of 0.1 mm (as reference sample) could be the optimal process parameter. Also, according to Durga et al [87], in the case of reinforced PLA by carbon fiber, it is stated the highest tensile strength observed in the sample with the minimum layer thickness (0.1 mm).

4.2.4 Influence of bed temperature

The effect of bed temperature was analyzed at different temperature values 25 °C, 45 °C, 60 °C, and 80 °C. One can note that generally, PA6 has relatively low viscosity and by increasing the bed temperature the risk of lack of dimensional stability can occur. Fig. 92 presents the SEM micrographs related to the CF-PA6 printed specimen at bed temperature of 80 °C. One can observe that the layers were more deformed compared to the SEM micrographs of the printed sample at bed temperature of 25 °C (Fig. 81). Moreover, there are more voids in this case.

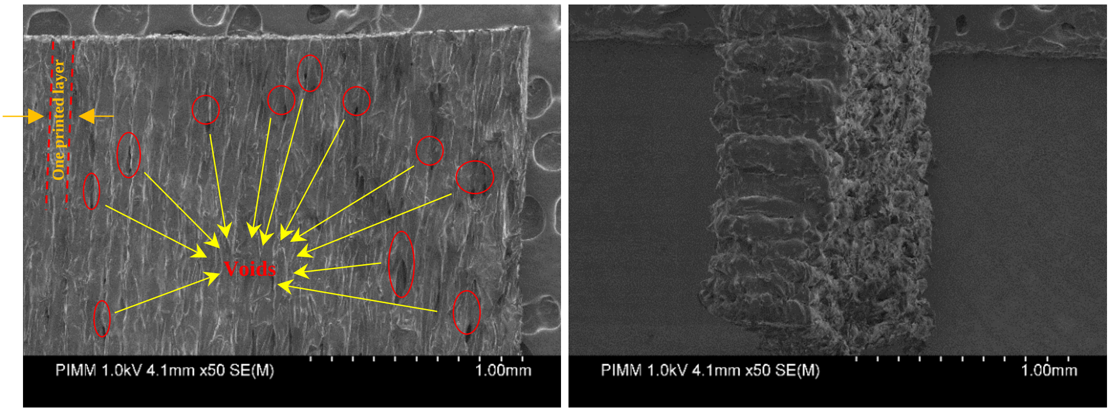

Fig. 92. SEM micrographs related to the CF-PA6printed specimen at bed temperature of 80°C

Fig. 93 presents the in-situ temperature measurement of the CF-PA6 printed specimens with the various bed temperatures. For all printed specimens with the aforementioned different bed temperatures, after the first layer deposition, the temperature reaches lower than crystallization temperature. However, at bed temperature of 80°C this value was near to the crystallization temperature compared to other samples related to the other bed temperatures values, but the problem of dimensional stability was existed.

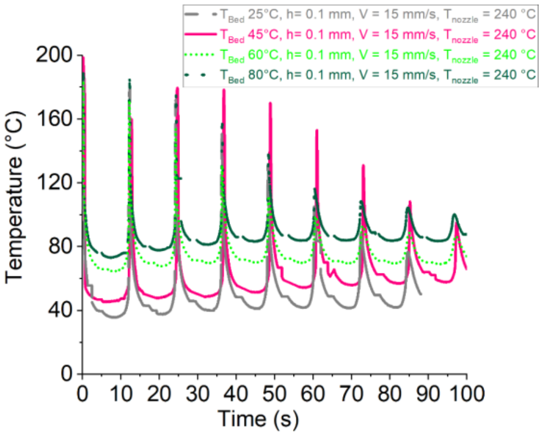

Fig. 93. In-situ temperature measurement of the printed specimens with the various bed temperatures

4.2.5 Microstructure analysis related to the printed specimens

Fig. 94 presents the microstructure observations of the manufactured CF-PA6 specimens (10 deposited filaments) for reference condition. The aim was to understand the contact surface of two adjacent layers. The results showed that as the distance from the bottom layer had been increased (lower layers to higher layers), the contact surface area of the adjacent layers was decreased. Because of the stated temperature evolution of the deposited layers, it is observable that after 2 or 3 sequences of deposition, the temperature dropped below the crystallization temperature. This fact contributes to the rate of cooling, solidified material, less material diffusion and then decrease the contact surface among two adjacent deposited layers.

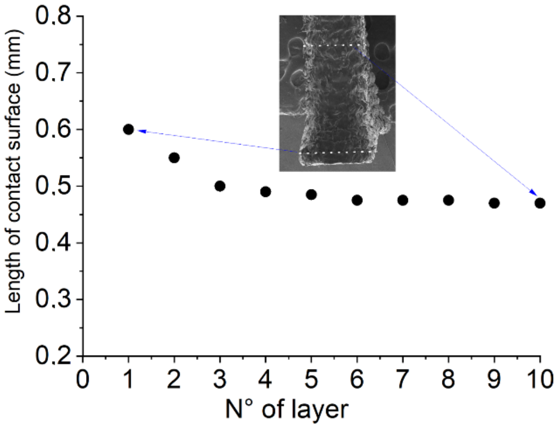

Fig. 94. Analysis of the length of contact between two adjacent filaments in manufactured CF-PA6 samples (the reference sample)

In comparison with the reference sample, each condition prepared its effect on the final feature and microstructure of the manufactured parts. According to the aforementioned observations, the same evaluation was applied on the deposited layers (Fig. 95) to evaluate the contact surface of each two adjacent filaments to be able to compare against each other. This analysis is beneficial to summarize the impact of each process parameter on the bonding and quality of manufactured parts. One can note that the reference sample has a more stable contact surface at first 10 printed layers. This analysis confirms that the reference sample (with printing condition of: liquefier temperature: 240°C, print speed: 15 mm/s, layer height: 0.1 mm, and platform temperature: 25°C) produced by the best and optimal process parameter.

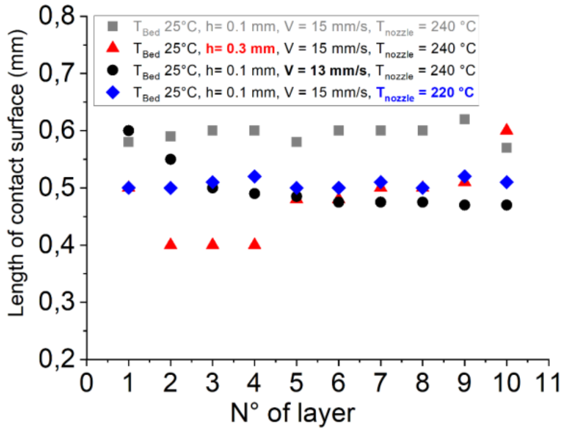

Fig. 95. Comparing the contact length between two adjacent layer in each condition of CF-PA6 printing process

4.3 Thermal properties and rheological analysis: Time-Temperature-Transformation diagram

During the FFF process, the thermal properties, and the rheological properties of the utilized polymers (also the matrix of the polymer-based composites) have the essential and significant role. The adhesion of the deposited layers in the final manufactured part is depended on this role. So, because of the stated reason we focused on temperature and its effect on the viscosity of the polymer and the matrix component of the utilized composite material, in this study (Fig. 96).

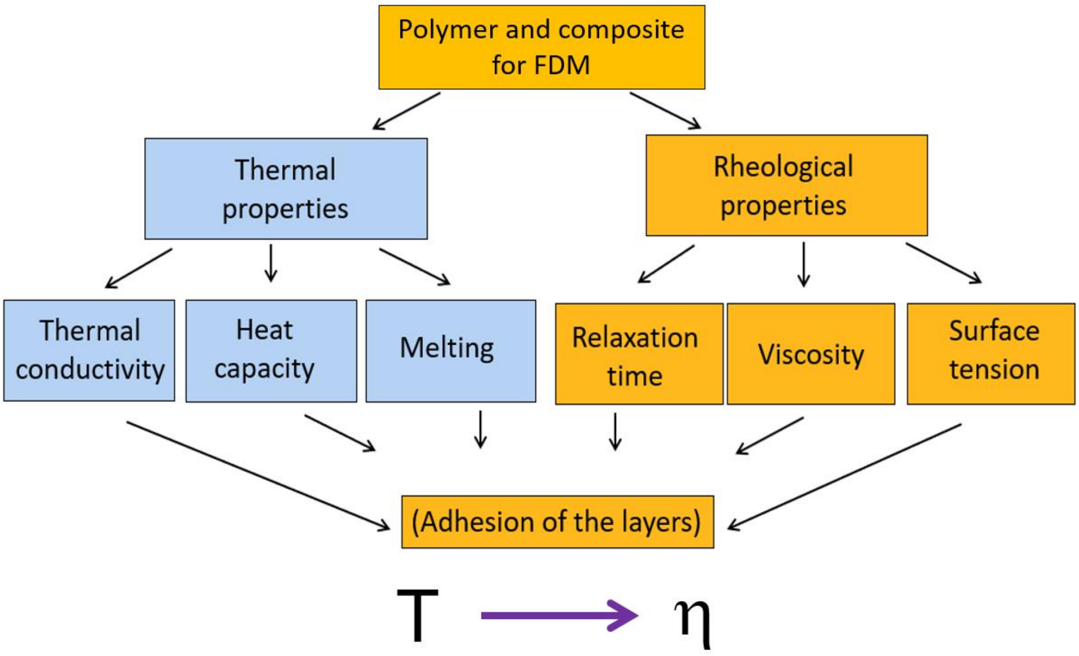

Fig. 96. General view of the FDM process of polymer and composite materials and the obtained adhesion of the deposited layers

In FDM/FFF process, a thermoplastic polymer is fed into a liquefier that extrudes a filament while moving in successive X-Y planes along the Z direction, to fabricate a 3D part layer-by-layer. Consequently, as the deposition progresses, the hot filament is deposited onto filaments that were previously deposited and also are situated in the cooling process. This causes the re-heating of the previous deposited layers/filaments during the manufacturing process. A period of time is defined in which the temperature of the interfaces of the contacted layer/filaments is above the glass transition temperature (T_g) in the case of amorphous materials, or above the crystallization temperature (T_c) in the case of semi-crystalline materials. Considering this period of time is necessary, because the proper bonding occurs during this period. Therefore, each deposited filament should be sufficiently hot during deposition, but not too hot, to avert deformation due to gravity and the weight of the deposited filaments in the subsequent layers. Fig. 97 presents the thermal properties of the used PA6.

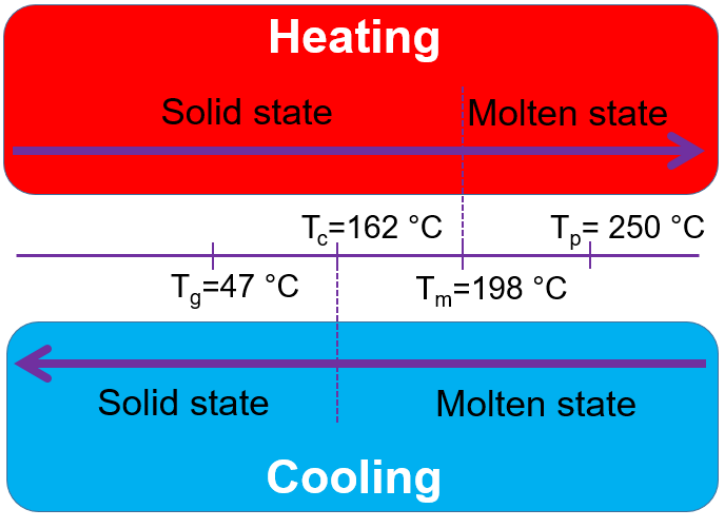

Fig. 97. The thermal properties of the used CF-PA6

Several researches performed on thermal history prediction of filaments while deposited. Bellehumeur et al**.** [88] proposed the Lumped capacity model by assuming uniform temperature profile of filament’s cross-section. This 2D analysis was then simplified to a 1D transient heat transfer model, so the cooling process was simplified into a 1D heat transfer model. Despite the simplification proposed in this approach, the simulation does not contribute to the complex geometries. Taking into account the contacts between filaments, Costa et al. [89] suggested an analytical solution for the transient heat transfer during the deposition of filaments. Although they have neglected the axial and radial heat conduction, they have recently distinguished the contribution of various thermal phenomena engaged in the process [90]. The main disadvantage of their approaches is the limitation of experimental validations and the distance exists between the obtained results with reality. Thomas and Rodriguez [91] have also presented a 2D thermal model in a specific shape of deposition. In this work, the conduction and any contact resistance of filaments have been neglected. Moreover, Yardimici et al. [92, 93] proposed a 1D thermal model in their works by taking into account the thermal interaction with the environment and between the deposited filaments. Zhang et al. [94] developed a FEM, applying element activation, to simulate the thermomechanical characterization in FDM/FFF. A 3D transient thermal FEM developed by Ji et al. [95] considering the thermal conduction and heat capacity. The weakness of all analytic approaches is that simplified closed-form solutions are limited to simple geometry and could not be applied to realistic parts and manufacturing processes.

After a decade and by expiration of the Stratasys FDM^{TM} in 2010, the number of works on 3D printing have progressively raised up. The main reason relies on the emersion of open-source 3D printers and thus the possibility of working on different possible aspects of optimization purposes. Peng et al.

In addition, Seppala and Migler [96] used an IR-camera to study the temperature distribution around the active printing area. In other similar work, D'Amico and Peterson [97] applied a finite element analysis for simulation of the heat transfer during FDM/FFF process. In both work, using an IR-camera, they contributed a temperature profile of the external surface of the printed objects and thus the simulations were validated based on the mentioned results.

More recently, Costa et al. Developed a heat transfer model including the transient heat conduction between the filament and/or the built platform [89, 98]. As illustrated in Fig. 98, they found that temperature profile of filaments is highly affected by the physical contact exist between the filaments. Accordingly, they considered the involved parameters during their experimental validation and the results, however, obtained by implementing an IR-camera, show that the contacts between filaments play a crucial role and should be considered in heat transfer investigations.

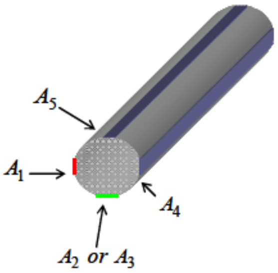

Fig. 98. Possible contact areas of one filament. A1, A3, A4, A5 , areas of contacts 1,3,4,5 with adjacent filaments; A2 area of contact 2 with the supporting table [96]

In FFF/FDM, based on the matter of heating the material during printing, the selection of liquefier temperature is an important issue. The point is to prevent overheating or even low flowability of material during deposition. Therefore, realization of the rheological characteristics is crucial. Certifying optimum material feeding as well as rapid changing in the viscosity, printed material should show sufficient increase in its viscosity while extruding to avert instability of geometry of the 3D printed final parts.

So, this is the reason why thermoplastic polymers are being used with an outstanding viscoelastic behavior while encountered with cyclic temperature profile during 3D printing [99]. To describe shear-thinning, rheological characteristics such as viscosity should be taken into consideration. Besides, there are two main parameters, storage modulus and loss modulus, determining the viscoelastic behavior of the material. The appropriate relative balance in between these two important factors specifies the solidity or liquidity of the material during the process. Despite the fact that the viscosity decreases drastically while melted and the material subjects to a high shear rate (depending on the liquefier diameter), even a greater decrease in the material viscosity is afforded [100]. Conversely, after extrusion of the material, the sudden drop in temperature results in the massive increase in the material viscosity [101]. These variations and transformations play an important role during FDM/FFF process. Given the above-mentioned explanations, controlling the viscosity variation further with the temperature profile between the deposited and previously deposited layer is an important issue to give sufficient time for proper diffusion and bonding. These are key factors to retain the temperature in a specified zone based on the type of material [96]. They thus imitate the material diffusion and welding process between two adjacent layers and categorized as a thermally driven phenomenon named ‘Coalescence’.

Regardless of study on the influence of parameters on neck-growth or neck-growth prediction by viscoelastic models, there is still a lack of practical knowledge on consideration of temperature dependent viscosity and its influence on coalescence of two adjacent filaments. To eliminate the mentioned missing spot, a thermo-mechanical approach is an essential manner by applying the results of temperature evolution of filaments at their interface.

The evolution of viscosity as a function of time and temperature by the following two methods have been determined:

- By rheometer, in the **molten state**
- By DMTA, in the **Rubbery state**

Rheometry tests were performed at varying shear rates in isotherm regime. Several tests were carried out at different temperatures. Using DMTA, multi-frequency testing from 1 Hz to 30 Hz was performed.

4.3.1 Viscosity measurement at molten state

As the temperature evolution during the cooling stage (and thus the re-heating peaks) of filaments plays an important role in determination of the filament bonding, the correlation of rheological characteristic along with the mechanical properties is a key point. So, simultaneous characterization of thermal and rheological properties is inevitable. Regarding the mechanism of deposition and temperature profile of each layer, viscosity varies accordingly. In general, following observations could be concluded:

- Lower cooling rate limits the viscosity enhancement; favorable flowability of the material.
- By cooling of the deposited filament from a temperature of the extruder to the ambient temperature, the viscosity varies depending on the deposition conditions.
- Viscosity tends to unlimited values depending on the filament’s temperature evolution.

One benefit of temperature dependence viscosity consideration in FDM/FFF process is that it enables us to have more precise investigations of rheological characteristics. This issue could be more highlighted while considering the interaction of involved parameters through them. This is a potential concern by which engaged researchers in the study of bonding and mechanical strength.

We have considered the evolution of viscosity and temperature simultaneously, so far. The temperature dependence viscosity was considered to vary from the liquefier temperature to the ambient temperature using Arrhenius equation by implementing the temperature evolution in it. The obtained curves from viscosity measurements of PA6 and CF-PA6 are presented below Fig. 99 and Fig. 100.

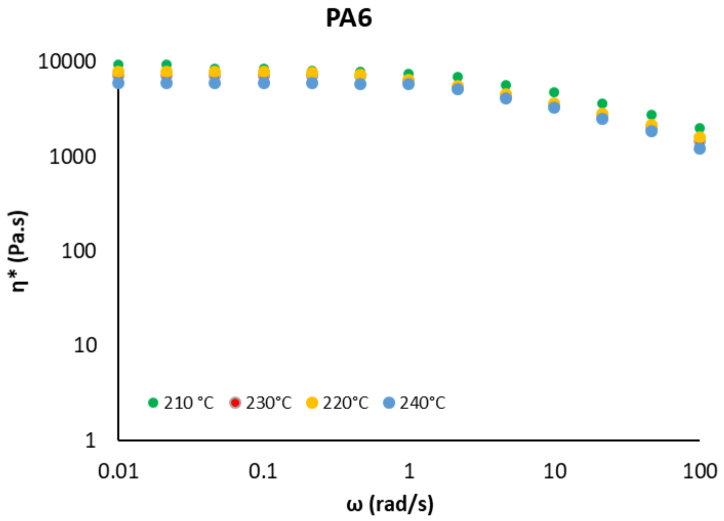

Fig. 99. Viscosity evolution in different temperature related to PA6

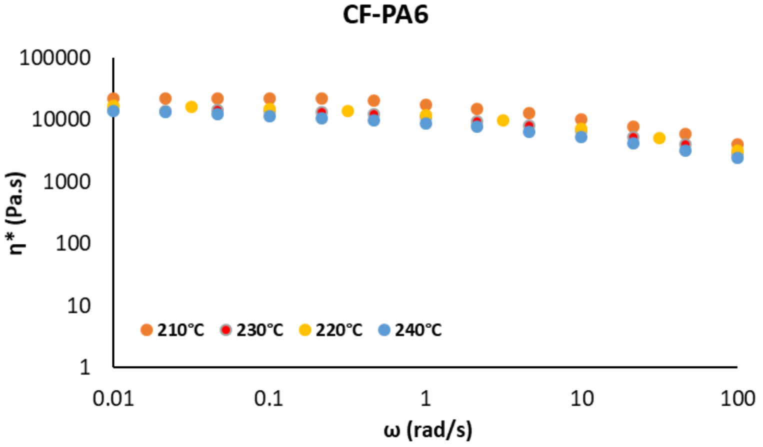

Fig. 100. Viscosity evolution in different temperature related to CF-PA6

The viscosity variation in melt state as a function of temperature obeys Arrhenius law (Equation 4.1). As for showing the validity of this law for the PA6 and CF-PA6 in the molten state, we determined the Newtonian viscosity of stated materials at different temperatures by performing isothermal tests. According to this equation, by plotting $\ln \eta$ as a function of ${}^{1}/_{T}$, we will obtain the following equation that is a linear function:

$$\ln \eta = \ln \eta_0 + \left(\frac{E}{R}\right) \times \frac{1}{T} \qquad (4.1)$$

Fig. 101 clearly demonstrates the measured value for viscosity at different temperature and isotherm state, related to PA6 and CF-PA6. The values could be fit to the mentioned equation and the related curve, which means that the constants of this law, E and η_0 for PA6, are 30,36 kJ and 4.93 Pa.s, respectively. Also, the constants of this law, E andη_0 for CF-PA6, are 42,93 kJ and 0.5 Pa.s, respectively

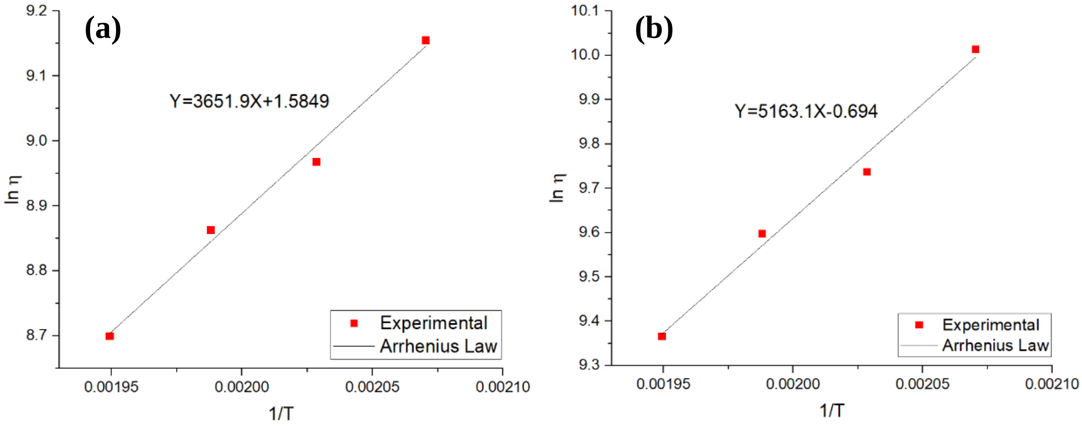

Fig. 101. Ln (η) versus 1/T related to (a) PA6 and (b) CF-PA6

4.3.2 Viscosity measurement at solid state

<u>Influence of temperature on viscoelastic properties</u>

Consequently, to explore the influence of temperature on viscoelastic properties of PA6 and CF-PA6, multi-frequencies DMA test was implemented in flexural bending mode. The obtained curves related to CF-PA6 are presented below as Fig. 102.

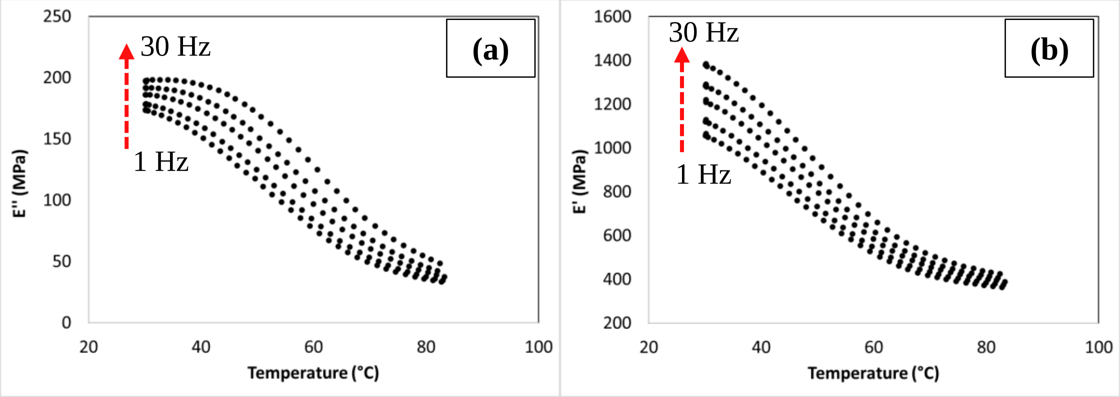

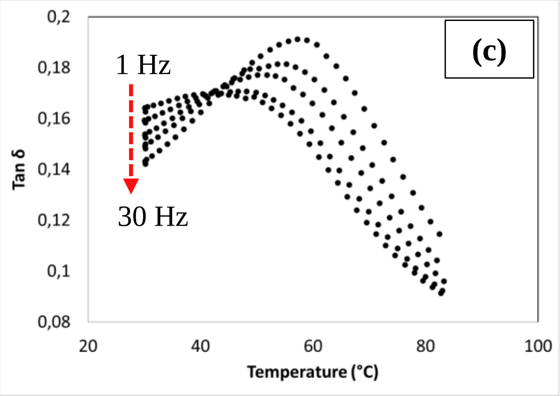

Fig. 102. DMTA test result: Evolution of the (a) loss moduli, (b) storage moduli, and (c) loss factor versus temperature for CF-PA6

The evolution of viscosity could be calculate using Williams-Landel-Ferry (WLF) equation:

$$Log\ a_T = \frac{-C_1(T - T_r)}{C_2 + (T - T_r)} \tag{4.2}$$

Where a_T is WLF shift factor, C_1 and C_2 are empirical constants adjusted to fit the values of superposition parameter a_T, T is the temperature, and T_r is the reference temperature at reference frequency.

Using linear regression method, WLF equation could be transformed to the following equation:

$$\frac{1}{Log\ a_T} = \frac{-C_2}{C_1}\frac{1}{T - T_r} + \frac{1}{C_1} \tag{4.3}$$

Then, $\frac{1}{Log\ a_T}$ was plotted versus $\frac{1}{T-T_r}$. The fitted curves are shown in Fig. 103 (R^2=0.9869 related to PA6 and R^2=0.9993 related to CF-PA6). The value of C_1 and C_2 are then calculated using the obtained results.

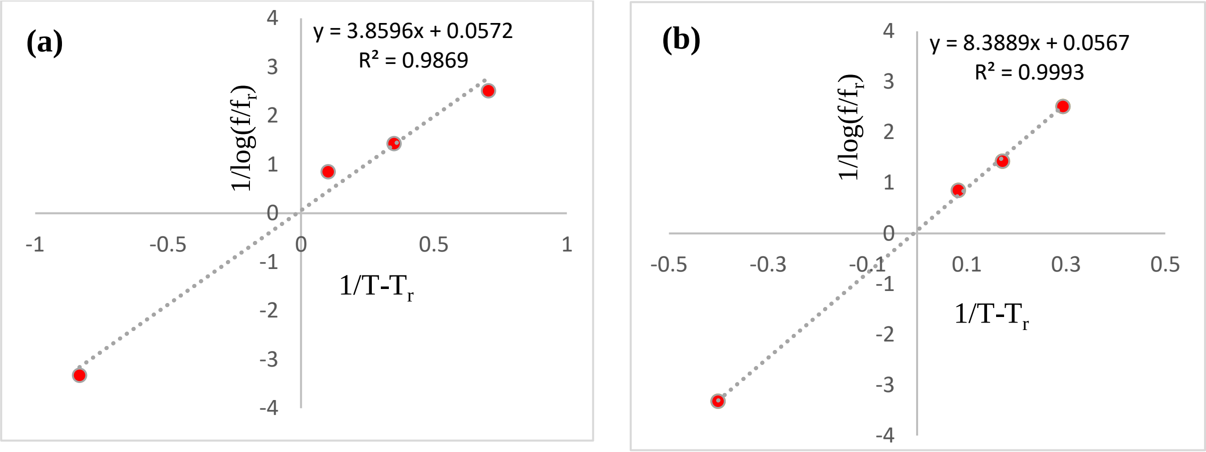

Fig. 103. Linear regression of WLF equation related to (a) PA6 and (b) CF-PA6

4.3.3 Time-Temperature-Transformation diagram

The main characteristic of the presented approach is the possibility of obtaining the Time-Temperature-Transformation diagram of a material during deposition and apply the findings in optimization procedures. It has been shown that viscosity is affected by the cyclic temperature profile that exists in FDM/FFF process, which could determine the features of final products. Its variation through the consecutive deposition of layers has been presented. Furthermore, a parametric study on the influence of process parameters upon viscosity evolution has also been performed. The influence of print speed and platform temperature on the evolution of viscosity indicate that the effect of process parameters is inevitable, and interaction of parameters should be taken into account.

A zoom of the processability areas of PA6 and CF-PA6 in FDM, show that the zone of processability is approximately between 240°C and 162°C (CF-PA6) / 173°C (PA6) during cooling down. In addition, viscosity raised suddenly from 650 Pa.s to 104 Pa.s during this cooling stage, (Fig. 104).

As a result, the variation in viscosity as a function of temperature can be modeled over a wide temperature range. Also, the influence of cyclic temperature profile on viscoelastic behavior of the material using WLF equation indicated that the viscosity variation in solid state plays an important role on the rheological characteristic of the material. Results presented here may help researchers to improve the quality of constructed parts in FDM/FFF and consequently ameliorate their strength.

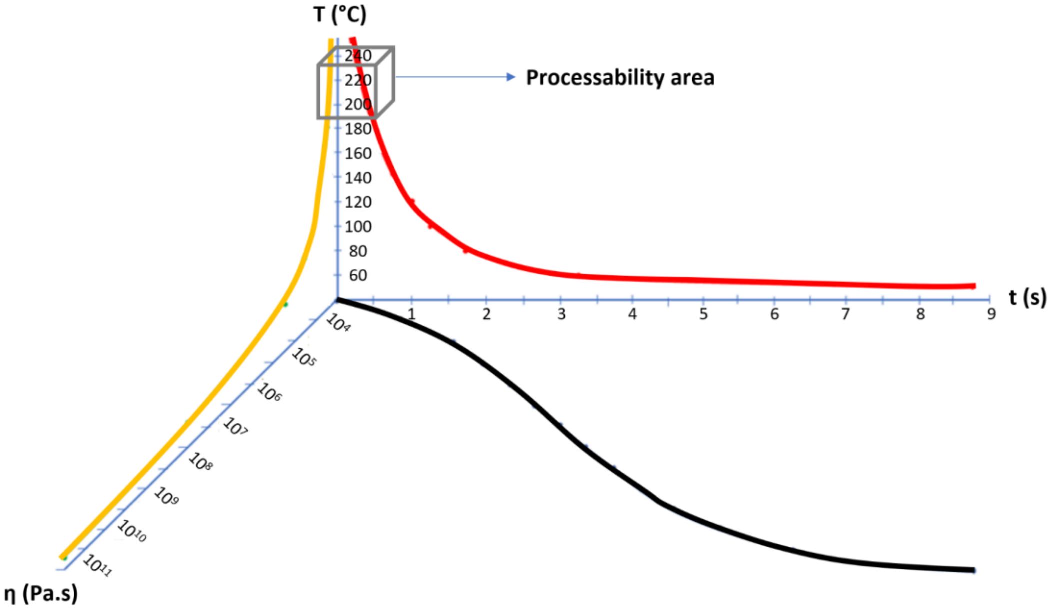

Fig. 104. Time-Temperature-Transformation diagram: PA6 and CF-PA6

4.4 Mechanical characterizations

An investigation for the impact of some important FFF process parameters of polymer-based composites on the inter-layer adhesion (bonding) of the deposited filaments have been performed. It was proved that temperature profile evaluation of printed layers has a significant effect on the bonding of adjacent filaments. The presented approach was the possibility of obtaining the Time-Temperature-Transformation diagram of a material during deposition and apply the findings in optimization procedures. Failure stress/strain can be the indicators to figure out the mechanical properties of FFF manufactured products. In this section using optimized process parameters (liquefier temperature: 240°C, print speed: 15 mm/s, layer height: 0.1 mm, platform temperature: 25°C), the mechanical properties of the fabricated parts under monotonic and fatigue loadings have been analyzed.

4.4.1 Quasi-static tensile behavior

4.4.1.1 Effect of infill patterns

Three main infill patterns which were Triangular, Rectangular, and Hexagonal were considered to print the tensile specimens, by Mark Two printer. So, the tensile samples were printed by use of the CF-PA6 filament under the stated main infill patterns. Their tensile strength was compared with each other and also with the solid infill pattern (whose infill percentage was 100%). So, the tensile strength was considered as the criterion to make the comparison. The Tensile test results of the different infill pattern samples, which were made of CF-PA6 are listed in Fig. 105 and table 22.

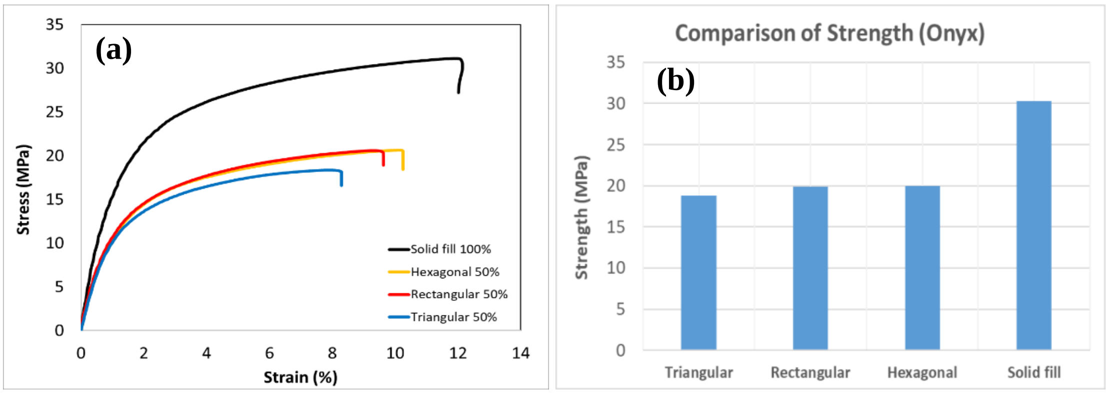

Fig. 105. Quasi-static tensile curves (a) and strength evolution (b)

According to the tensile test results of the printed samples by the use of CF-PA6, the tensile strength values of Triangular, Rectangular, Hexagonal, and solid infill were 18.79±1.19, 19.84±1.66, 19.99±1.32, and 30.31±5.5 (MPa), respectively. The tensile strength of the manufactured specimens with Triangular, Rectangular, and Hexagonal patterns were close to each other. However, the highest tensile strength is related to the solid infill samples. As it was extracted from the results, by changing the fill pattern of the printed CF-PA6 samples from triangular to rectangular and hexagonal, the tensile strength has been improved 5.9% and 6.4%, respectively. While by changing the infill pattern of the printing process of the samples which were made of CF-PA6, from the triangular to solid infill, the tensile strength improved almost 61.3% (Fig. 105). As it was observed from Fig. 106, the fracture surface of the solid samples was more brittle and more homogenous, in comparison with other samples.

Triangular infill pattern samples, made of CF-PA6					
SAMPLE	E (MPa)	σ_{max} (MPa)	ε_{max}	σ_y	ε_y
1	15	20.25	8.3	5.2	0.31
2	16	19.10	8.2	4.8	0.33
3	15	18.4	8	4.1	0.3
4	15	17.41	7	5.9	0.4
AVERAGE	15.25	18.79	7.87	5	0.34
STDEV	0.5	1.19	0.59	0.75	0.04
Rectangular infill pattern samples, made of CF-PA6					

SAMPLE	E (MPa)	σ_{max} (MPa)	ε_{max}	σ_y	ε_y
1	13	18.8	9.7	4.4	0.36
2	18	21.8	8.9	5.9	0.33
3	17	18.17	10.53	3	0.2
4	17	20.6	9.30	4.7	0.3
AVERAGE	16.25	19.84	9.61	4.5	0.3
STDEV	2.22	1.66	0.7	1.19	0.07
Hexagonal infill pattern samples, made of CF-PA6					
SAMPLE	E (MPa)	σ_{max} (MPa)	ε_{max}	σ_y	ε_y
1	13	16.85	8.3	5.2	0.31
2	15	20.06	8.2	4.8	0.33
3	15	20.67	8	4.1	0.3
4	16	22.41	7	5.9	0.4
AVERAGE	14.75	19.99	7.88	5	0.34
STDEV	1.26	2.32	0.6	0.75	0.05
Solid infill samples, made of CF-PA6					
SAMPLE	E (MPa)	σ_{max} (MPa)	ε_{max}	σ_y	ε_y
1	23	31.15	11.94	7.7	0.36
2	18	24.1	10.8	5.41	0.32
3	24	37.3	11.8	10.76	0.42
4	21	28.7	12.8	5.15	0.26
AVERAGE	21.5	30.31	11.84	7.26	0.34
STDEV	2.65	5.5	0.82	2.6	0.07

Table 22. Tensile test results of the printed samples under the different infill patterns, made of CF-PA6

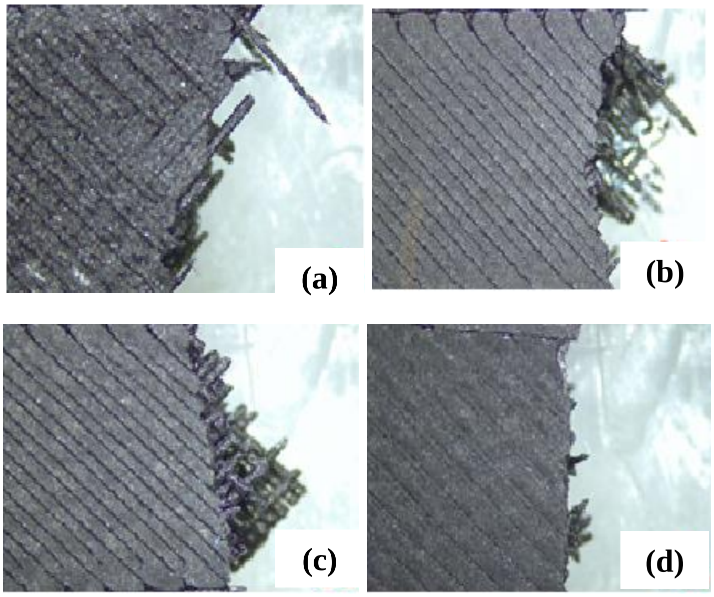

Fig. 106. Macroscopic observation after quasi-static tensile test,
(a) Hexagonal, (b) Triangular, (c) Rectangular, and (d) Solid infill

4.4.1.2 Effect of the continuous reinforcement on different infill patterns

The Tensile samples were printed by use of the CF-PA6 filament and continuous glass fiber, under the main stated infill patterns. Again, their tensile strength was compared with each other and also with the solid infill pattern (whose infill percentage was 100%). So, the tensile strength was considered as the criterion to make the comparison. The tensile test results of the different infill pattern samples, which were made of CF-PA6 reinforced with continuous glass fiber, are in Fig. 107. According to the tensile test results of the printed samples by use of CF-PA6 reinforced continuous glass fiber, the tensile strength of Hexagonal, Rectangular, Triangular and solid infill were 60.04±4.16, 66.7±2.63, 69.6±3.05, and 78.35±0.87 (MPa), respectively. So, as is clear, the tensile strength of the Hexagonal specimens is the lowest in comparison with other infill patterns. The most tensile strength is related to the Solid infill samples. As it was extracted from the results, by changing the infill pattern of the printed CF-PA6 reinforced with continuous glass fiber samples from hexagonal to rectangular and triangular, the tensile strength has been improved 11.1% and 15.92%, respectively. But, by changing the infill pattern of the printing of the samples which were made of CF-PA6 and continuous glass fiber, from the hexagonal to solid infill, the tensile strength improved almost 30.5% (Fig. 107).

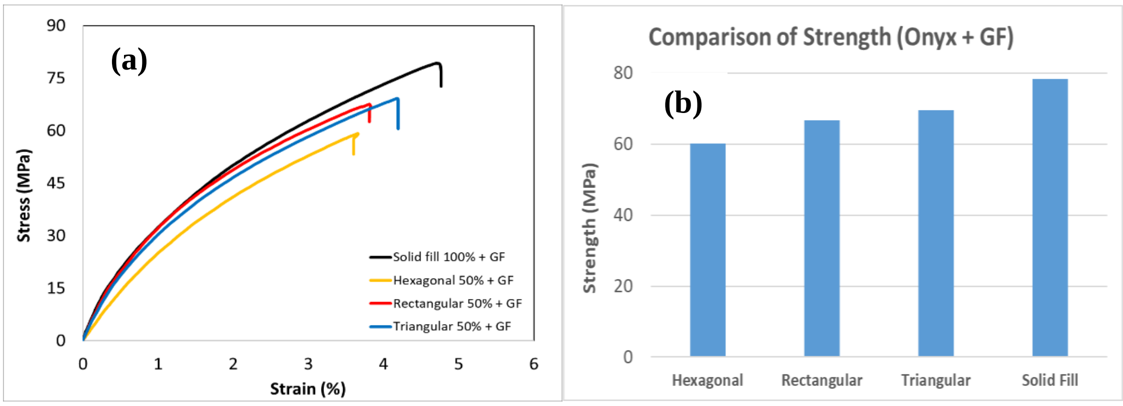

Fig. 107. (a) Quasi-static tensile curves and (b) Strength evolution

Fig. 108, showed the effect of using continuous glass fiber in the solid infill pattern. In fact, by use of continuous glass fiber, the strength of the solid infill samples, increased about 158.5%, respectively.

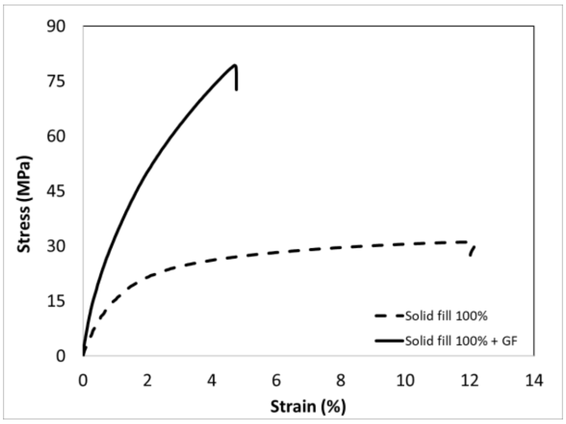

Fig. 108. Quasi-static tensile curves of CF-PA6 (Onyx) and CF6-PA6 reinforced with continuous glass fiber (Onyx + GF) (solid fill pattern)

4.4.1.3 Effect of the density of the continuous reinforcement

As for study the effect of the density of the continuous reinforcement layers, a rectangular sample with thickness of 3.5 mm was designed. The continuous fiberglass was considered for manufacturing the PA6 reinforced with continuous glass fiber composite samples. The 0.1 mm value was selected as the layer height of the deposited PA6 rasters. Also, the layer height of the printed fiber glass was 0.1 mm, too. So, the samples were manufactured by deposition of 35 layers during the layer-by-layer fabrication process. As for study the effect of the density of the continuous glass fiber layers, different quantities of the printed continuous glass fiber layers were considered to manufacture the related samples to compare their tensile strength. The different quantities of the continuous glass fiber layers of 2, 4, 6, 8, and 10 out of the total printed layers (35 layers) were applied in the manufactured specimens. The related tensile strength of the specimens made up 2, 4, 6, 8, and 10 layers were 36.38±0.53 MPa, 144.26±3.18 MPa, 187.55±3.35 MPa, 226.34±5.4 MPa, and 233.72±4.32 MPa, respectively. The tensile strength of the non-reinforced samples, which were processed by 35 layers made of PA6 layers without any continuous glass fiber, was 34.63±2.5 (Fig. 109).

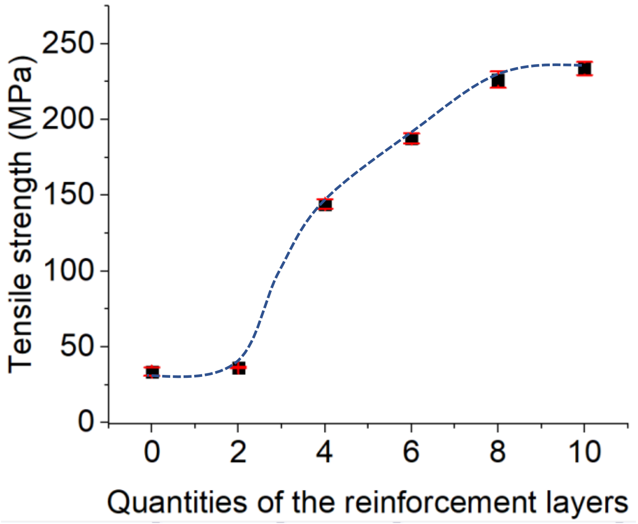

Fig 109. Effect of the density of the continuous reinforcement layers on the tensile strength

As was found out, by increase of the quantities of the continuous glass fiber layers, the tensile strength of the manufactured samples was increased. The tensile strength had a significant increase by enhancement the quantity of the continuous glass fiber layers from 2 layers till 8 layers. But, the amount of the tensile strength increment of the manufactured samples from 8-reinforced layers to 10-reinforced layers were less than the related increase strength amount, provided by enhancement of the quantities of the continuous glass fiber layers from 2-reinforced layers to 4-reinforced layers. These obtained results are correlated to the weaker adhesion strength between the glass fiber reinforcement layers to polymer matrix layers in comparison with polymer to polymer layers. In fact, by enhancement of the quantity of the reinforcement layers from 2 to 8 layers, the tensile strength of the samples was increased because of the existence of the continuous reinforcement which resists against the applied tensile stress. While, the nature of weaker interface strength of the glass fiber reinforcement layers-polymer matrix layers in the manufactured samples which consist of more than 8 reinforcement layers dominated the reinforcement existence impact. So, we can consider that in our manufactured samples, the fabricated specimens made of 8 layer had more optimum density of the continuous reinforcement.

4.4.1.4 Effect of the continuous reinforcement direction

According to the recent stated results, concerning the performed study on the effect of the density of the continuous reinforcement, it was concluded that we can consider an optimum quantity layer for the continuous reinforcement layers in the manufactured reinforced polymer composites by FFF process. In the case of our rectangular tensile test sample, 8 layers of the continuous glass fiber layers prepared an optimum tensile behavior.

Therefore, the continuous glass fiber reinforced PA6 composite samples, reinforced by 8 reinforcement layers were consider to study the tensile behavior of manufactured samples with different continuous reinforcement directions. As for study of the effect of the continuous reinforcement direction, five direction values of 0°, 30°, 45°, 60°, and 90° were considered for continuous glass fibers. The tensile strength values of the related manufactured samples with continuous directions of 0°, 30°, 45°, 60°, and 90° were 226.34±5.4 MPa, 46.8±2.05 MPa, 37±1.1 MPa, 36.81±1.1 MPa, and 36.6±0.79 MPa, respectively (Fig. 110).

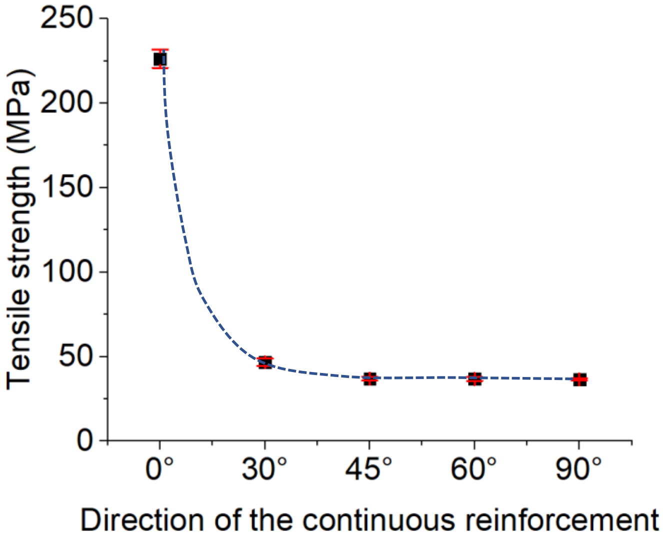

Fig 110. Effect of the direction of the continuous reinforcement on the tensile strength

As it is observed the tensile strength of the manufactured samples with continuous reinforcement with 0°-direction had the most strength in comparison with the other fabricated samples under the different reinforcement directions. As the direction of the continuous reinforcement increased from 0 to 90, the tensile strength was decreased. A significant drop in tensile strength was observed by the change of continuous reinforcement from 0 to 30. The manufactured samples with 45°, 60°, and 90° as the reinforcement directions were so close to each other. Also, the tensile strength of the fabricated samples with continuous reinforcement direction of 90° was so close to the strength of unreinforced samples (33.65±2.8 MPa). So, it understood that manufactured samples with reinforcement direction of 0° had the most strength, while as the direction of reinforcement decreased, the tensile strength was decreased, too. In case of the samples with reinforcement of 0°, the glass fibers resist against the tensile strength well because it was in the direction of the applied strength. While, the fabricated samples with the reinforcement direction of 90°, had the weakest strength because of the perpendicular directions of applied stress and reinforcement. So, in case of samples with glass fiber direction of 90°, the impact of the existence of the reinforcement on the tensile strength wasn't so manifest and sensible. The close tensile strength value of the specimens with reinforcement direction of 90° to the unreinforced specimens can be an evidence of this phenomenon. The macroscopic fracture views showed the same breakage direction and reinforcement direction in the fabricated samples (Fig. 111).

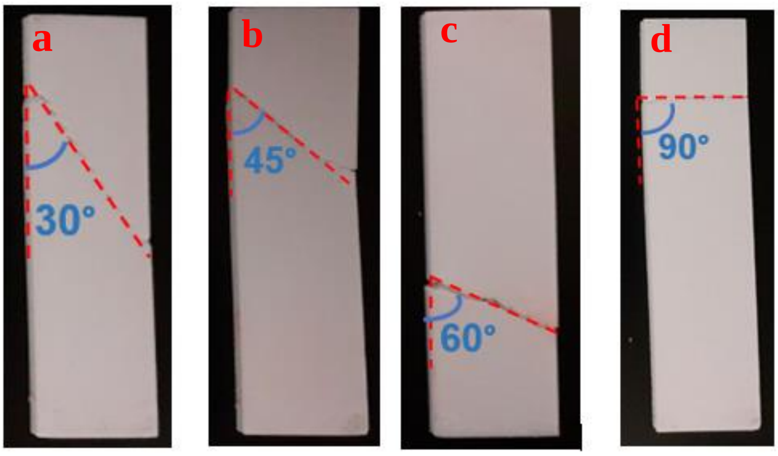

Fig. 111. The macroscopic fracture view of the fabricated samples with the reinforcement directions of (a) 30°, (b) 45°, (c) 60°, and (d) 90°

4.4.2 Fatigue behavior analysis

4.4.2.1 Effect of using the continuous reinforcement

Fig. 112 shows the Wöhler curves obtained in three points bending fatigue tests at a frequency of 10 Hz for CF-PA6 and CF-PA6 reinforced with continuous glass fiber samples.

The curves evidence the effect of the fiber reinforcement. One can note that in the case of the printed specimens with CF-PA6, for applied strain equal to 4.5%, the fatigue life is about 200,000 cycles whereas the fatigue life is about 8000 cycles for CF-PA6 reinforced with continuous glass fiber.

It can be established that for CF-PA6 composite, the fatigue design can be efficiently optimized through glass fiber reinforcement. Regarding CF-PA6 reinforced with continuous glass fiber samples at 10 Hz, it can be noted that the Wöhler curve shows a linear form. However, for the CF-PA6 sample a bi-linear form can be observed.

Wöhler curves obtained from fatigue tests for CF-PA6 and CF-PA6 reinforced with continuous are shown in Fig. 112. One can indicate that there is a small difference between the curves at high amplitude while at low strain amplitude, the Wöhler curve is shifted.

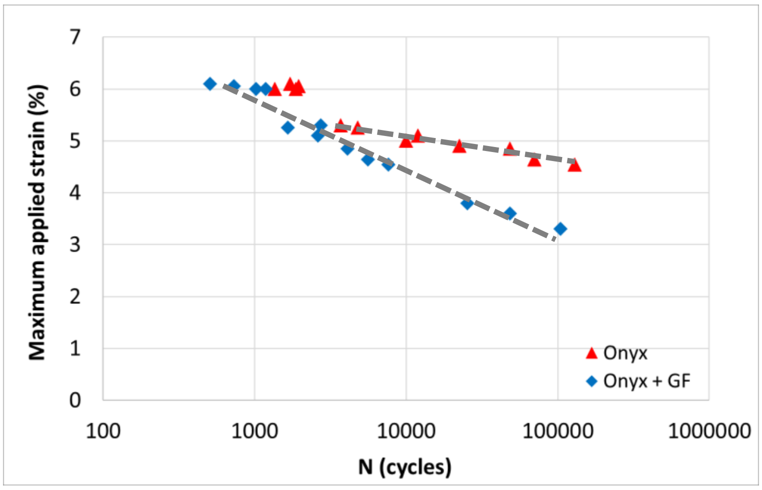

Fig. 112. Wöhler curves for CF-PA6 (Onyx) and CF-PA6 reinforced with continuous glass fiber (Onyx+GF) samples at 10 Hz

4.4.2.2 Relative Young's modulus evolution and self-heating phenomenon

Fig. 113 shows the evolution of the relative stress during fatigue tests for CF-PA6 and CF-PA6 reinforced with continuous glass fiber samples at the frequency of 10 Hz. All samples exhibit a fatigue behavior mostly governed by the Mechanical Fatigue (MF) nature due to damage phenomenon, whereas for high amplitude, the Induced Thermal Fatigue (ITF) is the predominant nature of the fatigue behavior at low cycles for CF-PA6 and CF-PA6 reinforced with continuous glass fiber samples.

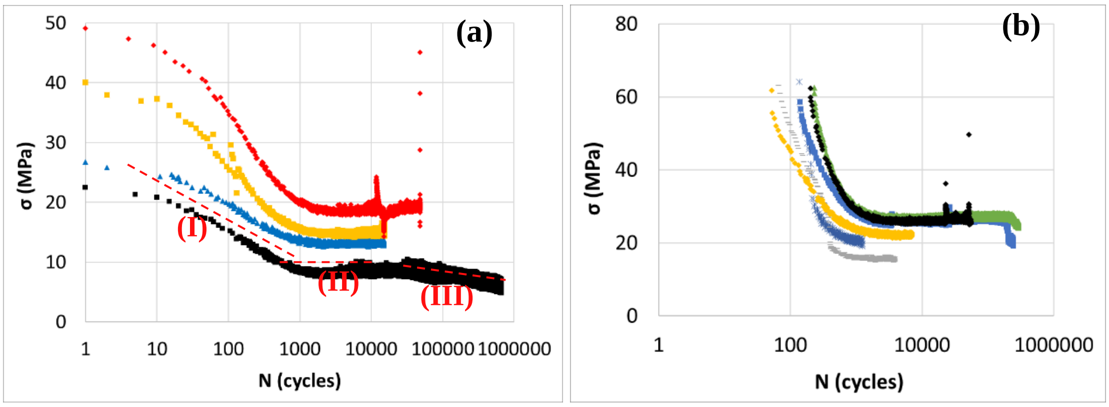

Fig. 113. Evolutions of the relative stress (~Young's modulus) during fatigue tests for (a) CF-PA6 (Onyx) and (b) CF-PA6 reinforced with continuous glass fiber (Onyx+GF) samples

From these curves, one can observe that for high loading amplitudes, the dynamic modulus decreases rapidly in a linear regime of the logarithmic curve until the failure of the specimen. For low applied amplitudes, the dynamic modulus exhibit three decreasing regimes a rapid one during the initial cycles (I), followed by a gradual one (II), and finally a drastic decrease (III) just before the fracture. One can note that the significant damage kinetic in the case of CF-PA6 reinforced with continuous glass fiber (Fig. 114).

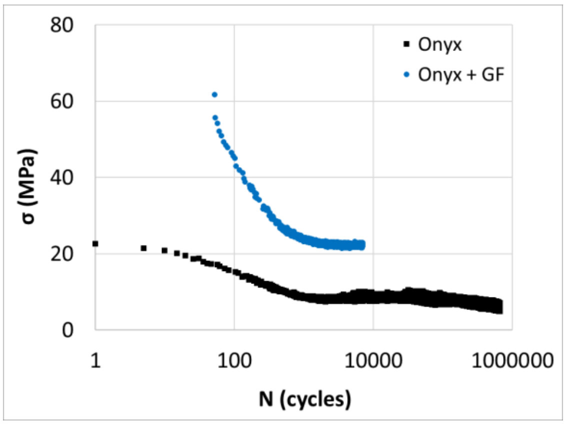

Fig. 114. Evolutions of the relative stress (~Young's modulus) during fatigue tests

Varying the loading conditions in terms of amplitude, the fatigue behavior of CF-PA6 and CF-PA6 reinforced with continuous glass fiber induces self-heating. This phenomenon influences the viscous behavior of the polymer as a function of the temperature rise level concerning material transition temperatures. In the case of CF-PA6 samples, for the test performed at 10 Hz, the temperature increases up to 60 ºC (Fig. 115). This temperature corresponds to the glass transition zone. At this stage, the polymer stiffness slightly decreases as shown in Fig. 102. Therefore, the polymer matrix is subjected to extraordinary thermally activated modifications of its physical state.

Hence, at the microscopic scale, the fatigue behavior and failure of printed CF-PA6 samples are not only due to the devolvement of diffuse damage but also to the evolution of the viscous behavior of the polymer and the inherent brittle-ductile transition. The evolution of temperature is one of the critical parameters in fatigue. Maximum induced temperature can be a factor in predicting the fatigue behavior of CF-PA6 and reinforced CF-PA6 with continuous glass fiber and the state of polymer in terms of ductility. Fig. 115, illustrates the maximum induced temperature just before failure. Fig. 115, presents the influence of reinforcement on the maximum induced temperature.

One can observe the same slope of the curve for two cases. As was mentioned, there are two types of fatigue: MF and ITF. By considering the glass transition temperature of about 61°C, the critical fatigue tests with induced thermal fatigue can be separated. Moreover, one can note that the induced temperature for all applied strains is higher in the case of CF-PA6 (without continuous reinforcement).

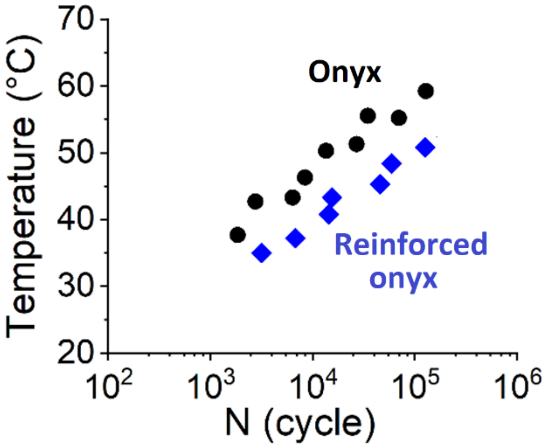

Fig. 115. Maximum induced temperature evolution versus the number of cycles

4.4.2.3 Fatigue fracture surface

For emphasizing the effect of loading amplitude at a microscopic scale fracture surface observations have been performed. Fig. 116, compares the fracture surfaces of the printed CF-PA6 and CF-PA6 reinforced with continuous glass fiber samples. SEM analysis highlights these conclusions:

- For the printed CF-PA6 samples, the first observed damage phenomenon corresponds to the debonding of the filament. This leads to the propagation of interphase cracking. For a higher value of cycles, this damage mechanism is spreading through the whole observation zone (Fig. 116 (a)).
- The fracture surface observation in the case of CF-PA6 reinforced with continuous glass fiber samples, showed that the bundles of fibers are pulled out from CF-PA6 simultaneously with breakage of the more surrounding matrix (Fig. 116 (b)).

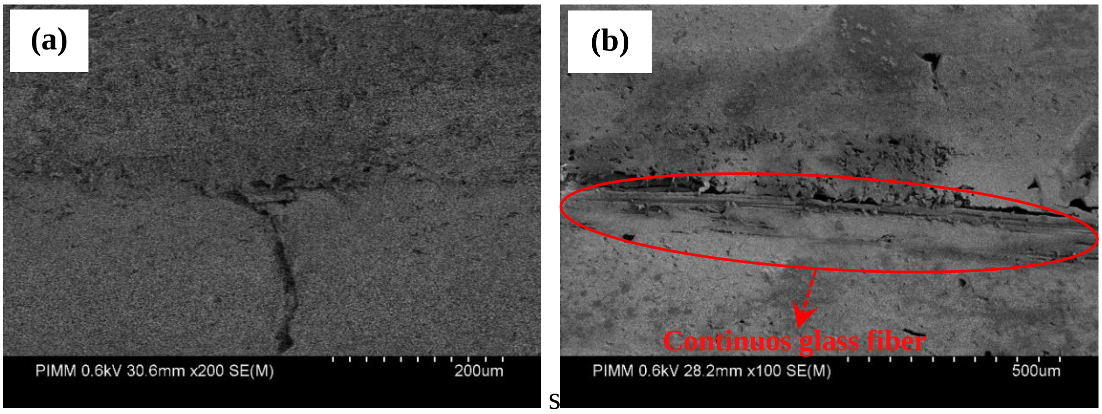

Fig. 116. Fracture surface observations for CF-PA6 (a), and CF-PA6 reinforced with continuous glass fiber (b) samples

5 Conclusions and perspectives

This thesis was carried out between two laboratories, PIMM and LCPI, at Arts et Métiers institute of Technology. The main purpose of this research was to study the rheological characteristics of materials during FFF to process optimization and mechanical characterization improvement of the fabricated parts. In fact, the essential problem with parts produced with the FFF process is the adhesion between the filaments and the presence of porosity inside the part. Good adhesion between a solid material and a very viscous molten material cannot be expected. One can note that, a precise and local measurement of the temperature on the scale of the diameter of the filaments is necessary. Therefore, the main issue is to consider both temperature and viscosity parameters. And establish the Time-Temperature-Transformation diagram for process optimization. This helps us to determine the processability area.

According to the performed investigation for the impact of some important FFF process parameters of polymer-based composites on the inter-layer adhesion (bonding) of the deposited filaments. The thermal, physicochemical and mechanical analysis showed that degree of crystallinity can affect the diffusion of the material during the cooling stage and the bonding of two adjacent filaments and consequently the mechanical properties of the final part. Temperature profile evaluation of printed layers illustrates that FFF process parameters have a significant effect on the cooling process of filaments which modifies the bonding of adjacent filaments. Failure stress/strain can be the indicators to figure out the mechanical properties of FFF manufactured products. One can note that the polymer used in this study was PA6 which has low molecular weight and low viscosity. To analyze the effect of process parameters in this type of materials, it is important to pay close attention to the temperature. By increasing the bed temperature, the problems of dimensional stability and voids presence can occur in the printed parts made of CF-PA6.

Also, polymer-based composites using Fused Filament Fabrication (FFF) were prepared and submitted to tension and three points bending fatigue loadings. The related main conclusion for this investigation is as follows: firstly, the homogeneous and unidirectional distribution of carbon fibers in the used CF-PA6 filament was observed through the microscopy observation. The printed CF-PA6 samples in solid infill pattern, have excellent stiffness and mechanical properties under tension. In fatigue, the effect of reinforcement has been analyzed. The results showed that the induced temperature is increased and as a result, the fatigue life is decreased for and reinforced CF-PA6. This phenomenon, which is known as self-heating, can evaluate the viscous behavior of the polymer especially in the glass transition zone. Therefore, it is necessary to study the viscoelastic behavior of CF-PA6. Perez model could predict the viscoelastic behavior of CF-PA6 and CF-PA6 reinforced with continuous glass fiber. Finally, damage mechanisms development in fatigue has been investigated at the microscopic scale. For CF-PA6 and reinforced CF-PA6 with continuous glass fiber, the first observed damage phenomenon corresponds to the debonding of the filaments which leads to the propagation of cracking.

Moreover, the effects of the density and direction of continuous glass fiber in FFF process of polymer-based composites were studied. It was found out that by increase of the density of the continuous glass fibers in the manufacture composite, the strength was increased, too. By utilization the continuous reinforcement, the increment in the strength was increased significantly until a specific value. Then, the strength of the manufactured specimens by more than the specific density of the applied continuous reinforcement became stable. This phenomenon is due to lower adhesion between continuous reinforcement layers and polymer matrix in comparison with adhesion between the deposited polymer matrix layers. As for study the effect of the direction of the continuous reinforcement in the FFF process polymer composite materials, the five directions of 0°, 30°, 45°, 60°, 90° were investigated. The highest strength was related to the manufactured parts, in which the reinforcements were in the applied stress direction (0°). As the direction of the used reinforcement deviated more from the applied stress direction, the strength of the manufactured parts was decreased. Hence, a significant drop in tensile strength was observed by the change of continuous reinforcement from 0° to 30°. The manufactured samples with 45°, 60°, and 90° as the reinforcement directions were so close to each other. Also, the tensile strength of the fabricated samples with the continuous reinforcement direction of 90° was so close to the strength of unreinforced samples. The fracture of the tensile tested samples occurred in the direction of the deposited continuous reinforcement. As the perspective of this work, several subjects can be considered:

- Overall study of the quality of final part,
- Further analysis through the non-isotherm viscosity evolution and developing the rheological model considering the viscoelastic properties of polymer,
- To improve and optimize the inter-layer adhesion of filaments, thermo-mechanical modeling is required
- Bonding optimization could be performed by applying all findings.

6 References

1. Fatimatuzahraa, A. W., Farahaina, B., & Yusoff, W. A. Y. (2011, September). The effect of employing different raster orientations on the mechanical properties and microstructure of Fused Deposition Modeling parts. In 2011 IEEE Symposium on Business, Engineering and Industrial Applications (ISBEIA) (pp. 22-27).

2. Croccolo, D., De Agostinis, M., & Olmi, G. (2013). Experimental characterization and analytical modelling of the mechanical behaviour of fused deposition processed parts made of ABS-M30. Computational Materials Science, 79, 506-518.

3. Mahmood, S., Qureshi, A. J., Goh, K. L., & Talamona, D. (2017). Tensile strength of partially filled FFF printed parts: experimental results. Rapid Prototyping Journal.

4. Cuan-Urquizo, E., Barocio, E., Tejada-Ortigoza, V., Pipes, R. B., Rodriguez, C. A., & Roman-Flores, A. (2019). Characterization of the mechanical properties of FFF structures and materials: A review on the experimental, computational and theoretical approaches. Materials, 12(6), 895.

5. Harris, M., Potgieter, J., Archer, R., & Arif, K. M. (2019). Effect of material and process specific factors on the strength of printed parts in fused filament fabrication: A review of recent developments. Materials, 12(10), 1664.

6. Fodran, Eric, Martin Koch, and Unny Menon. "Mechanical and dimensional characteristics of fused deposition modeling build styles." 1996 International Solid Freeform Fabrication Symposium. 1996.

7. Furlanello, F., Bertoldi, A., Dallago, M., Furlanello, C., Fernando, F., Inama, G., ... & Chierchia, S. (1998). Cardiac arrest and sudden death in competitive athletes with arrhythmogenic right ventricular dysplasia. Pacing and clinical electrophysiology, 21(1), 331-335.

8. Es-Said, O. S., Foyos, J., Noorani, R., Mendelson, M., Marloth, R., & Pregger, B. A. (2000). Effect of layer orientation on mechanical properties of rapid prototyped samples. Materials and Manufacturing Processes, 15(1), 107-122.

9. Rodríguez, J. F., Thomas, J. P., & Renaud, J. E. (2001). Mechanical behavior of acrylonitrile butadiene styrene (ABS) fused deposition materials. Experimental investigation. Rapid Prototyping Journal.

10. Ahn, S. H., Montero, M., Odell, D., Roundy, S., & Wright, P. K. (2002). Anisotropic material properties of fused deposition modeling ABS. Rapid prototyping journal.

11. Lee, B. H., Abdullah, J., & Khan, Z. A. (2005). Optimization of rapid prototyping parameters for production of flexible ABS object. Journal of materials processing technology, 169(1), 54-61.

12. Sun, Q., Rizvi, G. M., Bellehumeur, C. T., & Gu, P. (2008). Effect of processing conditions on the bonding quality of FDM polymer filaments. Rapid Prototyping Journal.

13. Sood, A. K., Ohdar, R. K., & Mahapatra, S. S. (2010). Parametric appraisal of mechanical property of fused deposition modelling processed parts. Materials & Design, 31(1), 287-295.

14. Sood, A. K., Ohdar, R. K., & Mahapatra, S. S. (2012). Experimental investigation and empirical modelling of FDM process for compressive strength improvement. Journal of Advanced Research, 3(1), 81-90.

15. Durgun, I., & Ertan, R. (2014). Experimental investigation of FDM process for improvement of mechanical properties and production cost. Rapid Prototyping Journal.

16. Górski, F., Kuczko, W. I. E. S. Ł. A. W., & Wichniarek, R. A. D. O. S. Ł. A. W. (2014). Impact strength of ABS parts manufactured using Fused Deposition Modeling technology. Archives of Mechanical Technology and Automation, 31(1), 3-12.

17. Baich, L., Manogharan, G., & Marie, H. (2015). Study of infill print design on production cost-time of 3D printed ABS parts. International Journal of Rapid Manufacturing, 5(3-4), 308-319.

18. Górski, F., Wichniarek, R., Kuczko, W., & Andrzejewski, J. (2015). Experimental determination of critical orientation of ABS parts manufactured using fused deposition modelling technology. Journal of Machine Engineering, 15(4), 121-132.

19. Ziemian, S., Okwara, M., & Ziemian, C. W. (2015). Tensile and fatigue behavior of layered acrylonitrile butadiene styrene. Rapid Prototyping Journal.

20. Onwubolu, G. C., & Rayegani, F. (2014). Characterization and optimization of mechanical properties of ABS parts manufactured by the fused deposition modelling process. International Journal of Manufacturing Engineering, 2014.

21. Tymrak, B. M., Kreiger, M., & Pearce, J. M. (2014). Mechanical properties of components fabricated with open-source 3-D printers under realistic environmental conditions. Materials & Design, 58, 242-246.

22. Ebel, E., & Sinnemann, T. (2014). Fabrication of FDM 3D objects with ABS and PLA and determination of their mechanical properties. RTejournal, 2014(1).

23. Rankouhi, B., Javadpour, S., Delfanian, F., & Letcher, T. (2016). Failure analysis and mechanical characterization of 3D printed ABS with respect to layer thickness and orientation. Journal of Failure Analysis and Prevention, 16(3), 467-481.

24. Letcher, T., Rankouhi, B., & Javadpour, S. (2015, November). Experimental study of mechanical properties of additively manufactured ABS plastic as a function of layer parameters. In ASME International Mechanical Engineering Congress and Exposition (Vol. 57359, p. V02AT02A018). American Society of Mechanical Engineers.

25. Fernandez-Vicente, M., Calle, W., Ferrandiz, S., & Conejero, A. (2016). Effect of infill parameters on tensile mechanical behavior in desktop 3D printing. 3D printing and additive manufacturing, 3(3), 183-192.

26. Alvarez C, K. L., Lagos C, R. F., & Aizpun, M. (2016). Investigating the influence of infill percentage on the mechanical properties of fused deposition modelled ABS parts. Ingeniería e Investigación, 36(3), 110-116.

27. Hernandez, R., Slaughter, D., Whaley, D., Tate, J., & Asiabanpour, B. (2016). Analyzing the tensile, compressive, and flexural properties of 3D printed ABS P430 plastic based on printing orientation using fused deposition modeling. In 27th Annual International Solid Freeform Fabrication Symposium, Austin, TX (pp. 939-950).

28. Torrado, A. R., & Roberson, D. A. (2016). Failure analysis and anisotropy evaluation of 3D-printed tensile test specimens of different geometries and print raster patterns. Journal of Failure Analysis and Prevention, 16(1), 154-164.

29. Raney, K., Lani, E., & Kalla, D. K. (2017). Experimental characterization of the tensile strength of ABS parts manufactured by fused deposition modeling process. Materials Today: Proceedings, 4(8), 7956-7961.

30. Cantrell, J. T., Rohde, S., Damiani, D., Gurnani, R., DiSandro, L., Anton, J., ... & Ifju, P. G. (2017). Experimental characterization of the mechanical properties of 3D-printed ABS and polycarbonate parts. Rapid Prototyping Journal.

31. Montero, Michael, Shad Roundy, Dan Odell, Sung-Hoon Ahn, and Paul K. Wright. "Material characterization of fused deposition modeling (FDM) ABS by designed experiments." Society of Manufacturing Engineers 10, no. 13552540210441166 (2001).

32. Schöppner, Volker, and Kunststofftechnik Paderborn KTP. "Mechanical properties of fused deposition modeling parts manufactured with Ultem* 9085." In Proceedings of 69th Annual Technical Conference of the Society of Plastics Engineers (ANTEC'11), vol. 2, pp. 1294-1298. 2011.

33. Sood, Anoop Kumar, Raj K. Ohdar, and Siba S. Mahapatra. "Parametric appraisal of mechanical property of fused deposition modelling processed parts." Materials & Design 31, no. 1 (2010): 287-295.

34. Ziemian, Constance, Mala Sharma, and Sophia Ziemian. "Anisotropic mechanical properties of ABS parts fabricated by fused deposition modelling." Mechanical engineering 23 (2012).

35. Chin Ang, Ker, Kah Fai Leong, Chee Kai Chua, and Margam Chandrasekaran. "Investigation of the mechanical properties and porosity relationships in fused deposition modelling-fabricated porous structures." Rapid Prototyping Journal 12, no. 2 (2006): 100-105.

36. Melnikova, Rimma, Andrea Ehrmann, and Karin Finsterbusch. "3D printing of textile-based structures by Fused Deposition Modelling (FDM) with different polymer materials." In IOP conference series: materials science and engineering, vol. 62, no. 1, p. 012018. IOP publishing, 2014.

37. Perkins, Isaac, and Martin Skitmore. "Three-dimensional printing in the construction industry: A review." International Journal of Construction Management 15, no. 1 (2015): 1-9.

38. Stoof, David, and Kim Pickering. "Sustainable composite fused deposition modelling filament using recycled pre-consumer polypropylene." Composites Part B: Engineering 135 (2018): 110-118.

39. Carneiro, Olga S., A. F. Silva, and Rui Gomes. "Fused deposition modeling with polypropylene." Materials & Design 83 (2015): 768-776.

40. Nikzad, M., Masood, S. H., & Sbarski, I. (2011). Thermo-mechanical properties of a highly filled polymeric composites for fused deposition modeling. Materials & Design, 32(6), 3448-3456.

41. Hwang, S., Reyes, E. I., Moon, K. S., Rumpf, R. C., & Kim, N. S. (2015). Thermo-mechanical characterization of metal/polymer composite filaments and printing parameter study for fused deposition modeling in the 3D printing process. Journal of Electronic Materials, 44(3), 771-777.

42. Isakov, D. V., Lei, Q., Castles, F., Stevens, C. J., Grovenor, C. R. M., & Grant, P. S. (2016). 3D printed anisotropic dielectric composite with meta-material features. Materials & Design, 93, 423-430.

43. Shemelya, C. M., Rivera, A., Perez, A. T., Rocha, C., Liang, M. I. N., Yu, X., ... & Wicker, R. B. (2015). Mechanical, electromagnetic, and X-ray shielding characterization of a 3D printable tungsten–polycarbonate polymer matrix composite for space-based applications. Journal of Electronic Materials, 44(8), 2598-2607.

44. Boparai, K., Singh, R., & Singh, H. (2015). Comparison of tribological behaviour for Nylon6-Al-Al2O3 and ABS parts fabricated by fused deposition modelling: This paper reports a low cost composite material that is more wear-resistant than conventional ABS. Virtual and Physical Prototyping, 10(2), 59-66.

45. Matsuzaki, R., Ueda, M., Namiki, M., Jeong, T. K., Asahara, H., Horiguchi, K., ... & Hirano, Y. (2016). Three-dimensional printing of continuous-fiber composites by in-nozzle impregnation. Scientific reports, 6, 23058.

46. Hao, W., Liu, Y., Zhou, H., Chen, H., & Fang, D. (2018). Preparation and characterization of 3D printed continuous carbon fiber reinforced thermosetting composites. Polymer Testing, 65, 29-34.

47. Li, N., Li, Y., & Liu, S. (2016). Rapid prototyping of continuous carbon fiber reinforced polylactic acid composites by 3D printing. Journal of Materials Processing Technology, 238, 218-225.

48. Tian, X., Liu, T., Yang, C., Wang, Q., & Li, D. (2016). Interface and performance of 3D printed continuous carbon fiber reinforced PLA composites. Composites Part A: Applied Science and Manufacturing, 88, 198-205.

49. Hao, W., Yuan, Y., Zhu, J., & Chen, L. (2016). Effect of impact damage on the curved beam interlaminar strength of carbon/epoxy laminates. Journal of adhesion science and Technology, 30(11), 1189-1200.

50. Akhoundi, B., Behravesh, A. H., & Bagheri Saed, A. (2019). Improving mechanical properties of continuous fiber-reinforced thermoplastic composites produced by FDM 3D printer. Journal of Reinforced Plastics and Composites, 38(3), 99-116.

51. Van Der Klift, F., Koga, Y., Todoroki, A., Ueda, M., Hirano, Y., & Matsuzaki, R. (2016). 3D printing of continuous carbon fibre reinforced thermo-plastic (CFRTP) tensile test specimens. Open Journal of Composite Materials, 6(01), 18.

52. Agarwal, K., Kuchipudi, S. K., Girard, B., & Houser, M. (2018). Mechanical properties of fiber reinforced polymer composites: A comparative study of conventional and additive manufacturing methods. Journal of Composite Materials, 52(23), 3173-3181.

53. Oztan, C., Karkkainen, R., Fittipaldi, M., Nygren, G., Roberson, L., Lane, M., & Celik, E. (2019). Microstructure and mechanical properties of three dimensional-printed continuous fiber composites. Journal of Composite Materials, 53(2), 271-280.

54. Dong, G., Tang, Y., Li, D., & Zhao, Y. F. (2018). Mechanical properties of continuous kevlar fiber reinforced composites fabricated by fused deposition modeling process. Procedia Manufacturing, 26, 774-781.

55. Ning, F., Cong, W., Qiu, J., Wei, J., & Wang, S. (2015). Additive manufacturing of carbon fiber reinforced thermoplastic composites using fused deposition modeling. Composites Part B: Engineering, 80, 369-378.

56. van de Werken, N., Hurley, J., Khanbolouki, P., Sarvestani, A. N., Tamijani, A. Y., & Tehrani, M. (2019). Design considerations and modeling of fiber reinforced 3D printed parts. Composites Part B: Engineering, 160, 684-692.

57. N. Sarvestani, A., van de Werken, N., Khanbolouki, P., & Tehrani, M. (2017, November). 3D printed composites with continuous carbon fiber reinforcements. In ASME International Mechanical Engineering Congress and Exposition (Vol. 58356, p. V002T02A031). American Society of Mechanical Engineers.

58. Chen, Y., Rios, C. O., Imeri, A., Russell, N. A., & Fidan, I. (2020). Investigation of the tensile properties in fibre-reinforced additive manufacturing and fused filament fabrication. International Journal of Rapid Manufacturing, 9(2-3), 251-267.

59. Imeri, A., Fidan, I., Allen, M., & Perry, G. (2018). Effect of fiber orientation in fatigue properties of FRAM components. Procedia Manufacturing, 26, 892-899.

60. Dickson, A. N., Barry, J. N., McDonnell, K. A., & Dowling, D. P. (2017). Fabrication of continuous carbon, glass and Kevlar fibre reinforced polymer composites using additive manufacturing. Additive Manufacturing, 16, 146-152.

61. Chuncheng, Y. (2017). 3D printing for continuous fiber reinforced thermoplastic composites: mechanism and performance. Rapid Prototyping J, 23(1), 209-215.

62. Tian, X., Liu, T., Wang, Q., Dilmurat, A., Li, D., & Ziegmann, G. (2017). Recycling and remanufacturing of 3D printed continuous carbon fiber reinforced PLA composites. Journal of cleaner production, 142, 1609-1618.

63. Melenka, G. W., Cheung, B. K., Schofield, J. S., Dawson, M. R., & Carey, J. P. (2016). Evaluation and prediction of the tensile properties of continuous fiber-reinforced 3D printed structures. Composite Structures, 153, 866-875.

64. Bettini, P., Alitta, G., Sala, G., & Di Landro, L. (2017). Fused deposition technique for continuous fiber reinforced thermoplastic. Journal of Materials Engineering and Performance, 26(2), 843-848.

65. Zhong, W., Li, F., Zhang, Z., Song, L., & Li, Z. (2001). Short fiber reinforced composites for fused deposition modeling. Materials Science and Engineering: A, 301(2), 125-130.

66. Tekinalp, H. L., Kunc, V., Velez-Garcia, G. M., Duty, C. E., Love, L. J., Naskar, A. K., ... & Ozcan, S. (2014). Highly oriented carbon fiber–polymer composites via additive manufacturing. Composites Science and Technology, 105, 144-150.

67. Love, L. J., Kunc, V., Rios, O., Duty, C. E., Elliott, A. M., Post, B. K., ... & Blue, C. A. (2014). The importance of carbon fiber to polymer additive manufacturing. Journal of Materials Research, 29(17), 1893.

68. Yasa, E. (2019). ANISOTROPIC IMPACT TOUGHNNESS OF CHOPPED CARBON FIBER REINFORCED NYLON FABRICATED BY MATERIAL-EXTRUSION-BASED ADDITIVE MANUFACTURING. Anadolu University of Sciences & Technology-A: Applied Sciences & Engineering, 20(2).

69. Carneiro, O. S., Silva, A. F., & Gomes, R. (2015). Fused deposition modeling with polypropylene. Materials & Design, 83, 768-776.

70. Lewicki, J. P., Rodriguez, J. N., Zhu, C., Worsley, M. A., Wu, A. S., Kanarska, Y., ... & Hensleigh, R. (2017). 3D-printing of meso-structurally ordered carbon fiber/polymer

composites with unprecedented orthotropic physical properties. Scientific reports, 7(1), 1-14.

71. Gupta, A., Fidan, I., Hasanov, S., & Nasirov, A. (2020). Processing, mechanical characterization, and micrography of 3D-printed short carbon fiber reinforced polycarbonate polymer matrix composite material. The International Journal of Advanced Manufacturing Technology, 107(7), 3185-3205.

72. Hill, C., Rowe, K., Bedsole, R., Earle, J., & Kunc, V. (2016, May). Materials and process development for direct digital manufacturing of vehicles. In SAMPE Long Beach 2016 Conference and Exhibition.

73. Kunc, V. (2015, September). Advances and challenges in large scale polymer additive manufacturing. In Proceedings of the 15th SPE Automotive Composites Conference, Novi, MI, USA (Vol. 9).

74. Duty, C. E., Drye, T., & Franc, A. (2015). Material development for tooling applications using big area additive manufacturing (BAAM) (No. ORNL/TM-2015/78). Oak Ridge National Lab.(ORNL), Oak Ridge, TN (United States). Manufacturing Demonstration Facility (MDF).

75. Duty, C. E., Kunc, V., Compton, B., Post, B., Erdman, D., Smith, R., ... & Love, L. (2017). Structure and mechanical behavior of Big Area Additive Manufacturing (BAAM) materials. Rapid Prototyping Journal.

76. Perez, A. R. T., Roberson, D. A., & Wicker, R. B. (2014). Erratum to: Fracture surface analysis of 3D-printed tensile specimens of novel ABS-based materials. Journal of Failure Analysis and Prevention, 14(4), 549-549.

77. Shofner, M. L., Lozano, K., Rodríguez-Macías, F. J., & Barrera, E. V. (2003). Nanofiber-reinforced polymers prepared by fused deposition modeling. Journal of applied polymer science, 89(11), 3081-3090.

78. Ferreira, R. T. L., Amatte, I. C., Dutra, T. A., & Bürger, D. (2017). Experimental characterization and micrography of 3D printed PLA and PLA reinforced with short carbon fibers. Composites Part B: Engineering, 124, 88-100.

79. Shofner, M. L. (2003). FJ Rodr iguez-Mac Ias, R. Vaidyanathan, and EV Barrera,“. Single wall nanotube and vapor grown carbon fiber reinforced polymers processed by extrusion freeform fabrication,” Composites, Part A, 34(12), 1207-1217.

80. Compton, B. G., & Lewis, J. A. (2014). 3D-printing of lightweight cellular composites. Advanced materials, 26(34), 5930-5935.

81. Mahajan, C., & Cormier, D. (2015). 3D printing of carbon fiber composites with preferentially aligned fibers. In IIE annual conference. Proceedings (p. 2953). Institute of Industrial and Systems Engineers (IISE).

82. Gardner, J. M., Sauti, G., Kim, J. W., Cano, R. J., Wincheski, R. A., Stelter, C. J., ... & Siochi, E. J. (2016). Additive manufacturing of multifunctional components using high density carbon nanotube yarn filaments.

83. DeNardo, N. M. (2016). Additive manufacturing of carbon fiber-reinforced thermoplastic composites.

84. Chacón, J. M., Caminero, M. A., Núñez, P. J., García-Plaza, E., García-Moreno, I., & Reverte, J. M. (2019). Additive manufacturing of continuous fibre reinforced thermoplastic composites using fused deposition modelling: Effect of process

parameters on mechanical properties. Composites science and technology, 181, 107688.

85. https://markforged.com/materials/plastics/nylon
https://markforged.com/materials/plastics/onyx

86. Krylova, V., and N. Dukštienė. "The structure of PA-Se-S-Cd composite materials probed with FTIR spectroscopy." Applied Surface Science 470 (2019): 462-471.

87. Rao, V. D. P., Rajiv, P., & Geethika, V. N. (2019). Effect of fused deposition modelling (FDM) process parameters on tensile strength of carbon fibre PLA. Materials Today: Proceedings, 18, 2012-2018.

88. Bellehumeur, C., Li, L., Sun, Q. and Gu, P., Modeling of bond formation between polymer filaments in the fused deposition modeling process. Journal of manufacturing processes, 2004. 6(2): p. 170-178.

89. Costa, S., F. Duarte, and J. Covas, Towards modelling of Free Form Extrusion: analytical solution of transient heat transfer. International Journal of Material Forming, 2008. 1(1): p. 703-706.

90. Costa, S., F. Duarte, and J. Covas, Thermal conditions affecting heat transfer in FDM/FFE: a contribution towards the numerical modelling of the process: This paper investigates convection, conduction and radiation phenomena in the filament deposition process. Virtual and Physical Prototyping, 2015. 10(1): p. 35-46.

91. Thomas, J. and J. Rodríguez. Modeling the fracture strength between fused-deposition extruded roads 16. in 2000 international solid freeform fabrication symposium. 2000.

92. Yardimci, M.A. and S. Güçeri, Conceptual framework for the thermal process modelling of fused deposition. Rapid Prototyping Journal, 1996.

93. AtifYardimci, M., Hattori, T., Guceri, S.I. and Danforth, S.C., Thermal analysis of fused deposition. in 1997 international solid freeform fabrication symposium. 1997.

94. Zhang, Y. and Y. Chou, Three-dimensional finite element analysis simulations of the fused deposition modelling process. Proceedings of the Institution of Mechanical Engineers, Part B: Journal of Engineering Manufacture, 2006. 220(10): p. 1663-1671.

95. Ji, L.B. and T.R. Zhou. Finite element simulation of temperature field in fused deposition modeling. in Advanced Materials Research. 2010. Trans Tech Publ.

96. Seppala, J.E. and K.D. Migler, Infrared thermography of welding zones produced by polymer extrusion additive manufacturing. Additive manufacturing, 2016. 12: p. 71-76.

97. D’Amico, A. and A.M. Peterson, An adaptable FEA simulation of material extrusion additive manufacturing heat transfer in 3D. Additive Manufacturing, 2018. 21: p. 422-430.

98. Costa, S., F. Duarte, and J. Covas, Estimation of filament temperature and adhesion development in fused deposition techniques. Journal of Materials Processing Technology, 2017. 245: p. 167-179.

99. Jiang, Z., Diggle, B., Tan, M.L., Viktorova, J., Bennett, C.W. and Connal, L.A., Extrusion 3D Printing of Polymeric Materials with Advanced Properties. Advanced Science, 2020. 7(17): p. 2001379.

100. Scheithauer, U., Schwarzer, E., Richter, H.J. and Moritz, T., Thermoplastic 3D printing—an additive manufacturing method for producing dense ceramics. International journal of applied ceramic technology, 2015. 12(1): p. 26-31.

101. Duty, C., Ajinjeru, C., Kishore, V., Compton, B., Hmeidat, N., Chen, X., Liu, P., Hassen, A.A., Lindahl, J. and Kunc, V., What makes a material printable? A viscoelastic model for extrusion-based 3D printing of polymers. Journal of Manufacturing Processes, 2018. 35: p. 526-537.

7 Appendix (French version)

1. Introduction :

Le procédé de fabrication par filaments fondus (FFF) des composites à base de polymères se distingue par sa capacité à créer rapidement des objets de formes complexes avec des propriétés mécaniques raisonnables. Pourtant, l'amélioration de ces propriétés représente encore une priorité majeure pour les concepteurs dont l'objectif est d'élargir l'employabilité de ce procédé. Il existe plusieurs stratégies afin d'améliorer les propriétés souhaitées des pièces ainsi produites ; par exemple en optimisant les paramètres du processus et/ou en utilisant d'autres conceptions architecturales.

Le présent rapport s'intéresse à l'effet de certains paramètres du processus FFF (température de liquéfaction, vitesse d'impression, hauteur de couche et température de la plate-forme) sur l'évolution de la température et du comportement mécanique de pièces en PA6 renforcé de fibres de carbone coupées. En raison du dépôt par couches, il existe un profil cyclique de température. Celui-ci représente un critère majeur pour la fabrication et par conséquent la résistance des pièces ainsi fabriquées. Parallèlement à l'étude de l'effet des paramètres du procédé, ce profil de température cyclique a été mesuré.

Les résultats préliminaires liés aux propriétés physico-chimiques et mécaniques ont montré que des différences de pourcentage de cristallinité existent et que la contrainte et la déformation à la rupture peuvent être considérées comme des indicateurs pour évaluer les propriétés mécaniques des objets obtenus par ce procédé. La mesure du profil de température cyclique révèle que les paramètres du processus ont une influence considérable sur la phase de refroidissement des filaments déposés, ce qui se répercute alors sur la liaison entre filaments adjacents. Les températures plus élevées présentent une vitesse de refroidissement plus lente. Enfin, les résultats confirment l'impact des paramètres mentionnés sur la formation de la liaison dans le procédé FFF ainsi que sur les propriétés mécaniques obtenues sur les pièces imprimées. Par conséquent, le choix de paramètres de processus optimisés et appropriés apparaît comme une étape de conception importante.

2. Description du matériel, dispositif d'impression 3D et méthodes de caractérisation :

2.1 Préparation du matériel et des échantillons

Le matériau sélectionné pour cette étude est un PA6 renforcé avec des fibres de carbone coupées (CF). Ce matériau désigné commercialement sous le nom d'Onyx sera référencé CF-PA6 pour les besoins de cette étude. En fait, le CF-PA6 utilisé est introduit en tant que filament composite. Il peut également être utilisé comme étant le matériau de la matrice pour fabriquer les pièces composites continues avec les imprimantes 3D Markforged. Les résultats issus de la pyrolyse du filament CF-PA6 utilisé dans le cadre de cette recherche ont montré une teneur en masse de fibre de carbone hachés de 6.5 %.

La Fig. 1 illustre la géométrie retenue des échantillons utilisés pour étudier l'influence des paramètres du procédé FFF sur les comportements thermiques et mécaniques. Les spécimens ont été imprimés avec une imprimante commerciale FlashForge Adventurer 3. Les paramètres du processus sont rapportés dans le tableau 1. Les emplacements des échantillons requis pour appliquer les différents tests et caractérisations sont présentés en Fig.2. Le suivi de l'évolution Temps-Température a également été enregistré lors de l'impression des spécimens.

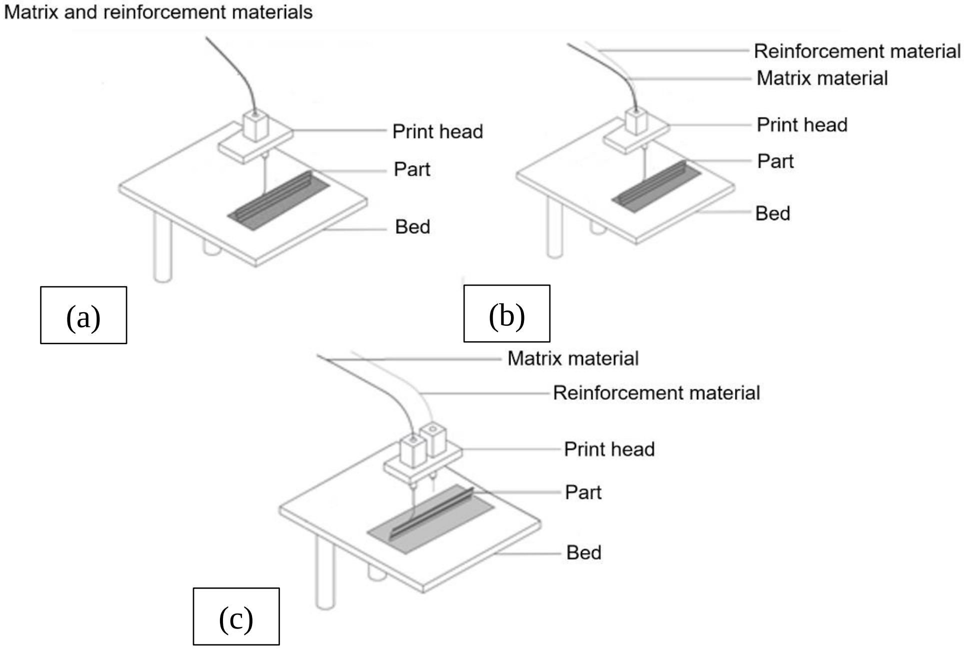

Fig. 1. Fabrication par filaments fondus renforcés avec : (a) un filament composite (comme matière première), (b) un filament et une fibre combinés à travers la tête d'impression et (c) un filament et une fibre combinés avec deux buses indépendantes

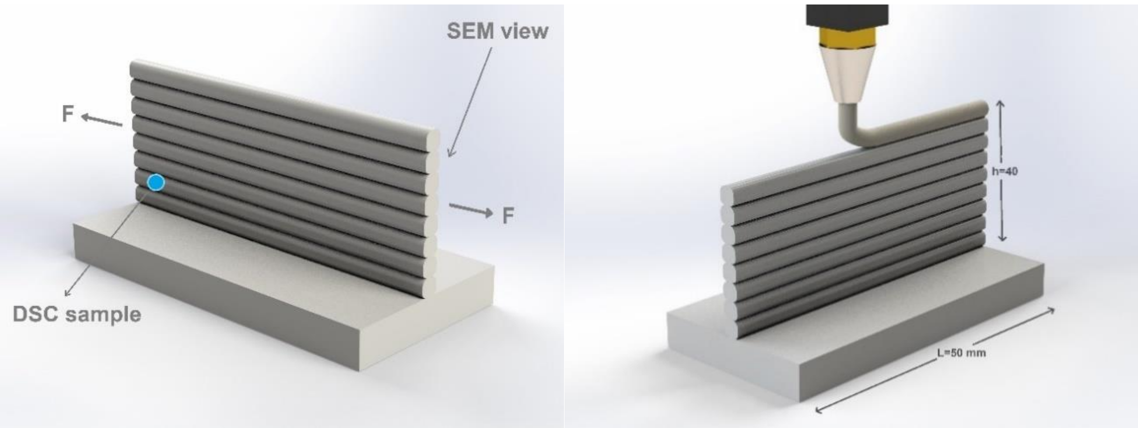

Fig. 2. Schématisation des échantillons imprimés

2.2. Classification des paramètres de processus

Il existe plusieurs paramètres de process pour chaque imprimante 3D. Ces paramètres jouent un rôle essentiel en termes d'adhérence entre les couches imprimées et de propriétés mécaniques des pièces fabriquées par le procédé de fabrication additive. Les principaux paramètres de process pour l'imprimante FlashForge Adventurer 3 sont présentés dans le tableau 1.

Condition No.	T_{Buse} (°C)	T_{Lit} (°C)	V (mm/s)	Hauteur de couche (mm)
No. 1	220 230 240	25±0.5	15	0.1
No. 2	240	25±0.5	13 15 17	0.1
No. 3	240	25±0.5	15	0.1 0.2 0.3
No. 4	240	25±0.5 45±1 62±1 79±1	15	0.1

Tableau 1. Paramètres du processus FFF. Cas de l'imprimante FlashForge Adventurer 3

In fine, cette étude a pour objectif de rapporter les effets de ces quatre paramètres pour les échantillons fabriqués par FFF :

- La température du liquéfacteur (T_{Liq})
- La température de la plate-forme/lit (T_{Lit})
- La vitesse d'impression (V)
- La hauteur de la couche

Les conditions d'impression des spécimens à des fins d'évaluation de la température du liquéfacteur, de la vitesse d'impression, de la hauteur de la couche et des effets de la température de la plate-forme du lit sont classées comme conditions No. 1, 2, 3 et 4 dans le tableau. 1, respectivement.

2.3. Matériels et méthodes

2.3.1 Observation microscopique

L'observation microscopique de la matière première utilisée (CF-PA6) a été réalisée à l'aide d'un microscope optique ZEISS (OLYMPUS BH2) avec des grossissements de x100 et x200. En ce qui concerne l'observation qualitative des spécimens imprimés pour les différents paramètres du processus sélectionné, le microscope électronique à balayage HITACHI 4800 SEM, encore désigné MEB, a été employé.

2.3.2 Calorimétrie différentielle à balayage (DSC)

La calorimétrie différentielle à balayage (DSC), avec l'appareil DSC Q1000, a permis de déterminer la température de transition vitreuse et de cristallisation, la capacité calorifique des matières premières utilisées et des échantillons imprimés toujours selon les paramètres de traitement sélectionnés. Ceci permet ainsi la caractérisation des filaments utilisés. La caractérisation DSC des matières premières a été réalisée en trois rampes dans la plage de température de -20°C à 220°C. L'histoire thermique de l'échantillon a été effacée dans la première rampe. Ainsi, les résultats obtenus sont mesurés dans des conditions contrôlées. Les valeurs de vitesse de chauffage et de refroidissement étaient de 10 °C/min. Tandis que la caractérisation DSC des spécimens imprimés a été réalisée en deux rampes (chauffage et refroidissement) avec des valeurs de vitesse de chauffage et de refroidissement de 10 °C/min et une plage de température s'étalant de 20 °C à 220 °C.

2.3.3 Mesure DMTA

La température de transition vitreuse principale de l'échantillon en CF-PA6 imprimé est obtenue par des essais de flexion avec analyse thermomécanique (DMTA). La mesure est réalisée avec l'équipement DMA Q800 de TA Company. Le test de flexion a été mené dans une plage de température allant de 30 à 80 ºC, une rampe de température de 2 ºC/min, une fréquence de 1 Hz et une force appliquée de 30 N.

2.3.4. Essai de traction quasi-statique

L'éprouvette de traction a été découpée à partir d'un bloc imprimé. La dimension de l'échantillon utilisé pour l'essai mécanique est conforme à la norme ISO 527-2 (Fig. 3). Des expériences de traction quasi-statique ont été réalisées avec la machine INSTRON 4301 avec une vitesse de déplacement de 5 mm/min. En fait, selon le spécimen imprimé (Fig. 2), les échantillons de test mécanique préparés provenaient des couches à paroi unique imprimées, qui avaient un angle de trame de 0 degré. Au moins trois éprouvettes ont été préparées pour effectuer ces essais de traction.

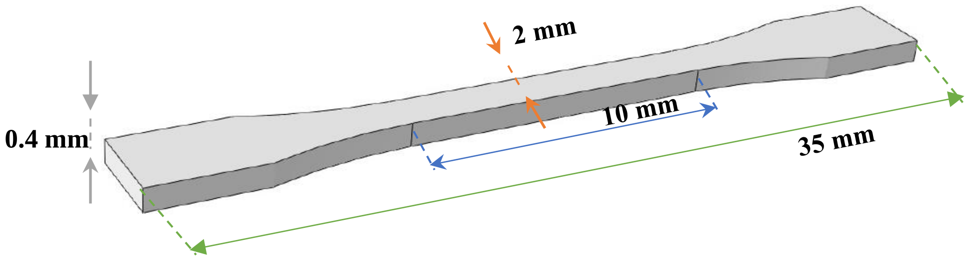

Fig. 3. La géométrie de l'éprouvette utilisée

2.4 Surveillance in situ de l'évolution de la température

Une caméra infrarouge Optris PI450 a été employée dans l'étude des effets des paramètres du procédé sur les propriétés thermiques et mécaniques des polymères et des composites utilisant le procédé FFF. Cette caméra a été utilisée en tenant compte de la distance préalablement déterminée et spécifique de l'extrudeuse pour obtenir un champ de vision simple (FOV) approprié à toutes les couches successives imprimées (Fig. 4). En ce qui concerne les données techniques de la caméra infrarouge, elles sont respectivement de 80 Hz, 382 x 288 pixels, 32 Hz, 8-14 µm et 2 %. De plus, l'auto-échauffement du composite pendant l'essai de fatigue se fait sur la surface de l'échantillon au moyen de cette caméra.

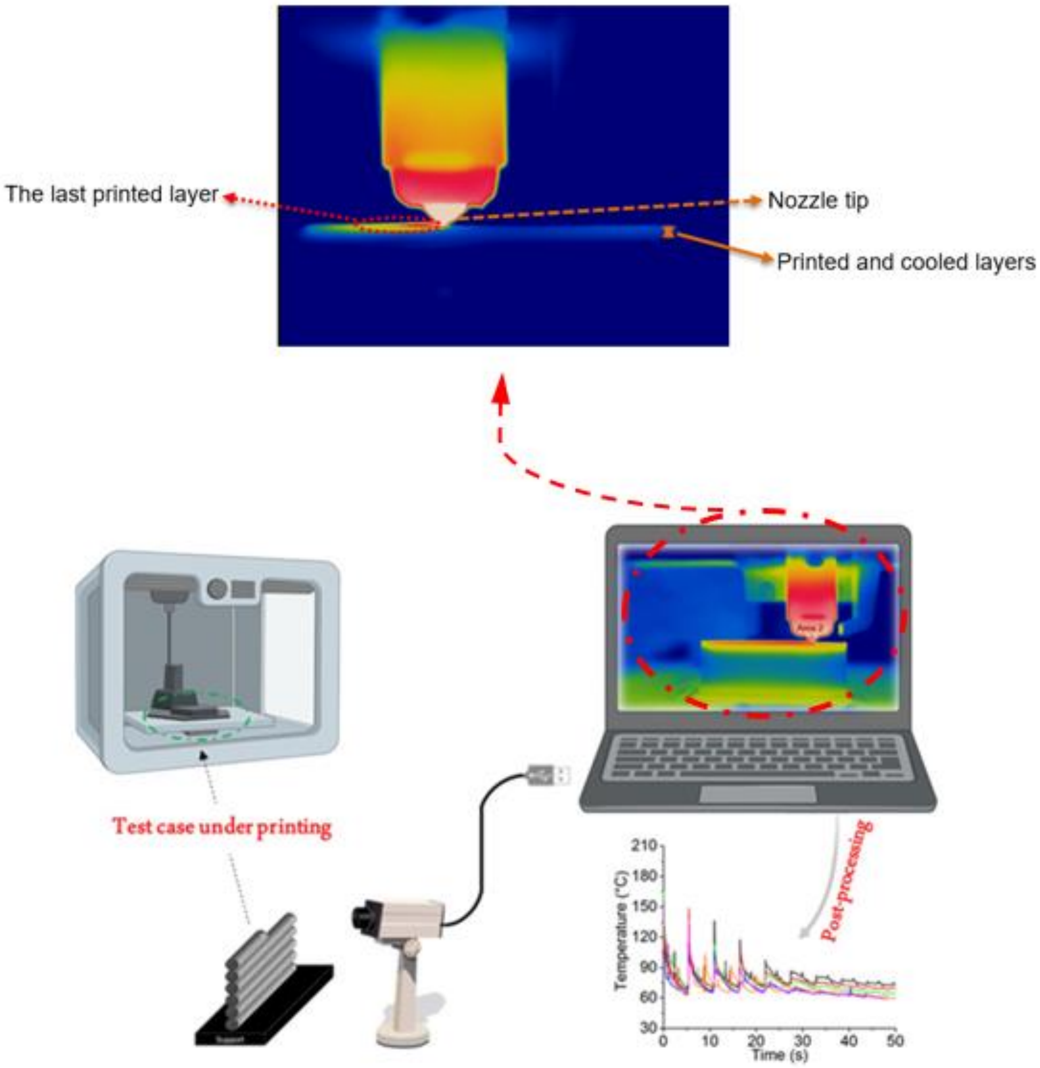

Fig. 4. Surveillance in situ de l'évolution de la température pendant le processus FFF

3. Résultats et discussions

3.1. Caractérisation du filament utilisé (matière première)

3.1.1. Analyse des microstructures

D’après l'observation des fibres de carbone sous microscope optique, la gamme de taille (en longueur) des fibres de carbone coupées va de 10 à 312 micromètres (Fig. 5 (a)). Il est à noter que le diamètre du filament CF-PA6 utilisé était de 1.75 mm. Selon l'observation optique du filament CF-PA6 (Fig. 5 (b)), les carbones hachés du filament CF-PA6 sont orientés selon la longueur du filament. L'orientation unidirectionnelle approximative de la fibre de carbone courte en longueur du filament CF-PA6 était due au processus de production du filament à savoir par extrusion.

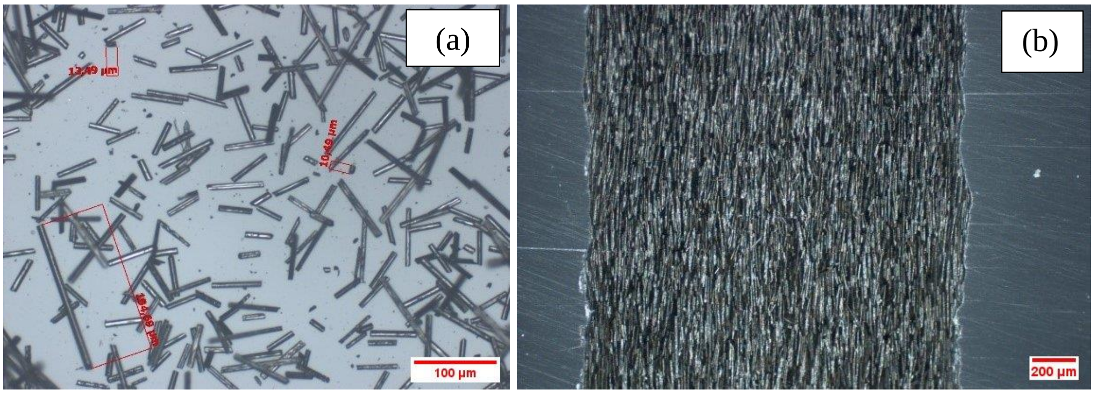

Fig. 5. Observation de la microstructure : (a) après pyrolyse à 500°C pendant 5h, et (b) orientation de la fibre en filament

3.1.2 Caractérisation du comportement thermomécanique par DMTA

Les courbes présentées ci-après (Fig. 6) ont été obtenues à l’aide de l’appareil DMA Q800. Les principales températures de transition dues à la mobilité moléculaire en fonction de la température sont ainsi mesurées. Comme on peut le constater, le CF-PA6 le CF-PA6 possède une transition vitreuse aux alentours de 47 ºC.

Cet essai est utile pour analyser le phénomène d'auto-échauffement induit et le mettre en relation avec l'échauffement mesuré lors d'un essai de fatigue à différentes amplitudes.

La réponse élastique ou visqueuse du CF-PA6 peut être mesurée en fonction de la température à l'aide de DMTA ; il est possible donc de comprendre le véritable amortissement interne du système. On peut supposer que le CF-PA6 a une stabilité rigide à température ambiante tandis que le module de stockage continue à diminuer lentement jusqu'à 80°C ceci en raison de l'augmentation de la mobilité de la chaîne macromoléculaire.

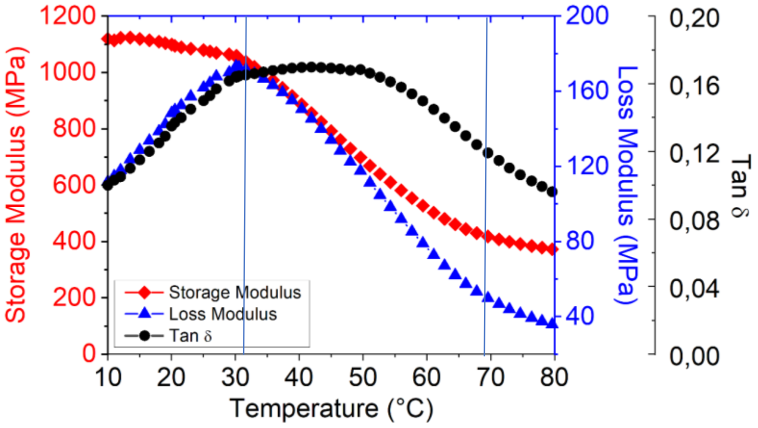

Fig. 6. Résultat du test DMTA : Évolution du stockage, des modules de perte et du facteur de perte en fonction de la température

Cependant, étant donné que le comportement thermomécanique du polymère détermine les diverses transitions et changements d'état physique du polymère, le test DMTA est mis en œuvre en utilisant la configuration de flexion alternée (avec la fréquence de 1 Hz). Le résultat obtenu est représenté sur la Fig. 6 comprenant trois états physiques : état vitreux, zone de transition vitreuse et état caoutchouteux. Comme on peut le voir sur cette figure, le matériau présente un état vitreux jusqu'à ~30 °C. A l'état vitreux, E' est relativement élevé (~1100 MPa). La deuxième zone (30 °C <T< 65 °C) correspond à la zone de transition vitreuse. E' diminue drastiquement de ~1100 MPa à une valeur inférieure à 400 MPa. L'état caoutchouteux du matériau se trouve dans la zone de température supérieure à 65 °C. La valeur de E' est alors faible et l'échantillon est relativement « mou ».

3.2. Caractérisation de l'échantillon imprimé

Un échantillon de référence avec des paramètres de processus spécifiques a été imprimé (température du liquéfacteur : 240°C, vitesse d'impression : 15 mm/s, hauteur de couche : 0,1 mm, température de la plateforme : 25°C). Par la suite, l'effet des paramètres du processus sélectionnés (tableau 1) a été pris en compte pour être comparé aux paramètres du processus de référence. A cet égard, des caractérisations physico-chimiques et mécaniques ont été menées, ainsi que le profil de température de la première couche déposée a été surveillé, in situ, lors du dépôt des couches déposées suivantes. Enfin, les résultats obtenus ont été utilisés pour évaluer l'impact de chacun des paramètres du processus sur les objets fabriqués.

La courbe de traction obtenue et les conditions d’essai de traction de l'échantillon de référence sont présentées à la Fig. 7 ainsi que le tableau fourni dans la section annexe. Trois échantillons ont été testés. La contrainte maxi et la déformation à la rupture mesurée sont respectivement d'environ 60 MPa et 30 %.

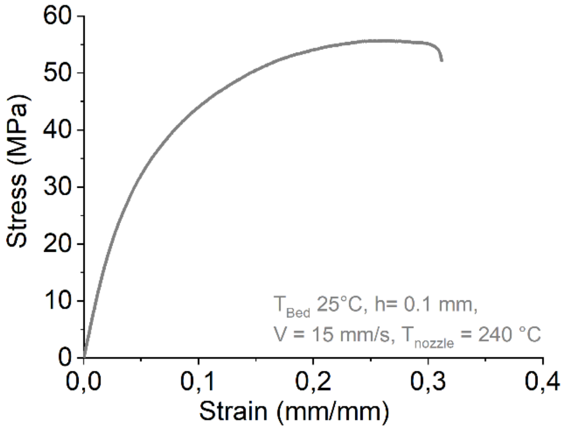

Fig. 7. Résultats de traction pour l'échantillon de référence

Certains tests ont été faits en utilisant des mesures locales pour enregistrer le profil de température des couches consécutives déposées à différents endroits. Le profil de température enregistré a été retenu pour la première couche déposée lors du dépôt d'autres couches dans une séquence de dépôt et ceci à un endroit déterminé à partir du début du dépôt (Fig. 8). L'objectif était de connaître le profil de température des couches consécutives déposées au cours du processus FFF au moyen d'une mesure ponctuelle in situ.

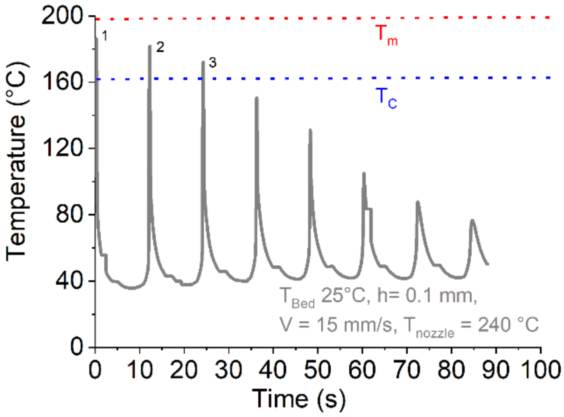

Fig. 8. Courbe obtenue liée au profil de température de la première couche imprimée lors du dépôt des autres couches dans l'échantillon de référence

3.3. Effet des paramètres du procédé FFF

3.3.1. Influence de la température du liquéfacteur

Selon l'étude menée, les paramètres du procédé FFF ont un impact sur les courbes Température-Temps qui sont représentatives du modèle de vitesse de refroidissement des couches imprimées. L'effet de la température du liquéfacteur comme étant l'un des paramètres de processus les plus importants a été pris en compte. Pour pouvoir étudier l'effet de la température du liquéfacteur, trois valeurs différentes de 220, 230 et 240 ºC ont été considérées pour comparer leurs résultats (tableau 3). D’après les courbes DSC obtenues pour les échantillons imprimés sous ces différentes températures, on peut constater qu’en modifiant la température du liquéfacteur, le degré de cristallisation et les valeurs de flux de chaleur associées à la cristallinité ne sont que légèrement modifiés (Fig. 9, Tableau 2). Plus précisément, la valeur de température de cristallisation associée dans le cas de 240 ºC a été augmentée.

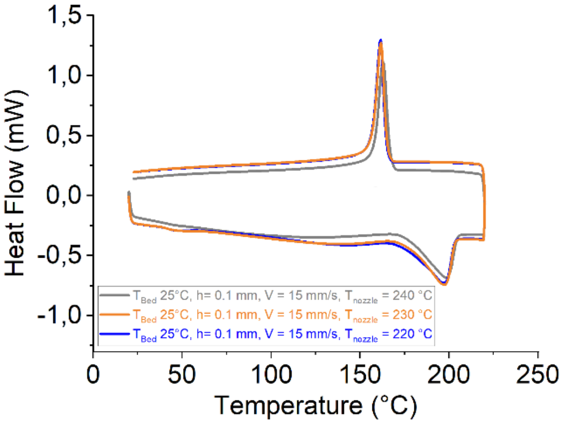

Fig. 9. Résultats DSC pour les échantillons fabriqués sous les différentes températures du liquéfacteur.

Conditions		T_c (°C)	T_m (°C)	%Crystallinity
No. 1	$T_{Liquefier}$ = 220 ºC	161.5°C	197.5°C	19.97%
	$T_{Liquefier}$ = 230 ºC	161.7°C	197.7°C	20.26%
	$T_{Liquefier}$ = 240 ºC	162.8°C	198.7°C	20.51%

Tableau 2. Valeurs obtenues liées aux différentes propriétés des courbes DSC des échantillons imprimés à différentes températures du liquéfacteur.

La Fig. 10 illustre les comportements à la traction des échantillons imprimés pour les températures du liquéfacteur déjà citées. La résistance à la traction maximale des spécimens imprimés à la température du liquéfacteur de 220, 230 et 240 ºC était respectivement de 49 ± 1.5 MPa, 51 ± 3 MPa et 55 ± 0.6 MPa. De plus, le pourcentage de cristallinité des échantillons fabriqués, pour cette même séquence de températures, était respectivement de 19,97 %, 20,26 % et 20,51 %. Ainsi, comme cela s'est révélé à partir des résultats obtenus, une augmentation de la température du liquéfacteur, entraîne une légère augmentation du pourcentage de cristallinité. Par ailleurs, cette (légère) tendance à la hausse a été observée pour la résistance à la traction obtenue par augmentation de la température du liquéfacteur parallèlement à l'augmentation de la cristallinité. De plus, l'évolution croissante du module de Young a été observée due à l'augmentation de la température du liquéfacteur lors de la fabrication FFF de CF-PA6. Aussi, selon Tian et al. [48], dans lequel l'effet de la température du liquéfacteur sur le processus de fabrication continu de composites PLA renforcés de fibres de carbone dans la plage de 180 à 240 ° C a été étudié, les valeurs obtenues de l'indice de fusion du PLA à la température de 180 °C et 240 °C étaient respectivement de 2 g/10 min et 36 g/10 min. En ce qui concerne les résultats obtenus, la résistance à la flexion et le module s'améliorent à mesure que la température augmente.

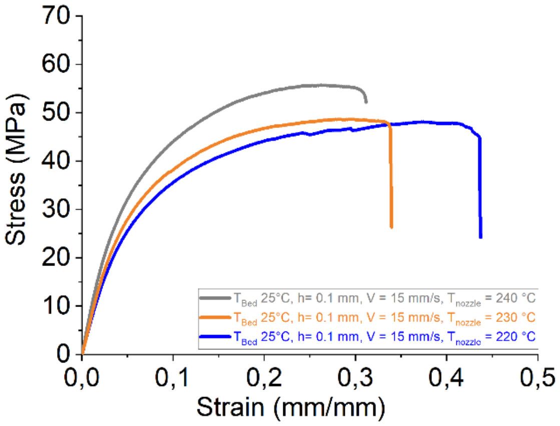

Fig. 10. Comportement en traction des éprouvettes imprimées pour les différentes températures du liquéfacteur

Des observations au microscope électronique à balayage (MEB) liées aux valeurs de température du liquéfacteur de T_{Liq} = 240 °C et T_{Liq} = 220 °C sont présentées à la Fig. 11.

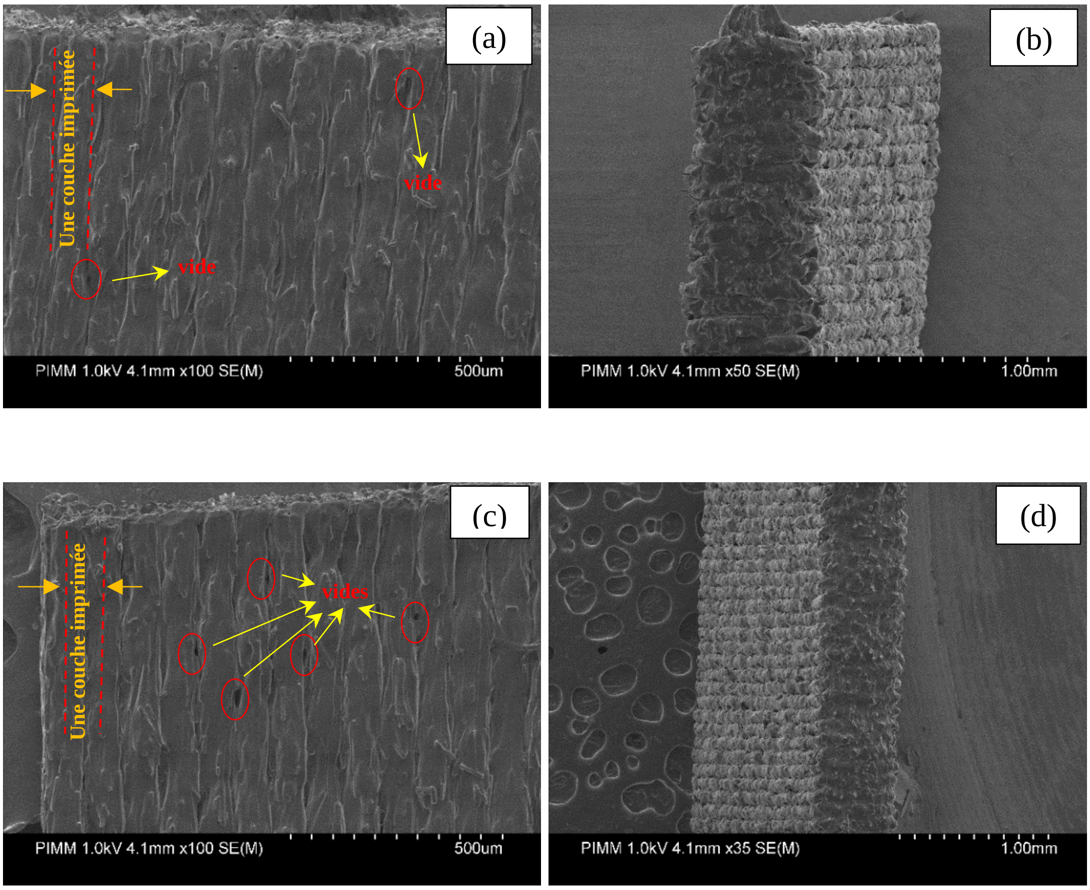

Fig. 11. Micrographies MEB à T_{Liq}= 240 °C (a, b) et T_{Liq} = 220 °C (c, d)

L'existence des micro-vides entre les couches imprimées, à l’origine des mauvaises propriétés mécaniques des spécimens fabriqués par FFF en comparaison avec ceux fabriquées par des procédés de fabrication conventionnels, est mise en évidence sur les photographies MEB. Les micro-vides à ces interfaces peuvent provenir d'une viscosité plus faible du PA6, ce qui cause une mauvaise adhérence et une faible résistance des couches entre elles, ce qui pourrait être par la suite des sites de propagation de fissures et de rupture. Dans les photographies MEB recueillies, les micro-vides sont plus sensibles pour le spécimen imprimé à la valeur de température du liquéfacteur de 220 ºC (et moins à la température de 240°C).

3.3.2. Influence de la vitesse d'impression

L'influence de la vitesse d'impression comme étant l'un des autres paramètres du processus a été envisagée. L'importance de celui-ci peut être soulignée en termes de vitesse de production. Pour étudier l'influence de la vitesse d'impression, trois vitesses 13, 15 et 17 mm/s ont été retenues pour la fabrication des échantillons. D’après les courbes DSC obtenues sur ces spécimens, il n'y a aucun changement notable dans les valeurs de degré de cristallinité (Fig. 12, Tableau 3).

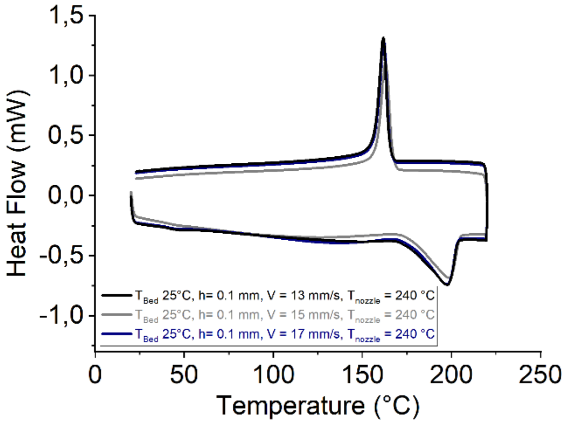

Fig. 12. Courbes DSC obtenues à partir d'échantillons imprimés à différentes vitesses d'impression

Conditions		T_c (ºC)	T_m (ºC)	%Crystallinity
No. 2	V = 13 mm/s	161.68°C	197.71°C	20.77%
	V = 15 mm/s	162.82°C	198.72°C	20.51%
	V = 17 mm/s	161.94°C	197.60°C	20.64%

Tableau 3. Résultats tirés des courbes DSC pour des échantillons imprimés à différentes vitesses.

Pour les tests de traction effectués sur les spécimens imprimés à ces différentes vitesses (13, 15 et 17 mm/s) les valeurs de résistance à la traction sont respectivement de 65 ± 0.5 MPa, 55 ± 0.6 MPa et 63 ± 1.3 MPa (Fig. 13). Les caractéristiques de traction des échantillons pour les vitesses d'impression de 13mm/s et 17 mm/s sont proches les unes des autres en comparaison de celles obtenues à 15 mm/s. On peut noter que le degré de cristallinité de l'échantillon imprimé à la vitesse de 13 mm/s était légèrement plus élevé, ce qui a également montré une résistance à la traction plus élevée. Cependant, les micrographies SEM des spécimens fabriqués à la valeur de vitesse d'impression de 13 mm/s montrent des micro vides à l'interface des couches (Fig. 14) et l'échantillon ne présente pas une bonne précision dimensionnelle. En raison de la faible stabilité dimensionnelle, il semble que l'échantillon imprimé avec une vitesse d'impression de 15 mm/s présente des conditions de traitement optimisées.

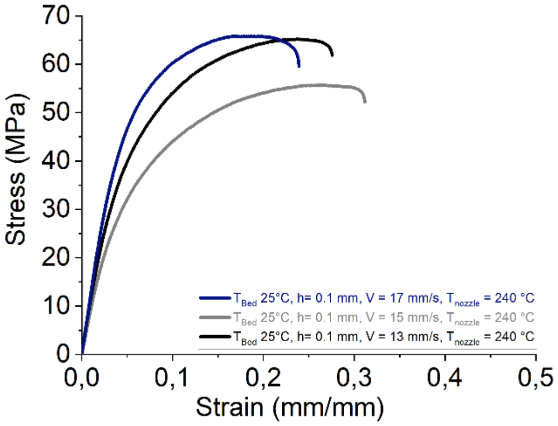

Fig. 13. Comportement en traction des éprouvettes imprimées aux différentes valeurs de vitesse d'impression

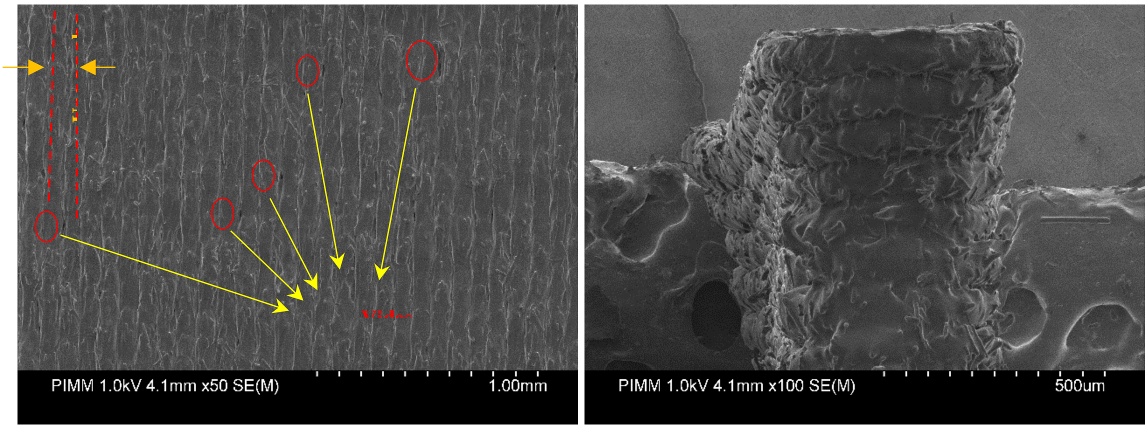

Fig. 14. Micrographies MEB liées aux spécimens imprimés à V = 13 mm/s

Pour analyser ce phénomène, des mesures de température in situ ont été faites pour les différentes vitesses d'impression (13, 15 et 17 mm/s). Les résultats sont présentés en Fig. 15. Ces derniers montrent que pour une augmentation de la vitesse d'impression, l'évolution de la température de la première couche imprimée reste au-dessus de la température de cristallisation dans les échantillons imprimés avec les trois valeurs de vitesse d'impression considérées. On peut noter que l'amélioration de la vitesse d'impression modifie le réarrangement des chaînes polymères et le degré de cristallinité obtenu en conséquence en diminuant le temps de refroidissement. Ce dernier peut être la raison de la mauvaise stabilité dimensionnelle.

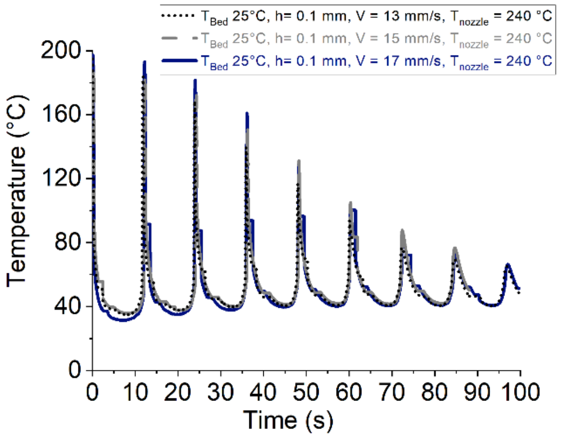

Fig. 15. Mesure de température in situ pour différentes vitesses d'impression

3.3.3. Influence de la hauteur de couche

L'effet de la hauteur de la couche en tant qu'un des paramètres du processus a été étudié dans le procédé de fabrication par filaments fondus du CF-PA6. Cette hauteur a été définie pour trois valeurs : 0.1 mm, 0.2 mm et 0.3 mm afin d'observer et d'analyser l'impact de celle-ci sur le comportement mécanique des échantillons réalisés. D'après les résultats des tests de traction obtenus, les échantillons imprimés pour les valeurs de hauteur de couche précédemment choisies et dans cet ordre croissant, montrent respectivement une résistance à la traction de 55 ± 0.6 MPa, 49 ± 2.5 MPa et 56 ± 2.5 MPa (Fig. 16). De plus, les valeurs en pourcentage de cristallinité de 20.51, 19.27 et 21.22 ont été enregistrées toujours en respectant ce même ordre croissant de hauteur de couche (tableau 4).

A partir des résultats obtenus, il est suggéré l'existence de deux facteurs compétitifs en termes de comportement mécanique pour des échantillons fabriqués par ce procédé FFF du CF-PA6. Les deux facteurs qui se concurrencent par l'augmentation de la hauteur de couche sont (i) la diminution de la liquidité (ou fluidité) des couches imprimées, et (ii) l'augmentation de la température retenue dans les couches imprimées. L'effet de la diminution de la liquidité (ou fluidité) s'est révélé dominant pour les échantillons obtenus en modifiant la hauteur de couche de 0.1 mm à 0.2 mm. Ce qui a provoqué la diminution de l'adhérence et de la liaison de la couche imprimée et, par voie de conséquence, la résistance à la traction des échantillons imprimés avec une hauteur de couche de 0.2 mm par rapport aux échantillons imprimés avec une hauteur de couche de 0.1 mm. L'augmentation indiquée de la fluidité a été conclue à partir des pics observés obtenus à partir des courbes d'évolution de la température (Temps-Température), dans lesquelles la valeur de température maximale enregistrée de chaque couche imprimée avec une hauteur de couche de 0.1 mm était supérieure à celle du dépôt de couche d'une hauteur de 0.2 mm (Fig. 17).

De plus, le pourcentage de la cristallinité a été légèrement diminué par l'augmentation de la hauteur de la couche de 0.1 mm à 0.2 mm. Alors qu'il est proposé que l'effet de l'augmentation de la température retenue dans les couches imprimées a surmonté le premier facteur concurrentiel, dans le cas du procédé FFF de CF-PA6 avec une hauteur de couche de 0.3 mm. Depuis la courbe Temps-Température (le bas des courbes) liée à la hauteur de la couche imprimée de 0.3 mm (Fig. 17), on peut observer que plus la valeur de température, ce qui peut provoquer le réarrangement des chaînes polymères et l'augmentation conséquente du comportement mécanique, dû à l'augmentation du pourcentage de cristallinité.

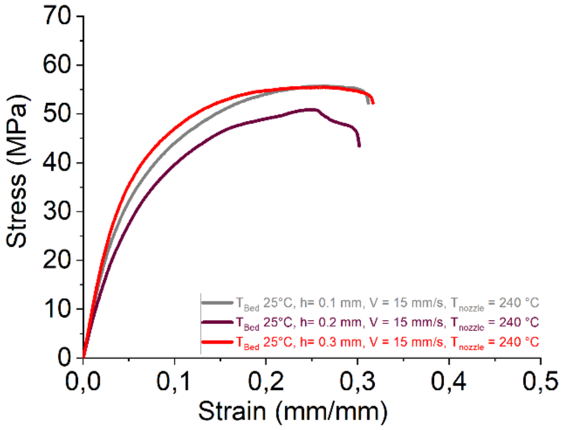

Fig. 16. Comportement en traction des éprouvettes imprimées pour différentes hauteurs de couche

Conditions		T_c (°C)	T_m (°C)	%Crystallinity
No. 3	h = 0.1 mm	162.82°C	198.72°C	20.51%
	h = 0.2 mm	161.50°C	197.79°C	19.27%
	h = 0.3 mm	161.68°C	197.48°C	21.22%

Tableau 4. Caractéristiques obtenues à partir des courbes DSC pour différentes hauteurs de couche

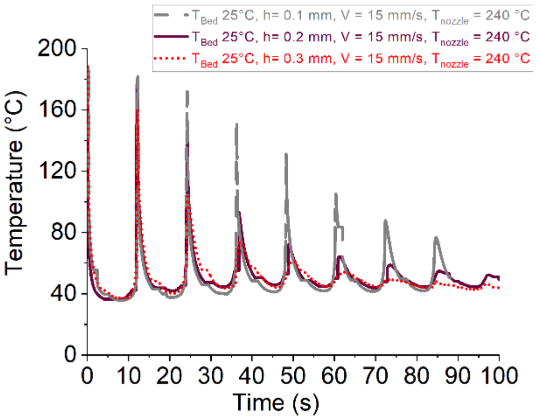

Fig. 17. Mesure de température in situ des échantillons imprimés selon différentes hauteurs de couche

3.3.4. Influence de la température du lit

L'effet de la température du lit a été analysé pour différentes valeurs de température :25, 45, 60 et 80 °C. On peut noter que généralement, le PA6 a une viscosité relativement faible et qu'en augmentant la température du lit, le risque de manque de stabilité dimensionnelle peut se produire. La Fig. 18 fournit les micrographies MEB relatives à l'échantillon imprimé CF-PA6 à la température du lit de 80 °C. On peut observer que les couches sont plus déformées par rapport aux micrographies MEB de l'échantillon imprimé à une température de lit de 25 °C (Fig. 11). De plus, davantage de vides sont observables.

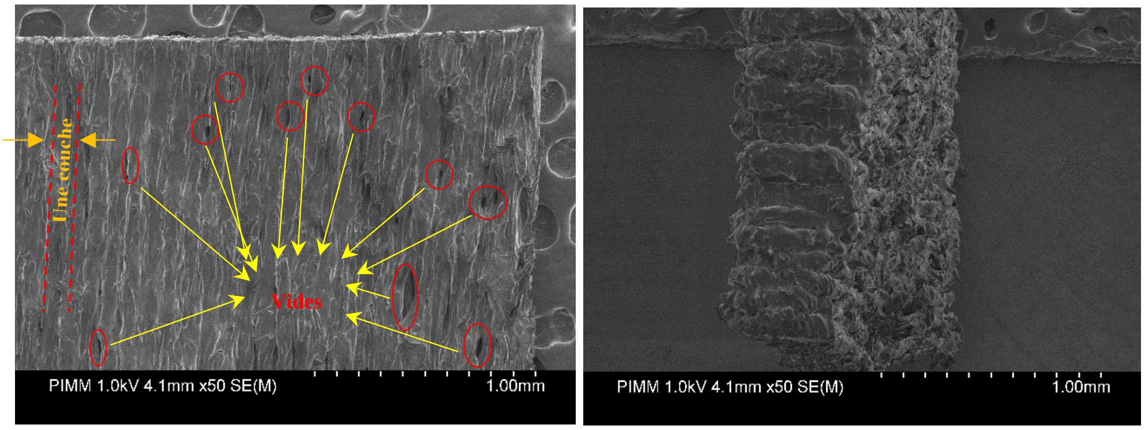

Fig. 18. Micrographies MEB relatives d'un échantillon pour une température de lit de 80 °C

La Fig. 19 présente la mesure de température in situ d'échantillons imprimés en CF-PA6 pour les différentes températures de lit. Pour tous les spécimens imprimés avec les différentes températures de lit susmentionnées, après le dépôt de la première couche, la température reste inférieure à la température de cristallisation. Cependant, à la température du lit à 80°C, cette valeur étant plus proche de la température de cristallisation, le problème de stabilité dimensionnelle subsiste.

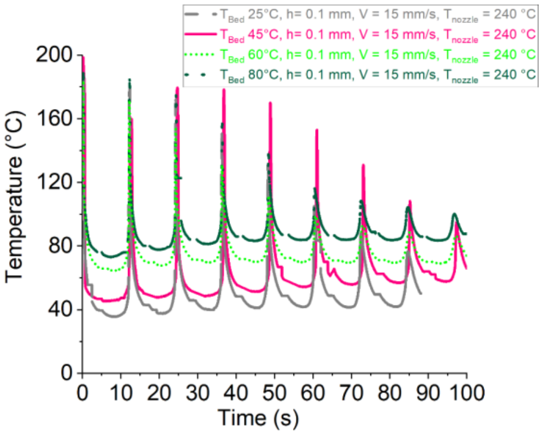

Fig. 19. Mesure de température in situ des éprouvettes imprimées pour les différentes températures de lit

3.4. Analyse de la microstructure liée aux spécimens imprimés

La Fig. 20 fournit les observations de microstructure des échantillons (10 filaments déposés) selon les conditions de référence. Le but de cette analyse est de suivre l’évolution de la surface de contact de deux couches adjacentes. Les résultats révèlent qu'en augmentant la distance à partir de la première couche déposée, la surface de contact des couches adjacentes suivantes a diminué. Du fait de l'évolution de température annoncée des couches déposées, on constate qu'après 2 ou 3 séquences de dépôt (couche), la température descend en dessous de la température de cristallisation. Ceci affecte la vitesse de refroidissement, la solidification du matériau et contribue à un moindre « étalement » du matériau et ainsi à la diminution de la surface de contact entre deux couches successives déposées.

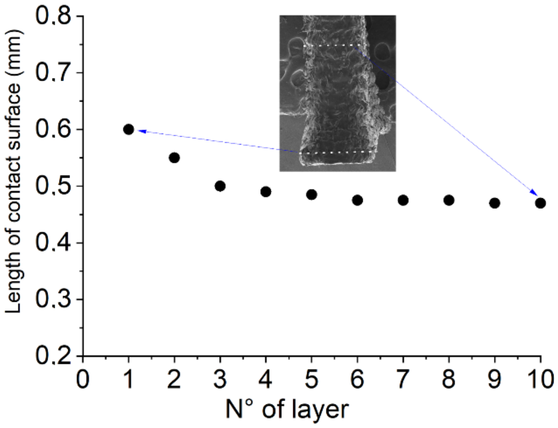

Fig. 20. Analyse de la longueur de contact entre deux filaments adjacents (Echantillon de référence)

Tout en prenant en compte l'échantillon de référence, chacune des conditions a montré son effet sur la caractéristique finale et la microstructure des pièces fabriquées. Selon les observations précitées, la même démarche a été adoptée pour les différentes couches (Fig. 21) ceci afin d’évaluer la surface de contact de chacun des filaments adjacents. Cette analyse est bénéfique pour synthétiser l'impact de chaque paramètre du procédé sur le collage et la qualité des pièces fabriquées. On peut noter que l'échantillon de référence a une surface de contact plus stable au niveau des 10 premières couches imprimées. Cette analyse confirme que l'échantillon de référence (température du liquéfacteur : 240 °C, vitesse d'impression : 15 mm/s, hauteur de couche : 0,1 mm et température de la plate-forme : 25 °C) fournit les paramètres optimaux du processus FFF.

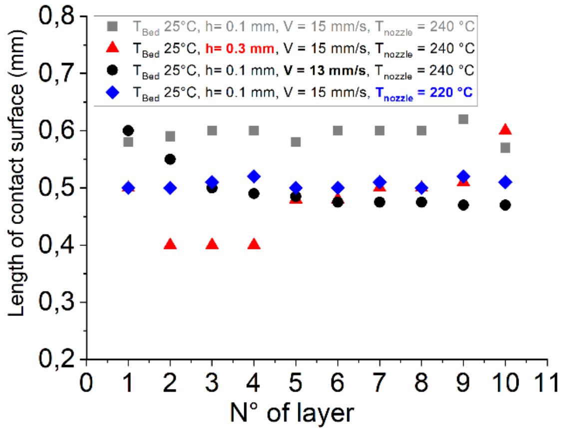

Fig. 21. Comparaison de la longueur de contact entre deux couches adjacentes pour chaque condition d'impression

4. Conclusions et perspectives

Ce travail présente une étude expérimentale visant à quantifier l'impact des principaux paramètres associés au processus FFF sur l'adhérence inter-couche (liaison) des filaments déposés pour des composites à base de polymères. Des analyses thermique, physico-chimique et mécanique ont montré que le degré de cristallinité peut affecter la « diffusion » du matériau pendant la phase de refroidissement qui contrôle la liaison de deux filaments adjacents et par conséquent les propriétés mécaniques de la pièce finale. L'évaluation du profil de température des couches imprimées montre que les paramètres du procédé FFF ont un effet significatif sur le processus de refroidissement des filaments. Les contraintes/déformations de rupture peuvent être des indicateurs permettant de déterminer les propriétés mécaniques des produits manufacturés FFF. On peut noter que le polymère utilisé dans cette étude était le PA6 et qu’il présente un faible poids moléculaire et une faible viscosité. Pour analyser l'effet des paramètres de procédé dans ce type de matériau, il est important de porter une attention particulière à la température. En augmentant la température du lit, des problèmes de stabilité dimensionnelle et de présence de vides peuvent survenir. Les résultats de ce travail confirment que l'échantillon de référence (avec des conditions d'impression de température du liquéfacteur : 240 °C, vitesse d'impression : 15 mm/s, hauteur de couche : 0.1 mm, température de la plate-forme : 25 °C) présente les meilleurs paramètres pour un processus optimal.

Abstract:

Additive manufacturing (AM) is a novel technology that enables rapid fabrication of physical models directly from 3D computer-aided design (CAD) data without any conventional tooling or programming requirement. Thermoplastic polymers are the most useful materials for the manufacturing of parts in the FFF process. In this process, extrusion of a semi-molten road through a nozzle is taken place to form each layer, the extruded road solidifies quickly due to the existence of temperature gradient between the surroundings and the extrusion temperature. Different key parameters affect the final products manufactured by this process. These parameters can be listed in three categories. Some of them are linked to the material, others are linked either to the characteristics of the process or to the specificity of the machine. They can influence the properties of the final part through their effect on various physical phenomena. The mentioned parameters affect the polymer temperature and its evolution. It is important to know the evolution of filaments temperature with time and recognize how it is affected by major process variables as mentioned. Due to the nature of the FFF process, it is important to measure the temperature profile and its evolution during the process by the means of local measurement methods. The idea of this work took place in 2018, by start reviewing literatures related to the FFF process. As mentioned, almost all studies and works either numerical or experimental approaches were based on global consideration. In the beginning, the work was concentrated on finding a method to be applied to the FFF process to proceed with the localized investigation. Afterward, the experiment was started to see the possibility of the work. As in the FFF process, there is a deposition of filaments, and each filament itself is heated by the deposition of newer filaments, there is almost a cyclic evolution of the temperature due to multi-layer deposition and it means that each filament is re-heated consequently because of the deposition of a new filament. This is a critical issue in creating a filament bonding and diffusion of materials. To implement and measure this cyclic temperature, it is required to apply a measurement device in which to be capable of measuring the temperature of the polymer when leaving the nozzle. One can note that the mechanical properties of 3d-printed pieces are limited. In this work, we try to improve the mechanical properties by reinforcing the fibers such as glass fibers, carbon fibers, etc. At the same time by controlling the temperature evolution, we try to improve the adhesion between the layers to have the best structure. The used material as raw material was polyamide-6 (PA6). The main objective of this research is to study the rheological characteristics of materials during FDM/FFF to process optimization for mechanical characterization improvement of the fabricated parts. Therefore, the main objective is to take into account both the temperature and viscosity parameters, and to establish the Time-Temperature-Transformation diagram for process optimization. This helps to determine the processability area.

Keywords: 3D printing, Rheology, Temperature evolution, Inter-layer bonding, Mechanical strength

Arts et Métiers Sciences et Technologies

HESAM UNIVERSITÉ